DOCTOR OF PHILOSOPHY

Generation of Very Long Waves in Laboratory for Tsunamis Research

Lu, Heng

Award date:
2017

Generation of Very Long Waves in Laboratory for Tsunamis Research

Heng Lu

Doctor of Philosophy
University of Dundee
July, 2017

Declaration

I declare that this thesis was composed by myself and that the work contained therein is my own, except where explicitly stated otherwise in the text.

(*Heng Lu*)

This thesis is dedicated to my parents.

Acknowledgements

I would like to express my sincere gratitude to my supervisor, Dr. Yong Sung Park, for his patience, great guidance and continuous support in all aspects of the research and my PhD life.

I would also like to thank the financial support from the University of Dundee and the partial support of the Korea Institute of Ocean Science and Technology (KIOST). In this regard, again, thank Dr. Yong Sung Park for arranging the major part of the funding during my PhD study.

I acknowledge my examiners: Dr. Masoud Hayatdavoodi and Dr. Nils Goseberg, and the convenor: Dr. Anthony Leung, for their valuable comments contributed to my work and the thesis. Also, I appreciate the generosity and hospitality of Professor Young Do Kim for inviting and funding me the visit to the Inje University in Korea. I enjoyed the work and discussion with him, Professor Jae-Hyeon Park, Dong-Seok Chae and all the students in the group. I thank all of the people who provided me valuable suggestions for my work.

Many thanks to: Mr. Alex Anderson, for constructing and maintaining the equipment; Mr. Michael McKernie, for assisting in setting up the electronic components; Mr. David Husband, for the IT support.

Besides, I thank my fellow students: Li Ma, Shengwenjun Qi and Rui Zhao, for the discussions and fun we have had, in particular the exercising time in ISE. Thanks also go to my best friends: Danying Chen, Qiqi Shu and Yunling Wang, for your listening and encouragement since we met in our teens. Friendship lasts forever.

Finally, I would like to thank my parents, my cousins and my partner Xiaocheng Shang, for your love, support and constant care. I love you all.

Abstract

This thesis is motivated by recent field observations of tsunamis which point out that use of solitary waves as model tsunami is not theoretically justified. In order to generate very long waves in laboratory, a bottom-tilting wave maker is designed and used at the University of Dundee. This new type of wave maker can produce waves longer than the effective length of solitary waves, which provides better long wave model. The main idea of the bottom-tilting wave maker is that moving the entire bottom can lead to the wave as long as the given wave tank. Meanwhile, some analytical solutions and numerical models are developed in this research for theoretical investigation. Wave behaviour in the tank without beach and the wave run-up on a plane beach are of main interest. The unique contributions for the two scenarios are that wave profile or run-up height of very long waves with a variety of bottom motions and surface problems have been investigated, respectively.

A series of experiments are conducted in the new wave tank by inputting the prescribed bottom motions to the electrical motor with varying water depth, bottom motion displacement and speed. The free surface elevation time-histories are measured by acoustic wave gauges while the maximum run-up heights of varying waves are observed by a video camera.

Nonlinear and dispersive numerical models are developed in this thesis for modelling the wave tank. A shock-capturing finite volume scheme with high-order reconstruction method is used to solve the governing equations, coupling with a computational domain mapping technique to estimate the moving shoreline. By comparing to the experimental measurements, the numerical models are verified and able to approximate the resulting waves in the wave tank. Surface waves

studied in Boussinesq scaling with time-dependent bottom bathymetry gives a better performance in approximating the wave generation in the tank without a beach, while nonlinear shallow water system is good at approximating the wave run-up on a plane beach. The computational domain is as long as the wave tank and bounded by two fully-reflective vertical walls at the two ends. The analytical solutions of the time-history of free surface elevation are derived by the linear wave theory in an infinite domain. To further extend the study, the numerical model based on the Boussinesq equations in a semi-infinite wave tank is developed, in order to estimate the wave period which can not be easily determined from the experiments and to explore the wave profile in a tank with long propagation distance.

For wave generation in the tank without a beach, it can be verified that the new wave maker can provide new long wave model better than solitary waves by the theoretical results from the linear wave theory and the numerical model based on the Boussinesq equations. All the waves within the measured range are longer than the effective wavelength of the solitary waves with same wave amplitude, which can reach seven times longer at most. Using both the theoretical and experimental results, the relations between the bottom motions and the resulting waves have been investigated in terms of the wave amplitude, wave peak time and wave period. Note that only for estimating the wave period is assumed that the wave tank has semi-infinite domain by using the Boussinesq equations. In particular, wave amplitudes can be expressed by power function. For wave run-up on a plane beach, the parametric studies based on the nonlinear shallow water equations reveal how the run-up height relates to the bottom motion and the leading wave profile in a wave tank with adjustable beach slope. Monotonous dependence of the maximum run-up height on the wave height or wave-front steepness is discovered. Furthermore, the influence of the bottom friction and wave breaking are addressed.

Contents

List of Figures

List of Tables

List of Symbols

a motion amplitude at right end. 25

A wave amplitude. 20

A_s solitary wave amplitude. 7

b motion duration time. 75

B temporal component of motion displacement time series. 25

c phase velocity of waves. 71

c_s phase velocity of solitary wave. 7

$\mathrm{c_{sd}}$ speed of sound. 60

C a cell by finite volume discretisation. 28

C_d drag coefficient. 37

C_r Courant number. 34

D_0 motion amplitude along the moving bottom. 25

DF Jacobian matrix. 29

E Energy. 41

F Fourier transform operator. 27

$\mathbb{F}$ advective flux term. 28

F_r Froude number. 71

g gravitational acceleration. 14

h static water depth. 7

h_0 constant water depth. 20

i imaginary number unit. 24

I identity matrix. 32

k wavenumber. 20

K_s wavenumber of solitary wave. 7

L length of the moving bottom. 10

L_p stroke length. 9

L_s wavelength of solitary wave. 7

L_w wavelength of the generated wave. 22

m a fitting parameter. 87

$\mathbb{M}$ dispersive term. 28

n Manning's roughness coefficient. 40

n a fitting parameter. 87

Q relative velocity of bottom motion. 25

r rotating radius. 23

R run-up height. 37

R_e Reynolds number. 72

R_m maximum run-up height. 12

$\mathbb{S}$ source term. 28

t time coordinate. 7

$\mathrm{t_g}$ time from when sound leaves from sensor to its return back. 60

T wave period. 76

T_s wave period of solitary wave. 7

u horizontal velocity. 14

U shoreline velocity. 38

U_r Ursell parameter. 20

v_n velocity of the moving bottom normal to the bottom surface. 23

V variables. 28

V_s total mass. 41

V_w volume of the displaced water. 87

w vertical velocity of water particle on moving bottom. 23

W vertical velocity of the moving bottom. 23

W_e Weber number. 72

x horizontal coordinate. 7

x_0 location of the initial wave crest. 40

X shoreline position function. 38

Y_w trajectory of the moving bottom. 78

z vertical coordinate. 20

α ratio of the constant water depth to the length of the moving bottom. 48

β beach angle. 12

γ slope of beach. 35

Γ initial length of the computational domain. 35

δ Delta function. 26

Δ step of discretisation. 25

ϵ a small and positive number. 31

ε nonlinearity. 7

ζ displacement of the moving bottom. 20

η free surface elevation. 7

θ angle of rotation of the moving bottom. 23

θ_m maximum rotating angle of the moving bottom. 78

ι surface tension. 72

κ wave front steepness. 122

λ eigenvalue. 33

μ dispersion. 7

ν kinematic viscosity of water. 72

ρ water density. 72

ϱ one of the Riemann invariants. 36

Υ k integral part of the analytical solution. 27

Φ velocity potential. 21

φ one of the Riemann invariants. 36

χ spectral radius. 29

Ψ_g the distance from the sensor to the target. 60

ω angular frequency. 22

∇ gradient operator. 21

$*$ transformation by the computational domain mapping technique. 38

$\prime$ nondimensionalisation. 76

Chapter 1

Introduction

1.1 Background

The generation of tsunamis is typically owing to undersea earthquakes, landslides, volcanic activity, or other impulsive geophysical events. In particular, undersea earthquakes result in great displacement of large amount of water which will generate extremely long waves [$\sim O(1$ hour$)$] compared to ocean depths, whereas the amplitudes of tsunamis are very small (Mei, 1989). Meanwhile, tsunamis contain enormous energy even when they approach the beach, making them catastrophic (Yeh et al., 1994).

The waves propagate and evolve gradually over long distances, undergoing substantial changes. Thus, tsunamis are found different and varying in wave profiles during their propagation, even waves disintegrate or break, especially in near-shore region due to the fast decreasing water depth (Borthwick et al., 2006; Schimmels et al., 2016). Tsunamis consist of not only crest but also troughs, and lead with either of them. Leading-elevation tsunamis will propagate into a series of solitary waves after long period of time, but usually limited by not sufficiently long distance in realistic ocean (Madsen et al., 2008). Leading-depression waves are unstable and usually evolve into positive waves, but they still have been found in near-shore region from many field observations by that the shoreline recedes

before going up when the propagation distance is not long enough (Tadepalli and Synolakis, 1994).

With regard to the complicated fluid motion and the length of tsunamis, investigating very long waves in laboratory becomes significantly important for tsunami science. Solitary or solitary-like waves have been used to simulate tsunamis for a few decades, but they were questioned by recent research (Madsen et al., 2008) for not being justified theoretically, which will be reviewed in detail in Section 2.1. In Fig. 1.1, the records of the 2011 Japan Tohoku tsunami clearly show that the solitary wave is not long enough and too steep when compared to the observed leading tsunami. Determination of the wavelength restricted by the wave amplitude of solitary waves will underestimate the realistic relations of tsunamis in geophysical scales and mislead some crucial understanding of their further wave behaviours, for example, misinterpretation of the physical quantities (e.g., pressure and velocity) and too early breaking observed (Madsen et al., 2008; Goseberg et al., 2013).

As tsunamis approach shore and run up a beach, the wave amplitudes increase dramatically and rapidly, which often result in significant loss of lives and properties near the shore. Run-up height is determined as the vertical height on shore above the sea level. For instance, in 1896, an earthquake-induced tsunami with up to 38 m of run-up height struck Sanriku in Japan and caused about 22,000 casualties (Fujii et al., 2011). Coastal regions were severely damaged and 226,000 people died by the 2004 Sumatra Tsunami with typical run-up height of 5-6.5 m and maximum run-up height of 19.6 m at Ban Thung Dap (Rabinovich and Thomson, 2007). The recent 2011 Tohuku tsunami has the maximum run-up height up to 40 m at Ofunato, which resulted in about 16,000 death (Mori and Takahashi, 2012). Since the tsunami related damage is usually caused by its severe run-up and great velocity at shore, there is a continuing demand on better understanding run-up process and predicting maximum run-up height, in particular for tsunami hazard mitigation and coastal protection works.

Therefore, it is of great importance to build an appropriate physical wave

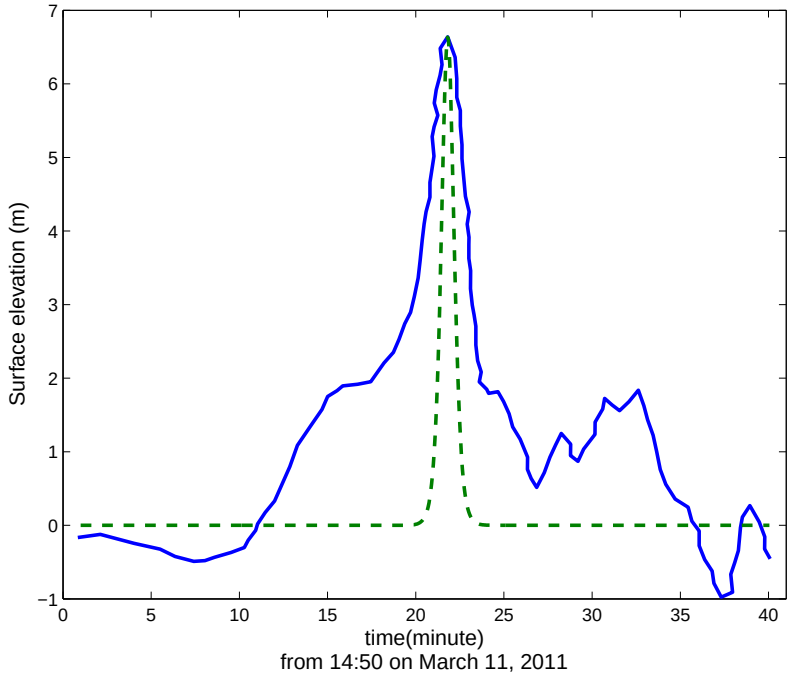

Figure 1.1: Comparison between the field data (solid line) at Iwate South during Japan Tohoku tsunami in 2011 (adapted from Fujii et al. (2011)) and the fitted solitary wave (dashed line) by Eq. (2.1).

model in tsunami research for more accurate theoretical and experimental investigations.

1.2 Objective and Scope

The objectives of this thesis are listed as follows:

- It aims to provide a more practical long wave model by a novel wave maker. The new wave maker called a bottom-tilting wave maker, is proposed in this study to generate waves as long as the given wave tank. To demonstrate that the new long-wave-model is more practical, longer waves will be generated which are longer than the effective length of solitary waves by only one single and simple bottom motion.

- Of equal importance is to investigate, both experimentally and theoretically,

the wave profile of the long waves and their run-up process on a plane sloping beach. A variety of bottom motions with a wide range of generation parameters are tested, including vertical motions upwards and downwards. Beach is only considered in the run-up investigation while a couple of slopes are observed.

- To quickly estimate the long waves before experiments and more precise computation, analytical solutions by the linear wave theory are proposed in this thesis.

- In order to facilitate the experimental investigation and further uncover some aspects of the long waves that cannot be found directly in the wave tank, two numerical models are developed in this thesis. For long wave generation and propagation, the numerical model based on the Boussinesq equations is applied, in terms of a domain same as the wave tank or a semi-infinite domain with long propagation distance. Otherwise, a numerical model based on the nonlinear shallow water equations is used to explore the process of long wave run-up in the wave tank. The numerical solver is derived based on a high-order shock-capturing finite volume scheme, for both numerical models.

- Other main objectives of investigating the relationship between the wave maker and the generated waves include: (1) relating the main characteristics (i.e., wave amplitude, wave period and the maximum run-up height) of the long waves to the bottom motions; and (2) associating the wave profile (i.e., wave amplitude and wave front steepness) with the maximum run-up height.

- The maximum run-up height is an important parameter to evaluate wave run-up. However, owing to the energy dissipation caused by bottom friction and breaking, the maximum run-up height will be reduced. Note that as breaking is too complicated, it is simplified numerically as bore and dealt with automatically in this study. These aspects of influence are addressed.

1.3 Outline

In this chapter, the background and motivation of the present study are introduced regarding some characteristics of tsunamis and the typical wave behaviour. The objective and scope of this study are demonstrated as well. The rest of the thesis is organized as follows.

In Chapter 2, a wide range of literature regarding long wave model as well as long wave run-up investigation in theoretical or experimental perspective are reviewed. Chapter 3 introduces the linear wave theory and the numerical models concerning dispersion and nonlinearity. The numerical solvers for the models of wave generation and wave run-up are described in detail, respectively, including the theoretical treatments of the shoreline motion and wave breaking. Then the experimental equipment and procedures are introduced in Chapter 4. Based on the theoretical and experimental results, the resulting long waves and their run-up processes are evaluated by comparing them and relating them to the bottom motion parameters in Chapter 5. Finally, concluding remarks are given in the last Chapter 6, with future works suggested.

Chapter 2

Literature Review

Long wave behaviour in shallow water and their impact on shore are reviewed in detail in this chapter. As the present study focuses on long wave generation and run-up, the related theoretical and experimental studies are emphasised.

2.1 Long wave model for tsunamis

Since the early 1970s, solitary or solitary-like waves have been the most commonly used tsunami wave models in theoretical and experimental studies of tsunamis (e.g., Hammack, 1973; Goring, 1978; Synolakis, 1987; Zelt, 1991; Grilli et al., 1997; Lin et al., 1999; Li and Raichlen, 2003; Synolakis and Bernard, 2006; Lo et al., 2013). It has been usually believed that solitary wave can capture many main features of tsunami behaviours in coastal region. Then, considering the bathymetry of the near-shore region or simply the slope of the beach into the long wave model, tsunami run-up can be modelled theoretically and experimentally (e.g., Tadepalli and Synolakis, 1994; Li and Raichlen, 2001, 2002; Borthwick et al., 2006; Craig, 2006; Madsen and Schäffer, 2010; Dutykh et al., 2011; Dutykh and Kalisch, 2013).

Solitary wave, firstly observed by Russell (1845), is long (infinitely long theoretically, but usually the effective wavelength is discussed) and stable as it propa-

gates in constant depth with permanent form. Boussinesq (1872) first developed the wave profile which is also the exact solution of the Korteweg–de Vries (KdV) equation. Originating from the KdV equation, it is determined typically as

$$\eta(x,t) = A_s \operatorname{sech}^2(K_s(x - c_s t)), \quad K_s = \frac{1}{h}\sqrt{\frac{3A_s}{4h}}, \tag{2.1}$$

in the horizontal coordinate x and time t, where η, A_s, c_s and h denote free surface elevation, wave height of solitary wave, phase velocity of solitary wave and static water depth, respectively. The solution works under the assumption that the nonlinearity ($\varepsilon \equiv A_s/h$) balances with the dispersion ($\mu^2 \equiv h^2/L_s^2$) where L_s denotes the effective wavelength of solitary wave by $L_s = 2\pi/K_s$. Apparently, the two variables A_s and h define the wave uniquely.

Tsunami consists of a group of transient waves which usually disperses into a series of solitary waves if sufficient long propagation distance is given (Hammack, 1973; Goring, 1978; Yeh et al., 1994). Moreover, owing to its stability and permanent form, solitary wave became popular in tsunami science. In fact, solitary wave is relatively easy to generate in laboratory (Goring, 1978), and this is another reason for having attracted great interests.

Notice that the wavenumber K_s obtained from the effective wavelength is tied to amplitude-to-depth ratio A_s/h. However, recent studies such as Madsen et al. (2008) show that wavelength-to-depth ratios of solitary waves are much smaller than those of tsunamis in reality in the respect of the effective wave period T_s and length L_s of solitary waves:

$$T_s = \frac{L_s}{c_s} = \frac{2\pi}{K_s c_s}. \tag{2.2}$$

In other words, the link between the effective wavenumber K_s and wave height A_s from solitary waves does not represent tsunamis in the filed, which motivated this thesis. Madsen et al. (2008) reported that the solitary waves can be 14 times shorter than the incoming wave of the Nicaragua 1992 tsunami. In particular, when tsunamis are approaching the beach, nonlinearity increases significantly,

leading to skewness of waves, which is already beyond the KdV scale.

Madsen et al. (2008) demonstrated that there is not long enough distance in sea for real-world tsunamis to develop into a series of solitary waves. Although, some short waves (solitary-type waves) riding on the main long waves have been found from the 1983 Nihonkai-Chubu tsunami and the 2004 Sumatra tsunami, Liu et al. (1991) reported that no significant effects on the maximum wave run-up height are made by the breaking of these short waves. The short waves do not seriously influence the run-up of the main long waves, and their breaking occurrence before the main wave can mislead the observation (Madsen et al., 2008).

Tsunamis have a variety of waveforms containing wave crests and troughs. The observation of the 2004 Indian Ocean tsunami confirms that the troughs exist in tsunamis (Borthwick et al., 2006). Tadepalli and Synolakis (1994) argued that large drawdown of shoreline at the arrival of trough-led long waves could amplify the run-up of the following positive waves. The findings of the leading-depression waves also question the solitary paradigm as negative waves are hydrodynamically unstable (Madsen et al., 2008).

In conclusion, long wave models have been usually simplified by solitary waves for the recent few decades by neglecting the geophysical relation between wavelength and wave height in reality and the fact that tsunamis are transient, changing and unstable. On the other hand, improvements or alternatives to the model wave have been suggested by a number of researchers. Tadepalli and Synolakis (1994) took the trough into consideration of building the leading tsunami wave by using N-waves, motivated by the findings that drawdown could occur before run-up. Madsen and Schäffer (2010) extended the work by Tadepalli and Synolakis (1994) and proposed a long wave model in which the effective wavelength and the wave height are independent of each other unlike solitary waves.

2.2 Laboratory Experiments

Generating long waves appropriately in laboratory plays an important role in experimentally simulating long wave propagation, run-up and other aspects of wave behaviour near-shore. Many experimental studies have explored the physical characteristics of long waves during their propagation and run-up processes as well as been used for the verification of theoretical models (e.g., Hall and Watts, 1953; Hammack, 1973; Goring, 1978; Synolakis, 1987; Briggs et al., 1995; Liu et al., 1995; Li and Raichlen, 2001; Tonkin et al., 2003; Jensen et al., 2003). However, there is still a lack of knowledge of initial wave profile of tsunamis as the source motion information is too difficult to measure and determine. Thus, the simulated source motions in laboratory were generally simplified. The typical wave makers are grouped into piston-type, paddle-type, bottom-moving type, pneumatic and pipe-driven type.

Since the piston-type wave makers are easily operated and provide approximately uniform flow field vertically, they have been widely used for a few decades to date (e.g., Hall and Watts, 1953; Synolakis, 1986; Zelt, 1991; Grilli et al., 1994; Lin et al., 1999; Li and Raichlen, 2002; Lo et al., 2013). Uniform flow field is an important characteristic of long waves. The generator developed by Hall and Watts (1953) can be regarded as the prototype of the piston-type generator owing to the similar generation mechanism. Later, experimental techniques were improved by employing the hydraulic system and servo-system, which have better performance in controlling the source motions. Goring (1978) and Synolakis (1986) both used an electro-hydraulic servo-system to move a piston attached to a vertical plate horizontally, which can create solitary waves and cnoidal waves in the long tank. The trajectories of the desired piston motions were transformed into voltage signals input in the system. The experimental equipment has been used by many other researchers for long time (e.g. Zelt, 1991; Li, 2000). However, the drawback is that the wavelength of the generated wave is limited by the stroke length L_p as shown in Fig. 2.1. In comparison with the piston-type wave maker, the bottom-tilting wave maker shown in the lower panel has longer moving part,

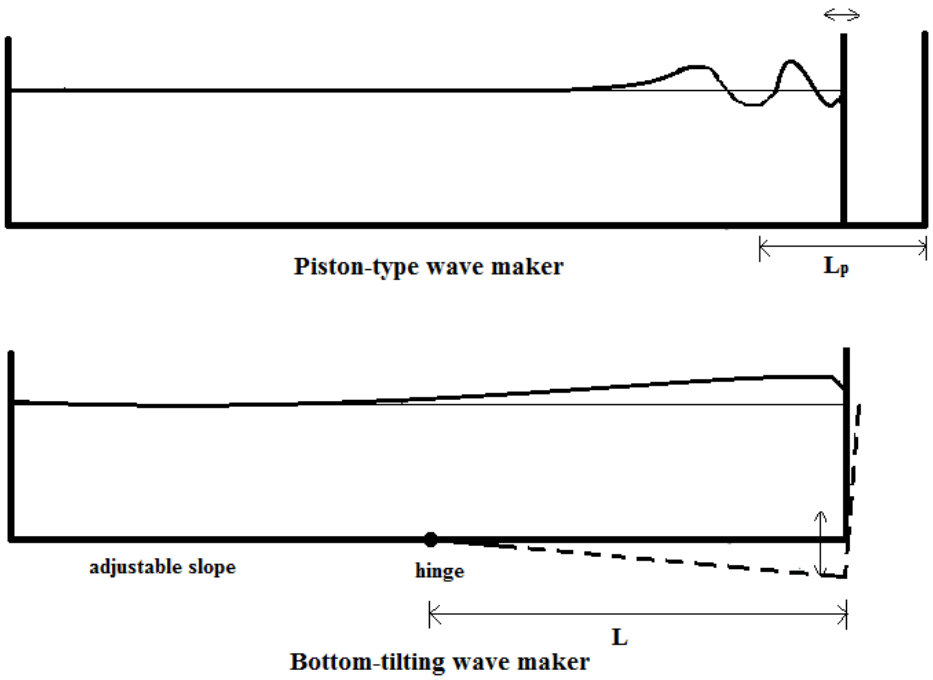

Figure 2.1: Comparison between piston-type wave maker and the bottom-tilting wave maker.

where L denotes the length of the moving bottom. Additionally, the resulting long waves will often disintegrate into shorter ones due to dispersion by the time they arrive at the other end of the tank.

Very few studies mentioned using bottom-wave-generator to simulate tsunami generation or create long waves. The one designed by Hammack (1973) is well known, which was designed for generating solitary waves excited by positive bed motion under the control of a hydraulic servo-system. He found that the generated positive waves by raising up the bottom evolved into solitary waves, whilst the negative waves by lowering the bottom led to a train of dispersive waves. It is noted that waves generated by sudden bottom motion have been studied in the context of impulsive sloshing in a partially-filled tank (e.g., Kit et al., 1987; Liu and Lin, 2008; Tyvand and Miloh, 2012).

Efforts have also been made to develop new kinds of wave makers to generate very long waves in laboratory. Rossetto et al. (2011) used a pneumatic valve-

pump system to release volume of water into wave basin in a controlled manner. However, the inconsistency in determining the extremes between the longer waves and shorter waves reveals the possible problem in controlling the compressible air in the generation box. Goseberg et al. (2013) developed a close-circuit wave flume in which waves are driven by electronically controlled high-capacity pipe pumps. A control loop feedback system enables virtually arbitrary surface profiles. Making use of the re-reflected wave components to generate a target wave longer than the propagation distance is the advantage. The shortcoming is the undesired generation of high-frequency ridding waves which requires better controllability of the control loop feedback system. Additionally for both types, due to the not well described boundary conditions, it is not easy to build theories for these new developed wave makers, though they are not limited by the stroke length.

To date, long-wave generation technique is still limited by imperfect controllability of generating arbitrary waves and space of laboratory restricting long length of equipments. An innovative and economical technique is demanded for scaling realistic tsunamis in laboratory. The concept shown in the lower panel in Fig. 2.1 is used in this thesis, aiming to manage the long wave generation in an easier manner. It is introduced in detail in Chapter 4.

In laboratory, a solitary wave is usually formed as the leading wave which disintegrates from the wave groups and trailed by a series of oscillating waves (Goring, 1978). On the other hand, Liu et al. (1991) suggested that generating a very clean solitary wave is not important since the shape of the leading wave matters more in the run-up motion. During wave propagation, waves usually experience transformation, especially over uneven bottom. Madsen and Mei (1969) reported that a solitary wave can evolve into a series of solitary waves of decreasing amplitudes after passing a slope onto a plane shelf.

The traditional methods of measurement for run-up are to use wave gauge to observe wave surface elevation and video cameras to track the shoreline motion (e.g., Synolakis, 1986; Li, 2000). Synolakis (1986) used resistance-type gauges by steel wires. Li (2000) obtained the water surface time histories in constant

water by a resistance-type wave gauge but a capacitance wave gauge close to the surface of the slope was used for near-shore measurements. Except for the shoreline time history, they also used a high-speed video camera to determine water surface profiles. Moreover, laser-Doppler anemometer (LDA) and particle image velocimetry (PIV) are usually used to observe the velocity field, but not involved in the present study. Briggs et al. (1995) investigated both two-dimensional and three-dimensional long wave run-up in a laboratory channel and a large wave basin. Capacitance type wave gauges and a laser Doppler velocimeter were used to measure the wave evolution and run-up. It would be more difficult to conduct field measurements, for example, Puleo et al. (2000) used a fiber-optic optical backscatter sensor system, a pressure sensor and two current meters to set up only one instrument bar and measure the sea surface elevation.

Hall and Watts (1953) firstly investigated the run-up of solitary waves in laboratory by using a pusher type wave generator and determined the maximum run-up height as a function of beach slope and wave height. To improve the empirical formulas of the maximum run-up height (R_m) proposed by the early researches((e.g., Hall and Watts, 1953)), Synolakis (1986) established the relation by nonlinear wave theory

$$\frac{R_m}{h} = 2.831\sqrt{\cot\beta}(\frac{A_s}{h})^{5/4}, \tag{2.3}$$

for non-breaking waves and

$$\frac{R_m}{h} = 0.918(\frac{A_s}{h})^{0.606}, \tag{2.4}$$

for breaking waves with theoretical validation where β denotes the angle of the slope. The relations were verified by their measurements on a slope of 1/19.85 and then used widely by many other researchers for validating their experiments or theories. In addition to the maximum run-up height formula, Synolakis (1986) also empirically concluded the breaking criterion by $A_s/h = 0.818(\cot\beta^{-10/9})$ to identify the non-breaking region.

2.3 Theoretical modelling

The relative importance of nonlinearity and frequency dispersion is varying along with the changing and complicated bathymetry. Hence, linear or nonlinear shallow water equations can be employed according to whether nonlinearity is ignored or not. However, in practice, both nonlinearity and frequency dispersion should be considered during the main part of wave evolution, especially wave propagation. It could be very challenging to model the complicated wave behaviour, in particular the wave breaking since waves post-breaking are still not well determined by now. The following review involves some of the simplified models concerning the evolution of long waves in shallow water.

In early stage, people evaluated the wave motion from the linear wave theory in tsunami studies. For instance, Kajiura (1963), Keller and Keller (1964), Tuck and Hwang (1972) and Synolakis (1987) have proposed the linear solutions to approximate near and far field waves. Keller and Keller (1964) firstly solved the wave run-up with the bathymetry of a uniform sloping beach connected with constant-depth water based on linear non-dispersive shallow water equations. Mei (1989) described the analytical solutions to linear shallow water equations for waves generated by surface disturbance. Based on his method, the analytical solutions are obtained for the new wave tank, which will be introduced in detail in Section 3.1.1. Zhang (1996) derived the linear solution for the three-dimensional run-up by Fourier synthesis. Although the linear wave theory is limited to situations where nonlinear effects are small for both near and far field waves, it can be used as first approximation tool to estimate long waves.

On the other hand, frequency dispersion is of great importance during wave generation and propagation when pressure cannot be assumed hydrostatic. Many studies have shown that dispersive models have good performances on long wave simulation (e.g., Peregrine, 1967; Zelt, 1991; Borthwick et al., 2006; Dutykh et al., 2011; Dutykh and Kalisch, 2013). Hence, Boussinesq equations become a good choice to demonstrate the evolution of the surface waves, meanwhile both dispersion and nonlinearity are considered on the basis that they are both small and

of the same order of magnitude. Zelt (1991) used a Lagrangian finite-element method to solve the Boussinesq equations and investigated the run-up of both non-breaking and breaking solitary waves.

Dutykh et al. (2011) introduced a variety of Boussinesq-type wave systems, among which some are applicable for flat bottom and some for arbitrary bottom. In this work, time-dependent bathymetry variations have to be coupled with surface wave. Therefore, the two-dimensional Boussinesq system derived by Wu (1987) for dynamic bathymetry is employed:

$$\left.\begin{aligned} &\eta_t + ((h+\eta)u)_x + h_t = 0, \\ &u_t + g\eta_x + uu_x = \tfrac{1}{2}h(h_t + (hu)_x)_{xt} - \tfrac{1}{6}h^2 u_{xxt}, \end{aligned}\right\} \tag{2.5}$$

which is an extension of the classical Boussinesq systems where subscripts denote partial differentiation, u and g denote depth-averaged fluid velocity in horizontal direction and gravitational acceleration, respectively. The introduction of the numerical model developed by the Boussinesq equations (2.5) in this study can be found in Section 3.1.3.

Nonlinearity plays a key role in wave run-up process in shallow water, so that nonlinear shallow water equations have been commonly used (e.g., Liu et al., 1995; Titov and Synolakis, 1995; Dodd, 1998; Li and Raichlen, 2002; Madsen and Schäffer, 2010). Based on the conservation of mass and momentum, the classical nonlinear shallow water (NSW) equations read

$$\left.\begin{aligned} &\eta_t + ((h+\eta)u)_x + h_t = 0, \\ &u_t + uu_x + g\eta_x = 0. \end{aligned}\right\} \tag{2.6}$$

The velocity is assumed uniform in the vertical direction with hydrostatic pressure field. The numerical model developed by the nonlinear shallow water equations in this study is introduced in Section 3.2.2.

Carrier and Greenspan (1958) adopted the hodograph transformation to the NSW equations and transformed them into a single linear equation. Then, they proposed the analytical solutions to the NSW equations and solved the run-up of

the monochromatic waves climbing a beach with constant slope. This method has been discussed in section 3.2.1. Synolakis (1987) extended the theory by Carrier and Greenspan (1958) for solving the run-up of non-breaking solitary waves on a plane beach connected with a constant-water region and deriving the breaking criterion. Their analytical solutions agreed to the experiments for non-breaking waves.

Breaking of waves scatters wave energy, which influences wave run-up seriously (Li, 2000). Due to the complexity of wave breaking, it is usually simplified. In the past, long periodic waves were used to explore the breaking wave run-up. Later, Synolakis (1986) has pointed out that a bore can be regarded as a long breaking wave as it does not change to a non-breaking wave over considerable distances. Li (2000) demonstrated that propagating bores can be used to model the waves post-breaking as they are analogous to the shocks in gas dynamics. Physically, bores are water waves generated by tidal motions and moving upstream in the form of hydraulic jumps. Chanson (2005) discovered the development of the tidal in the Baie du Mont Saint Michel and found a breaking front in shallow water. Moreover, the tidal behaviour of propagating inland they observed is similar to tsunamis.

2.4 Numerical methods

A wide range of numerical methods are developed in solving these hyperbolic equations, such as finite difference methods, finite element methods, finite volume methods and boundary-element methods. Finite difference methods are very commonly used for quite a long time. Zhang (1996) derived Lax-Wendroff finite difference method to solve the NSW equations for non-breaking solitary wave run-up. Finite volume methods are also popular since it is good at solving conservative equations with high efficiency, accuracy and robustness owing to its conservation and shock-capturing properties (Dutykh and Kalisch, 2013). It is used for discretisation in this study as demonstrated in Section 3.2.2. Borthwick et al.

(2006) applied the Godunov-type shock-capturing finite-volume scheme to solved the Boussinesq-type equations pre-breaking and non-linear shallow water equations post-breaking for solitary wave run-up. To consider bottom disturbance, Dutykh and Kalisch (2013) used a finite volume scheme to solve the Boussinesq equations for modelling surface waves caused by underwater landslides. Their numerical results have a good agreement with not only solitary wave propagation and interaction theoretically but also some experimental measurements. The boundary-element method performs well in modelling two or three-dimensional wave problems with only the boundary values required. Grilli et al. (1997) developed a boundary element technique for solving the wave model based on the full potential water-wave theory for solitary wave motions.

How to deal with the discontinuity of discrete solution at the cell interfaces is of key importance in solving numerical models, in particular the shocks and complicated region involved in the problems. In particular, for breaking waves, there will be numerical instabilities near the discontinuities due to the numerical oscillations of the solution. One of the methods to resolve the oscillations is to add additional ad-hoc terms as breaking terms that increases the dissipation. The other method is to employ limiters to suppress oscillation, for example, the total variation diminishing (TVD) scheme proposed by Sweby (1984). Nevertheless, the accuracy is reduced at the local extrema. To improve the TVD schemes, uniformly non-oscillatory (UNO) (Harten and Osher, 1987) scheme was constructed to remain high order accuracy at the local extrema.

Another way of obtaining non-oscillatory solutions near the discontinuities is the essentially non-oscillatory (ENO) schemes which was constructed by Shu and Osher (1988). The ENO schemes use an adaptive stencil to automatically resolve the discontinuities with a sharp, essentially non-oscillatory shock transition captured. In addition, ENO schemes are uniformly high order accurate. Furthermore, the weighted ENO (WENO) schemes are developed by a convex combination of all candidate stencils, as an improvement of the ENO schemes (Liu et al., 1994; Jiang and Shu, 1996). The WENO schemes have been used in many studies (e.g., Li and Raichlen, 2002; Xing and Shu, 2005; Shen et al., 2011; Wang

et al., 2015) as well as the present study. Thus, either UNO scheme or WENO scheme uses adaptive stencil to interpolate the numerical flux and keep the piecewise polynomial representations always non-oscillatory. The schemes used in this study (UNO and WENO) are reviewed in detail in section 3.1.3.

Dutykh et al. (2011) reviewed three methods of numerical flux functions. Among the three, the easiest way is to average the flux functions of the two adjacent cells in terms of computational speed, but it is not stable for nonlinear conservative equations. The central flux, as a Lax-Friedrichs type flux, is chosen in this work and described in detail in Section 3.1.3 and Eq. (3.46). Li and Raichlen (2002) and Xing and Shu (2005, 2006) used Lax-Friedrichs flux splitting, which shows a good performance in computation.

Beach surface roughness and bottom friction are important in determining wave run-up. Bottom friction has been included in many numerical studies, as well considered in the present study. The bottom friction term is usually presented quadratic in the horizontal water velocity which is discussed further in the last paragraph in section 3.2.2. Borthwick et al. (2006) considered both breaking and bottom friction terms in the numerical model based on the Boussinesq equations solved by a finite-volume scheme. They obtained the results which well agreed to the experimental data. The disadvantages are loss of accuracy and that calibrations are required before actual applications.

Furthermore, theoretical treatment of the moving shoreline became a difficulty in modelling wave run-up. In Eulerian perspective, the grid points in the computational domain are changing dynamically (increase during run-up but decrease during run-down) according to the shoreline motion (e.g., Hibberd and Peregrine, 1979; Titov and Synolakis, 1998; Dodd, 1998; Lynett et al., 2002). Hibberd and Peregrine (1979) applied a predictor scheme to predict whether the shoreward boundary is wet or not in order to adjust the number of the grip points. Lynett et al. (2002) applied linear extrapolation near the shoreline (wet–dry) boundary for their high-order model. The other way to treat the dynamic shoreline is to employ the Lagrangian coordinates (e.g., Pedersen and Gjevik, 1983; Zelt and

Raichlen, 1990; Zhang, 1996; Li and Raichlen, 2002). Zhang (1996) developed a scheme to remap the grid points based on the prediction of the shoreline position without changing the number of the grid points in his finite difference method to study the run-up of non-breaking waves. This computational domain mapping technique is used in the present study as shown in Eq.3.78.

Chapter 3

Theoretical modelling

This chapter involves the theoretical solutions and the numerical modelling of the long wave behaviour in the new wave tank as well as the validation of all the theoretical models. It is noted that as the wave tank is narrow, the resulting waves are regarded as two-dimensional. As a potential-flow free surface problem, the flow is under the assumptions of being inviscid, incompressible and irrotational in this study. The analytical solutions are only applicable to non-breaking waves. The two numerical models are built for wave generation and run-up, respectively. These are reported in the recent publication (Lu et al., 2017).

Fig. 3.1 shows the schematic sketch of the two-dimensional wave tank with a bottom moving in a combined rotating and lifting manner. Therefore, the analysis is divided into two parts at the toe of the slope (hinge). The moving bottom part will generate long waves, and the other part is for the generated waves propagating in the constant water depth (Section 3.1) or running up the slope (Section 3.2).

3.1 Theories for wave generation

In this section focusing on wave generation, slope is not considered. The co-ordinate system shown in Fig. 3.1 originates at the end wall of the generation

part, meanwhile the positive x axis is pointing the other end wall and z axis is pointing upwards. Thus, the fluid domain is bounded by the two end walls, the free surface and the bottom solid boundary, while the latter two are defined as $z = \eta(x,t)$ on the surface measured from the still water line $z = 0$ and $z = -h(x,t)$ at the bottom, respectively. For $0 < x < L$, water depth is expressed by $h(x,t) = h_0 + \zeta(x,t)$, where ζ, L and h_0 denote the bottom motion displacement measured from the left still bottom, length of the moving bottom and the constant water depth, respectively.

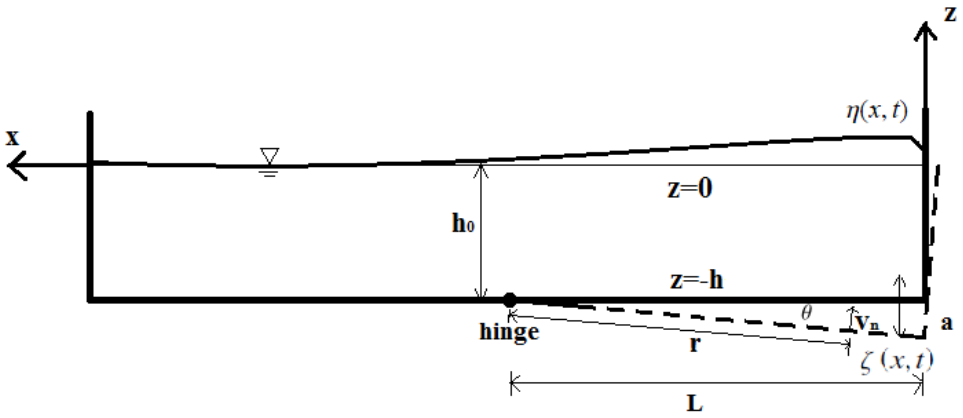

Figure 3.1: Sketch of the two-dimensional wave maker.

The Ursell parameter $U_r = (A/h)(kh)^{-2} = \varepsilon/\mu^2$ can be used to demonstrate the relation between nonlinearity ε and dispersion μ^2, where $\varepsilon = A/h$ and $\mu = kh$ with A and k denoting wave amplitude and wavenumber, respectively. The analytical solutions by linear wave theory are useful when $\varepsilon \ll 1$. But in fact, ε is not small in this shallow-water tank, so linear wave theory cannot describe the resulting waves accurately. Moreover, dispersion can be important during wave generation and propagation. If both nonlinearity and dispersion are taken into consideration, Boussinesq equations can be a good choice under the condition that the fluid should satisfy $O(\varepsilon) = O(\mu^2) < 1$. However, if $\varepsilon/\mu^2 \gg 1$, NSW equations can describe the fluid motion more practically.

3.1.1 Preliminary estimation by linear wave theory

Linear wave theory (LT) is useful for quick estimate of the generated waves, although limited by the conditions that it applies to non-breaking waves and where nonlinear effects are small.

The fluid motion in the wave tank (in the x, z plane) can be described by the two-dimensional Laplace's equation along with the appropriate boundary conditions. With Φ denoting the velocity potential ($u = \nabla\Phi$), the continuity equation reads

$$\nabla^2\Phi = \frac{\partial^2\Phi}{\partial x^2} + \frac{\partial^2\Phi}{\partial z^2} = 0, \tag{3.1}$$

where the operator ∇ denotes the gradient.

Aside from the two ends, the boundaries of the fluid in the wave tank are air-water free surface and water-solid bottom, where there is simply the tangential motion of the flow. Thus, two kinematic boundary conditions are added on the free surface and the bottom solid which are expressed by

$$\frac{\partial\Phi}{\partial z} = \frac{\partial\eta}{\partial t} + \frac{\partial\Phi}{\partial x}\frac{\partial\eta}{\partial x}, \quad z = \eta(x,t), \tag{3.2}$$

$$\frac{\partial\Phi}{\partial z} = \frac{\partial\zeta}{\partial t} + \frac{\partial\Phi}{\partial x}\frac{\partial\zeta}{\partial x}, \quad z = -h_0 + \zeta(x,t). \tag{3.3}$$

Then, according to the Bernoulli equation, a dynamical boundary condition is added on the free surface as well by

$$\frac{\partial\Phi}{\partial t} + \frac{1}{2}|\nabla\Phi|^2 + g\eta = 0, \quad z = \eta(x,t), \tag{3.4}$$

where the surface tension and the direct atmosphere forcing are assumed to be negligible.

The nonlinear terms and the not well located free surface make it difficult to solve the equations analytically. Later in the next subsection, the nonlinear terms will be taken into consideration in the numerical models based on the Boussinesq equations or the nonlinear shallow water equations.

Here, linearisation is employed by introducing the dimensionless variables (denoted by prime) which are normalised by the corresponding physical scales for being of order unity as Mei (1989) suggested

$$\begin{pmatrix} \Phi \\ x, z, h \\ t \\ \eta, \zeta \end{pmatrix} = \begin{pmatrix} A\omega L_w \Phi'/2\pi \\ L_w(x', z', h')/2\pi \\ t'/\omega \\ A(\eta', \zeta') \end{pmatrix}, \tag{3.5}$$

then the governing equation and boundary conditions are non-dimensionalised as

$$\nabla'^2\Phi' = \frac{\partial^2\Phi'}{\partial x'^2} + \frac{\partial^2\Phi'}{\partial z'^2} = 0, \quad -h' < z' < \varsigma\zeta', \tag{3.6}$$

$$\frac{\partial\Phi'}{\partial z'} = \frac{\partial\eta'}{\partial t'} + \varsigma\frac{\partial\Phi'}{\partial x'}\frac{\partial\eta'}{\partial x'}, \quad z' = \varsigma\eta', \tag{3.7}$$

$$\frac{\partial\Phi'}{\partial t'} + \frac{\varsigma}{2}(\nabla'\Phi')^2 + (\frac{2\pi g}{\omega^2 L_w})\eta' = 0, \quad z' = \varsigma\eta'. \tag{3.8}$$

$$\frac{\partial\Phi'}{\partial z'} = \frac{\partial\zeta'}{\partial t'} + \varsigma\frac{\partial\Phi'}{\partial x'}\frac{\partial\zeta'}{\partial x'}, \quad z' = -h_0 + \varsigma\zeta'. \tag{3.9}$$

where $\varsigma = 2\pi A/L_w$ with L_w and ω are wavelength and angular frequency, respectively.

Small-amplitude waves imply that ς could be very small. Retaining only the linear terms, the governing equation and the boundary conditions are linearised as below

$$\nabla^2\Phi = 0, \quad -h_0 < z < 0 \tag{3.10}$$

$$\frac{\partial\eta}{\partial t} = \frac{\partial\Phi}{\partial z}, \quad z = 0, \tag{3.11}$$

$$\frac{\partial\Phi}{\partial t} + g\eta = 0, \quad z = 0, \tag{3.12}$$

$$\frac{\partial\Phi}{\partial z} = \frac{\partial\zeta}{\partial t}, \quad z = -h_0, \tag{3.13}$$

with physical variables, where the free surface and the bottom are known now by simplifying them as $z = 0$ and $z = -h_0$, respectively. Hence, the accuracy of this linear approximation depends on the magnitude of the parameter ς.

However, under the assumption that the moving bed is flat, solid and impermeable, the fluid velocity normal to the bed v_n as shown in Fig. 3.1 is just the same as that of the moving bottom. Thus, the bottom boundary condition becomes

$$v_n = r\frac{\partial \theta}{\partial t}, \tag{3.14}$$

where r and θ denote the rotating radius and angle, respectively. In Fig. 3.1, the radius r can be described as $r = (L-x)\sqrt{1+\tan^2\theta}$ with $0 < x < L$. Since v_n also can be described as

$$v_n = w\cos\theta + u\sin\theta, \tag{3.15}$$

which leads to

$$(L-x)\sqrt{1+\tan^2\theta}\frac{\partial \theta}{\partial t} = w\cos\theta + u\sin\theta, \tag{3.16}$$

where u and w are the horizontal and vertical components of v_n, respectively. For small θ, these simplifications can be found: $w\cos\theta \approx w$, $u\sin\theta \approx 0$, $\tan^2\theta \ll 1$ and $\theta \approx \zeta(x,t)(L-x)^{-1}$, hence the left-hand side of (3.16) approximates $\partial\zeta/\partial t$. As a result, the bottom boundary condition (3.13) becomes

$$\frac{\partial \Phi}{\partial z} = \frac{\partial \zeta}{\partial t} = W(x,t), \quad z = -h_0, \tag{3.17}$$

where W is the vertical velocity given by the actuator with $W = w$.

In the present study, the bottom motion is of finite duration, which can excite the fluid and produce transient waves. Following the method by Mei (1989), the Laplace transform in t (denoted by $^-$) is applied firstly, which gives

$$\nabla^2\bar{\Phi}(x,z,s) = 0, -h_0 < z < 0, \tag{3.18}$$

$$\frac{\partial \bar{\Phi}}{\partial z} = \bar{W}(x,s), z = -h_0, \tag{3.19}$$

and

$$\frac{\partial \bar{\Phi}}{\partial z} + \frac{s^2}{g}\bar{\Phi} = -\eta(x,0) + \frac{s^2}{g}\Phi(x,0,0), z = 0. \tag{3.20}$$

Note that Eq. (3.20) is obtained by combing Eq. (3.11) and Eq. (3.12). Since it is

assumed that only bottom motion is considered and no initial surface disturbance, the initial condition is determined as $\eta(x,0) = \Phi(x,0) = 0$. Moreover, $\Phi \to 0$ is assumed where it is very far away from the initial disturbance within finite t, which also implies that $\bar{\Phi} \to 0$ as $\mid x \mid \to \infty$. Then, the Fourier transform in x (denoted by $\tilde{}$) is applied and leads the equations

$$\frac{\mathrm{d}^2\tilde{\bar{\Phi}}}{\mathrm{d}z^2} - k^2\tilde{\bar{\Phi}} = 0, \quad -h_0 < z < 0, \tag{3.21}$$

$$\frac{\mathrm{d}\tilde{\bar{\Phi}}}{\mathrm{d}z} + \frac{s^2}{g}\tilde{\bar{\Phi}} = 0, \quad z = 0, \tag{3.22}$$

$$\frac{\mathrm{d}\tilde{\bar{\Phi}}}{\mathrm{d}z} = \tilde{\bar{W}}, \quad z = -h_0. \tag{3.23}$$

Now, the velocity potential is given in the form

$$\Phi\left(x,z,t\right) = \frac{1}{2\pi}\int_{-\infty}^{\infty}\mathrm{d}k\, e^{ikx}\frac{1}{2\pi i}\int_{\Gamma}\mathrm{d}s\, e^{st}\tilde{\bar{\Phi}}\left(k,z,s\right), \tag{3.24}$$

with the solution of the transformed velocity potential

$$\tilde{\bar{\Phi}} = \frac{\tilde{\bar{W}}(s^2\sinh kz - gk\cosh kz)}{k(s^2+\omega^2)\cosh kh_0}, \tag{3.25}$$

where $\omega^2 = gk\tanh kh_0$ and i is the imaginary unit. Finally, by substituting Eq. (3.24) into Eq. (3.12), the solution for the free surface elevation resulting from general bottom motion is obtained as

$$\eta\left(x,t\right) = \frac{1}{2\pi}\int_{-\infty}^{\infty}\mathrm{d}k\frac{e^{ikx}}{\cosh kh_0}\frac{1}{2\pi i}\int_{\Gamma}\mathrm{d}s\frac{s\tilde{\bar{W}}e^{st}}{s^2+\omega^2}. \tag{3.26}$$

To apply the solution (3.26) for the bottom tilting wave maker, the domain is regarded as unbounded ($-\infty < x < \infty$) with the bottom motion centred and symmetric with respect to the vertical axis at $x = 0$ as shown in Fig. 3.2 (a). Due to the symmetry, only half of the motion is considered in the later experiments and the numerical models from $x = 0$ to $x = L$ as shown in Fig. 3.1. Accordingly,

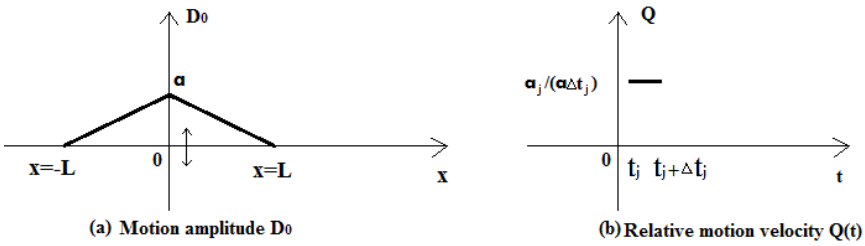

Figure 3.2: Sketch of the tilting bottom motion in unbounded domain.

the complete bottom motion displacement is given by

$$\zeta(x,t) = D_0(x)\, B(t)\,, \tag{3.27}$$

where the motion amplitude D_0 is presented as

$$D_0(x) = \begin{cases} a - \dfrac{a}{L}|x|\,, & -L \le x \le L, \\ 0, & x < -L \quad \text{and} \quad x > L, \end{cases} \tag{3.28}$$

with a denoting the motion amplitude at $x = 0$.

Then, Eq. (3.17) becomes

$$\frac{\partial \Phi}{\partial z} = \frac{\partial \zeta}{\partial t} = W(x,t) = D_0(x)\, Q(t)\,, \tag{3.29}$$

where relative velocity Q is

$$Q(t) = \frac{\mathrm{d}B}{\mathrm{d}t}, \tag{3.30}$$

which is shown in Fig. 3.2 (b) for example at a time-point t_j with a time-step Δt_j.

Taking Fourier transformation of (3.28),

$$\tilde{D}_0(k) = \int_{-\infty}^{\infty} D_0(x)\, e^{-ikx}\mathrm{d}x = aL\frac{\sin^2(kL/2)}{(kL/2)^2}. \tag{3.31}$$

in which it is made use of the fact that $D_0(x)$ is an even function.

It is straightforward to calculate the solution for impulsive bottom motion,

namely, $Q(t) = \delta(t)$, for example. It leads to

$$\tilde{\bar{W}} = \bar{D}(k)\tilde{Q}(s) = aL\frac{\sin^2(kL/2)}{(kL/2)^2}. \tag{3.32}$$

Then the s integral of the solution (3.26) can be evaluated by the two real poles at $s = \pm i\omega$:

$$\frac{1}{2\pi i}\int_\Gamma \frac{se^{st}\mathrm{d}s}{s^2+\omega^2} = \cos\omega t. \tag{3.33}$$

Furthermore, if it is supposed that the sudden bottom motion is initiated at time $t = t_1$ by a_1 as shown in Fig. 3.2 (b) when i=1, $Q(t_1) = (a_1/a)\delta(t_1)$ and Δt_1 is very small, $\tilde{\bar{W}}$ would be

$$\tilde{\bar{W}} = \bar{D}(k)\tilde{Q}(s) = a_1 L\frac{\sin^2(kL/2)}{(kL/2)^2}e^{-st_1}. \tag{3.34}$$

Then, the s integral follows as

$$\frac{1}{2\pi i}\int_\Gamma e^{-st_1}\frac{se^{st}\mathrm{d}s}{s^2+\omega^2} = \begin{cases} 0, t < t_1 \\ \cos\omega(t-t_1), t \geq t_1. \end{cases} \tag{3.35}$$

Similarly, if the bottom consists of multiple step functions with amplitudes $a_1, a_2, \cdots a_n$ at $t = t_1, t_2, \cdots t_n$, respectively, the solution of $\eta(x,t)$ would be

$$\eta(x,t) = \frac{1}{2\pi}\int_{-\infty}^{\infty} L\frac{\sin^2(kL/2)}{(kL/2)^2}\frac{e^{ikx}}{\cosh kh_0}\left(\sum_{j=1}^{N} a_j\cos\omega(t-t_j)\right)\mathrm{d}k. \tag{3.36}$$

The solution for general bottom motion, $Q(t) = \int_0^t Q(u)\delta(t-u)\,\mathrm{d}u$, is obtained as a superposition of the impulsive motions:

$$\eta(x,t) = \frac{aL}{\pi}\int_0^t \mathrm{d}u\int_0^\infty \mathrm{d}k\,\frac{\sin^2(kL/2)}{(kL/2)^2}\frac{\cos kx}{\cosh kh_0}Q(u)\cos\omega(t-u), \tag{3.37}$$

which was also shown in Miles (1962). Note that the solution covers the domain from $x = 0$ to $x = \infty$ will be described as semi-infinite domain in the following discussions. This restricts the solution valid to the wave information during the time or at the location that the waves are not affected by the reflection from the boundary at $x = 2L$. More practical estimation for the bounded wave tank is

based on the numerical modelling in Section 3.1.3 and 3.2.2. However, it also extends the experimental investigation of exploring the waves with infinite long distance to propagate. Furthermore, the solution will be used in Eq. (3.70) and (3.71) as the incident wave information for approximating run-up height.

3.1.2 Inversion calculation of the reflected waves

On the other hand, this extremely long wave will experience immediate reflections from both ends of the tank, and therefore controlling reflections would be important in this kind of wave tank. Although the reflection does not affect the observed wave features (first wave peak or nadir) in this study, it should be discussed for further research. One way to solve this problem is to obtain the corresponding bottom motion of the unwanted reflection waves.

Eq. (3.37) can be expressed in convolution form

$$\eta\left(x,t\right) \ = \frac{aL}{\pi}\int_0^t Q\left(u\right)\Upsilon\left(t-u\right)\mathrm{d}u = Q * \Upsilon. \tag{3.38}$$

where asterisk denotes convolution and

$$\Upsilon(x,t) = \frac{aL}{\pi}\int_0^\infty \frac{\sin^2\left(kL/2\right)}{\left(kL/2\right)^2}\frac{\cos kx}{\cosh kh}\cos\omega t\ \mathrm{d}k. \tag{3.39}$$

By the convolution theorem

$$F\left\{\eta\right\} = F\left\{Q * \Upsilon\right\} = F\left\{Q\right\}\cdot F\left\{\Upsilon\right\}, \tag{3.40}$$

where F denotes Fourier transform operator and dot denotes point-wise multiplication. The Fourier transformed bottom motion velocity $F\{Q\}$ can be acquired easily: $F\{Q\} = F\{\eta\}/F\{\Upsilon\}$. At last, the bottom motion velocity Q can be obtained by inversely Fourier transforming $F\{Q\}$.

Therefore, given the information of the reflected wave of free surface elevation which can be measured by subtracting the practical wave information (influenced

by reflection) by the wanted singe wave information, the corresponding bottom motion can be estimated. Then, theoretically, these unwanted reflections are counteracted by generating the waves in opposite direction. The ability of estimation will be tested and further explained in Section 3.3.2.

3.1.3 Numerical model in consideration of nonlinearity and dispersion

As a more rigorous approach, the weakly dispersive and weakly nonlinear wave theory is used to model the wave tank. The one-dimensional Boussinesq equations (BE) derived by Wu (1987) are rewritten in conservative form as below

$$\left.\begin{aligned} &H_t + [Hu]_x = 0, \\ &u_t + [\tfrac{1}{2}u^2 + g(H-h)]_x = \tfrac{1}{2}hh_{xtt} + \tfrac{1}{2}h(hu)_{xxt} - \tfrac{1}{6}h^2u_{xxt}, \end{aligned}\right\} \tag{3.41}$$

where $H = \eta + h$, which also can be rearranged in the form (Dutykh et al., 2011; Dutykh and Kalisch, 2013):

$$\mathbf{V}_t + [\mathbb{F}(\mathbf{V})]_x = \mathbb{S} + \mathbb{M}(\mathbf{V}), \tag{3.42}$$

where the variable V, the advective flux $\mathbb{F}(\mathbf{V})$, the source term $\mathbb{S}$ and the dispersive term $\mathbb{M}(\mathbf{V})$ are denoted respectively by $\mathbf{V} = \begin{pmatrix} H \\ u \end{pmatrix}$, $\mathbb{F}(\mathbf{V}) = \begin{pmatrix} Hu \\ \frac{1}{2}u^2 + g(H-h) \end{pmatrix}$, $\mathbb{S} = \begin{pmatrix} 0 \\ \frac{1}{2}hh_{xtt} \end{pmatrix}$ and $\mathbb{M}(\mathbf{V}) = \begin{pmatrix} 0 \\ \frac{1}{2}h(hu)_{xxt} - \frac{1}{6}h^2u_{xxt} \end{pmatrix}$.

The computational domain is discretised uniformly into cells $C_i = \left[x_{i-\frac{1}{2}}, x_{i+\frac{1}{2}}\right]$ with the center-point of a cell C_i being $x_i = \frac{1}{2}\left(x_{i-\frac{1}{2}} + x_{i+\frac{1}{2}}\right)$ $(i \in \mathbb{Z})$ while Δx_i regarded as the length of the cell. Hence, $x_{i-\frac{1}{2}}$ is the left boundary of cell C_i while $x_{i+\frac{1}{2}}$ is the right boundary. After the finite volume discretisation, the equations become

$$\frac{\mathrm{d}\bar{\mathbf{V}}_i}{\mathrm{d}t} + \frac{1}{\Delta x}[\mathbb{F}(\mathbf{V}(x_{i+\frac{1}{2}})) - \mathbb{F}(\mathbf{V}(x_{i-\frac{1}{2}}))] = \bar{\mathbb{S}}_i + \bar{\mathbb{M}}_i, \tag{3.43}$$

where $\bar{\mathbf{V}}_i(t) = \frac{1}{\Delta x}\int_{C_i} \mathbf{V}(x,t)\mathrm{d}x$ is regarded as cell average, so as the source term and the dispersive term. To deal with the discontinuity at cell interfaces in the discrete solution, numerical flux functions are replaced at the cell interfaces by

$$\mathbb{F}(\mathbf{V}(x_{i\pm\frac{1}{2}},t)) \approx \mathbb{F}_{i\pm\frac{1}{2}}(\bar{\mathbf{V}}^L_{i\pm\frac{1}{2}}, \bar{\mathbf{V}}^R_{i\pm\frac{1}{2}}), \tag{3.44}$$

where $\bar{\mathbf{V}}^{L,R}_{i\pm\frac{1}{2}}$ represent the high-order reconstructions of the variables $\bar{\mathbf{V}}$ with both left (L) and right (R) sides of each cell interface approximated. Hence, the conservative scheme becomes

$$\frac{\mathrm{d}\bar{\mathbf{V}}_i}{\mathrm{d}t} + \frac{1}{\Delta x}[\mathbb{F}_{i+\frac{1}{2}} - \mathbb{F}_{i-\frac{1}{2}}] = \bar{\mathbb{S}}_i + \bar{\mathbb{M}}_i. \tag{3.45}$$

For a stable scheme, the Lax-Friedrichs numerical flux is chosen among many other numerical fluxes in the present study as it is simple and inexpensive (Xing and Shu, 2006). The Lax-Friedrichs numerical flux function used for $\mathbb{F}$ is given by

$$\mathcal{F}(\mathbf{V},\mathbf{W}) = \frac{1}{2}\{[\mathbb{F}(\mathbf{W}) + \mathbb{F}(\mathbf{V})] - \mathbb{U}(\mathbf{V},\mathbf{W})[\mathbf{W}-\mathbf{V}]\}. \tag{3.46}$$

with the operator $\mathbb{U}$ defined as

$$\mathbb{U}(\mathbf{V},\mathbf{W}) = \max[\chi(DF(\mathbf{V})), \chi(DF(\mathbf{W}))], \tag{3.47}$$

where DF denotes the Jacobian matrix and $\chi(I)$ is the spectral radius of I.

For the purpose of achieving higher order approximations to $\mathbf{V}(x_{i\pm\frac{1}{2}},t)$, a piecewise polynomial representation called UNO2 (Harten and Osher, 1987) is introduced which has a good performance as being of second order accuracy and results in small dissipation in wave computation. On the other hand, WENO type reconstruction can lead to higher order accuracy, for example, 3rd order accurate WENO3 and 5th order accurate WENO5 (Shu, 1998). The high-order reconstruction schemes UNO2, WENO3 and WENO5 are described briefly following the summarised instructions and reviews (Dutykh et al., 2011; Xing and Shu, 2006) as below.

UNO2

$\mathbf{V}^L_{i+\frac{1}{2}}$ and $\mathbf{V}^R_{i+\frac{1}{2}}$ are respectively defined by

$$\mathbf{V}^L_{i+\frac{1}{2}} = \mathbf{V}_i + \frac{1}{2}\mathbf{G}_i, \quad \mathbf{V}^R_{i+\frac{1}{2}} = \mathbf{V}_{i+1} - \frac{1}{2}\mathbf{G}_i, \tag{3.48}$$

where

$$\begin{aligned}
&\mathbf{G}_i = m(\mathbf{G}_i^+, \mathbf{G}_i^-), \quad \mathbf{G}_i^{\pm} = \nu_{i\pm\frac{1}{2}} \mp \frac{1}{2}\mathcal{D}_{i\pm\frac{1}{2}}, \\
&\nu_{i\pm\frac{1}{2}}(\mathbf{V}) = \mathbf{V}_{i+1} - \mathbf{V}_i, \quad \mathcal{D}_{i\pm\frac{1}{2}} = m(\mathcal{D}_i, \mathcal{D}_{i+1}), \\
&\mathcal{D}_i(\mathbf{V}) = \mathbf{V}_{i+1} - 2\mathbf{V}_i + \mathbf{V}_{i-1}, \quad m(x,y) = \frac{1}{2}(\text{sign}(x) + \text{sign}(y))\min(|x|, |y|),
\end{aligned}$$

and $m(x, y)$ denotes the minmod function as a limiter in UNO2 scheme.

WENO3

Firstly, scheme WENO3 is introduced, with WENO5 followed in the next part. Before computing a WENO3 scheme with the accuracy of $2\xi - 1 = 3$ when $\xi = 2$, the reconstructed values are defined as

$$\left.\begin{aligned}
\mathbf{V}^{(0)}_{i+\frac{1}{2}} &= \tfrac{1}{2}(\mathbf{V}_i + \mathbf{V}_{i+1}), \quad \mathbf{V}^{(1)}_{i+\frac{1}{2}} = \tfrac{1}{2}(-\mathbf{V}_{i-1} + 3\mathbf{V}_i), \\
\mathbf{V}^{(0)}_{i-\frac{1}{2}} &= \tfrac{1}{2}(3\mathbf{V}_i - \mathbf{V}_{i+1}), \quad \mathbf{V}^{(1)}_{i-\frac{1}{2}} = \tfrac{1}{2}(\mathbf{V}_{i-1} + \mathbf{V}_i).
\end{aligned}\right\} \tag{3.49}$$

Then, the smoothness indicators are presented as

$$\beta_0 = (\mathbf{V}_{i+1} - \mathbf{V}_i)^2, \quad \beta_1 = (\mathbf{V}_i - \mathbf{V}_{i-1})^2, \tag{3.50}$$

which measures the smoothness of the variables $\mathbf{V}$ in the stencil. The weights are determined as

$$\omega_0 = \frac{\alpha_0}{\alpha_0 + \alpha_1}, \omega_1 = \frac{\alpha_1}{\alpha_0 + \alpha_1}, \tilde{\omega}_0 = \frac{\tilde{\alpha}_0}{\tilde{\alpha}_0 + \tilde{\alpha}_1}, \tilde{\omega}_1 = \frac{\tilde{\alpha}_1}{\tilde{\alpha}_0 + \tilde{\alpha}_1}, \tag{3.51}$$

where $\alpha_r = \dfrac{d_r}{\epsilon + \beta_r}$, $\tilde{\alpha}_r = \dfrac{\tilde{d}_r}{\epsilon + \beta_r}$ with ϵ being a small and positive number. The corresponding linear weights are $d_0 = \frac{2}{3}$, $d_1 = \frac{1}{3}$ and $\tilde{d}_0 = d_1$, $\tilde{d}_1 = d_0$. Finally, the third order WENO3 scheme is constructed by the combination of second order reconstructed values as below

$$\mathbf{V}^L_{i+\frac{1}{2}} = \sum_{r=0}^{\xi-1} \omega_r \mathbf{V}^{(r)}_{i+\frac{1}{2}}, \quad \mathbf{V}^R_{i-\frac{1}{2}} = \sum_{r=0}^{\xi-1} \tilde{\omega}_r \mathbf{V}^{(r)}_{i-\frac{1}{2}}. \tag{3.52}$$

WENO5

The fifth order ($\xi = 3$) WENO5 scheme is given by

$$\mathbf{V}^L_{i+\frac{1}{2}} = \sum_{r=0}^{2} \omega_r \mathbf{V}^{(r)}_{i+\frac{1}{2}}, \quad \mathbf{V}^R_{i-\frac{1}{2}} = \sum_{r=0}^{2} \tilde{\omega}_r \mathbf{V}^{(r)}_{i-\frac{1}{2}}, \tag{3.53}$$

with six third order fluxes $\mathbf{V}^{(r)}_{i+\frac{1}{2}}$ and $\mathbf{V}^{(r)}_{i-\frac{1}{2}}$ based on different stencils as below

$$\left.\begin{aligned}
\mathbf{V}^{(0)}_{i+\frac{1}{2}} &= \tfrac{1}{3}\mathbf{V}_i + \tfrac{5}{6}\mathbf{V}_{i+1} - \tfrac{1}{6}\mathbf{V}_{i+2}, \quad & \mathbf{V}^{(0)}_{i-\frac{1}{2}} &= \tfrac{11}{6}\mathbf{V}_i - \tfrac{7}{6}\mathbf{V}_{i+1} + \tfrac{1}{3}\mathbf{V}_{i+2}, \\
\mathbf{V}^{(1)}_{i+\frac{1}{2}} &= -\tfrac{1}{6}\mathbf{V}_{i-1} + \tfrac{5}{6}\mathbf{V}_i + \tfrac{1}{3}\mathbf{V}_{i+1}, \quad & \mathbf{V}^{(1)}_{i-\frac{1}{2}} &= \tfrac{1}{3}\mathbf{V}_{i-1} + \tfrac{5}{6}\mathbf{V}_i - \tfrac{1}{6}\mathbf{V}_{i+1}, \\
\mathbf{V}^{(2)}_{i+\frac{1}{2}} &= \tfrac{1}{3}\mathbf{V}_{i-2} - \tfrac{7}{6}\mathbf{V}_{i-1} + \tfrac{11}{6}\mathbf{V}_i, \quad & \mathbf{V}^{(2)}_{i-\frac{1}{2}} &= -\tfrac{1}{6}\mathbf{V}_{i-2} + \tfrac{5}{6}\mathbf{V}_{i-1} + \tfrac{1}{3}\mathbf{V}_i.
\end{aligned}\right\} \tag{3.54}$$

The smoothness parameters are defined as

$$\left.\begin{aligned}
\beta_0 &= \tfrac{13}{12}(\mathbf{V}_i - 2\mathbf{V}_{i+1} + \mathbf{V}_{i+2})^2 + \tfrac{1}{4}(3\mathbf{V}_i - 4\mathbf{V}_{i+1} + \mathbf{V}_{i+2})^2, \\
\beta_1 &= \tfrac{13}{12}(\mathbf{V}_{i-1} - 2\mathbf{V}_i + \mathbf{V}_{i+1})^2 + \tfrac{1}{4}(\mathbf{V}_{i-1} - \mathbf{V}_{i+1})^2, \\
\beta_2 &= \tfrac{13}{12}(\mathbf{V}_{i-2} - 2\mathbf{V}_{i-1} + \mathbf{V}_i)^2 + \tfrac{1}{4}(\mathbf{V}_{i-2} - 4\mathbf{V}_{i-1} + 3\mathbf{V}_i)^2,
\end{aligned}\right\} \tag{3.55}$$

as well as the other parameters defined as $d_0 = \frac{3}{10}$, $d_1 = \frac{3}{5}$, $d_2 = \frac{1}{10}$ and the relations $\tilde{d}_0 = d_2$, $\tilde{d}_1 = d_1$, $\tilde{d}_2 = d_0$, along with the weights

$$\left.\begin{aligned}
\omega_0 &= \frac{\alpha_0}{\alpha_0 + \alpha_1 + \alpha_2}, \quad \omega_1 = \frac{\alpha_1}{\alpha_0 + \alpha_1 + \alpha_2}, \quad \omega_2 = \frac{\alpha_2}{\alpha_0 + \alpha_1 + \alpha_2}, \\
\tilde{\omega}_0 &= \frac{\tilde{\alpha}_0}{\tilde{\alpha}_0 + \tilde{\alpha}_1 + \tilde{\alpha}_2}, \quad \tilde{\omega}_1 = \frac{\tilde{\alpha}_1}{\tilde{\alpha}_0 + \tilde{\alpha}_1 + \tilde{\alpha}_2}, \quad \tilde{\omega}_2 = \frac{\tilde{\alpha}_2}{\tilde{\alpha}_0 + \tilde{\alpha}_1 + \tilde{\alpha}_2}.
\end{aligned}\right\} \tag{3.56}$$

As the discretisation should keep well balanced and preserve the upwind nature, Dutykh et al. (2011) suggested the source terms to be

$$\frac{1}{\Delta x}\int_{C_i}\mathbb{S}(\mathbf{V})dx \approx \frac{\mathbb{S}_{i-\frac{1}{2}}+\mathbb{S}_{i+\frac{1}{2}}}{2}, \quad \mathbb{S}_{i\pm\frac{1}{2}} = \mathbb{S}\left(\frac{V^L_{i\pm\frac{1}{2}}+V^R_{i\pm\frac{1}{2}}}{2}\right). \tag{3.57}$$

For the right-hand side, the second component of the dispersive terms $\mathbb{M}(\mathbf{V})$ are discretised by finite difference scheme:

$$\begin{aligned}\mathbf{M}_i(\bar{\mathbf{V}}) =& \frac{1}{2}\bar{h}_i\frac{\bar{h}_{i+1}(\bar{u}_t)_{i+1}-2\bar{h}_i(\bar{u}_t)_i+\bar{h}_{i-1}(\bar{u}_t)_{i-1}}{\Delta x^2}\\ &-\frac{1}{6}\bar{h}_i^2\frac{(\bar{u}_t)_{i+1}-2(\bar{u}_t)_i+(\bar{u}_t)_{i-1}}{\Delta x^2}\\ =&\frac{\bar{h}_i}{2\Delta x^2}(\bar{h}_{i-1}-\frac{1}{3}\bar{h}_i)(\bar{u}_t)_{i-1}\\ &-\frac{2}{3\Delta x^2}\bar{h}_i^2(\bar{u}_t)_i+\frac{\bar{h}_i}{2\Delta x^2}(\bar{h}_{i+1}-\frac{1}{3}\bar{h}_i)(\bar{u}_t)_{i+1},\end{aligned} \tag{3.58}$$

which is of the second order accuracy.

The semi-discrete scheme for Boussinesq equations (Dutykh and Kalisch, 2013) can be rewritten as

$$\left.\begin{aligned}&\frac{d\bar{H}}{dt}+\frac{1}{\Delta x}\left[\mathbb{F}^{(1)}_+(\bar{\mathbf{V}})-\mathbb{F}^{(1)}_-(\bar{\mathbf{V}})\right]=0,\\ &(I-M)\cdot\frac{d\bar{u}}{dt}+\frac{1}{\Delta x}\left[\mathbb{F}^{(2)}_+(\bar{\mathbf{V}})-\mathbb{F}^{(2)}_-(\bar{\mathbf{V}})\right]=\mathbb{S}^{(2)},\end{aligned}\right\} \tag{3.59}$$

where I is the identity matrix, $\mathbb{F}^{(1,2)}_\pm(\bar{\mathbf{V}})$ are the right (+) and left (-) components of the flux vector $\mathbb{F}$, respectively, $\mathbb{S}^{(2)}$ is the second component of the source term vector $\mathbb{S}$ and M is the diagonal matrix obtained by factoring out $\bar{u}_t$ of the $\mathbf{M}$ as discretised in (3.58).

Owing to the solid wall on each end, respectively, the boundary conditions are determined as totally reflective. By introducing the ghost cells, the solid wall is located at the boundary between the first ghost cell (index of 0) and first real cell (index of 1). Hence, the horizontal velocity at the wall is imposed to be zero by $(u)_{\frac{1}{2}}=0$. According to the finite volume discretisation, the imposed boundary

conditions are described

$$\left.\begin{aligned} H_0 &= H_1, \\ (u)_0 &= -(u)_1, \\ (u)_{\frac{1}{2}} &= 0, \end{aligned}\right\} \tag{3.60}$$

then, a fully reflective boundary is built.

Time discretisation used here is based on a Runge-Kutta scheme of the third order with four stages (Bogacki-Shampine method) proposed by Bogacki and Shampine (1989):

$$\begin{aligned} q_1 &= \mathcal{N}(\mathbf{V}^n, t_n), \\ q_2 &= \mathcal{N}(\mathbf{V}^n + \tfrac{1}{2}\Delta t q_1, t_n + \tfrac{1}{2}\Delta t), \\ q_3 &= \mathcal{N}(\mathbf{V}^n + \tfrac{3}{4}\Delta t q_2, t_n + \tfrac{3}{4}\Delta t), \\ \mathbf{V}^{n+1} &= \mathbf{V}^n + \Delta t(\tfrac{2}{9}q_1 + \tfrac{1}{3}q_2 + \tfrac{4}{9}q_3)\,. \end{aligned} \tag{3.61}$$

where $\mathbf{V}_t = \mathcal{N}(\mathbf{V}, t)$. Here, constant Δt is used as it already satisfies the required accuracy and saves computing time.

The computational domain was discretised with $\Delta x = 1/3$ and $\Delta t = 0.1$ non-dimensionally for computational efficiency and stability. The Courant-Friedrichs-Lewy (CFL) condition, which demonstrates the variables cannot run faster and skip any cell in a single time step, has been verified and satisfied with this discretisation. For the equation system (3.42), the propagation speed is determined by the eigenvalues of the flux Jacobian matrix, where the flux Jacobian matrix is given by

$$\frac{\partial \mathbb{F}(\mathbf{V})}{\partial \mathbf{V}} = \begin{pmatrix} u & H \\ g & u \end{pmatrix} \tag{3.62}$$

and it leads to two eigenvalues defined as:

$$\lambda^{\pm} = u \pm c_s, \quad c_s \equiv \sqrt{gH}. \tag{3.63}$$

Therefore, the propagation speed λ cannot exceed the cell speed $\dfrac{dx}{dt}$, which can

be used to define the Courant number as shown below:

$$C_r = \frac{dt}{dx}\max(|\lambda|) \tag{3.64}$$

and to ensure $C_r < 1$ all the time to satisfy the CFL condition. In fact, by using this discretisation, C_r is less than 0.5 at each time step.

In the case where dispersive term $\mathbb{M}(\mathbf{V})$ could be neglected, (3.42) reduces to NSW equations and are discretised in the form

$$\frac{d\bar{\mathbf{V}}_i}{dt} + \frac{1}{\Delta x}[\mathbb{F}(\mathbf{V}(x_{i+\frac{1}{2}})) - \mathbb{F}(\mathbf{V}(x_{i-\frac{1}{2}}))] = \frac{1}{\Delta x}\int_{C_i} \mathbf{S}(\mathbf{V})dx \equiv \bar{\mathbb{S}}_i. \tag{3.65}$$

The equations are solved by the same finite volume method for the Boussinesq equation system. Satisfying the CFL condition has been ensured for this scenario as well. Later in section 5.1.2, this system will be used to compare with the Boussinesq equation system for wave generation in a tank without beach. Moreover, NSW equations will also be used for wave run-up modelling where nonlinearity plays a key role and the dispersion can be neglected. The Boussinesq equation system becomes less suitable and convenient as additional terms should be added for breaking and the breaking point requires to be identified. The convenient way will be simply applying the NSW equations. Note that when the numerical models are applied in this study, the computational domain is the same long as the wave tank, if not otherwise specified.

It is noted that the WENO5 scheme is used for nonlinear shallow water system as it has higher accuracy. WENO schemes take longer time, but the neglect of the dispersion term saves time for the calculation. For Boussinesq equations, all three reconstruction schemes (UNO2, WENO3 and WENO5) are used and compared to one another, which is further discussed in subsection 3.3.1, in terms of the error and the goodness of the fitting.

3.2 Theories for wave run-up

For sloping beach, the tank-long generated wave will soon run up the beach in this wave tank as shown in Fig. 3.3, which depicts the topography of the problem consisting of a plane sloping beach connected to a moving bottom which causes bottom disturbance. Similarly, the horizontal x axis is positive onshore, with h_0 is the initial water depth in the offshore. The initial shoreline position (the still water level on the beach) is located at $x = 0$ on the plane beach with the slope γ. Meanwhile, the right tank end is positioned at $x = -\Gamma$ as Γ denotes the length of the initial length of the computational domain.

Owing to the complicated flow motion during wave run-up, in particular wave breaking, it is difficult to model wave run-up process practically. The analytical solutions derived by Madsen and Schäffer (2010) can be used to estimate the shoreline movement and the maximum run-up height for non-breaking incident waves, which is described in the section 3.2.1. The section 3.2.2 introduces the numerical model able to model the wave behaviour during wave run-up involving wave breaking based on the NSW equations solved by a high-order finite volume method with WENO schemes.

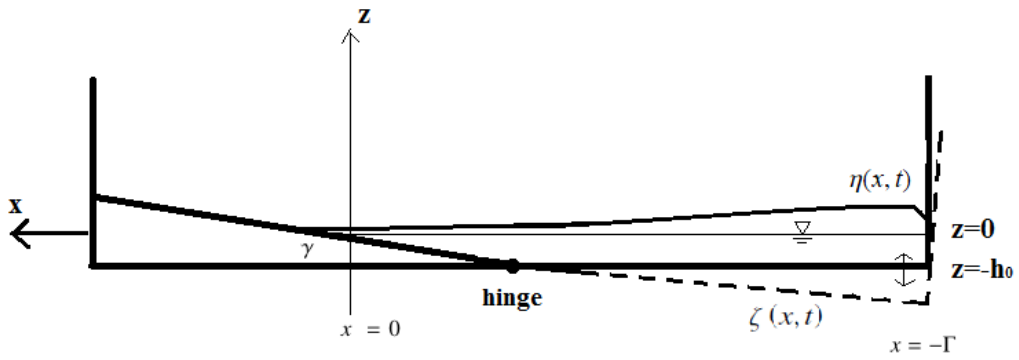

Figure 3.3: Coordinate system used for run-up modelling

3.2.1 Analytical solution to the NSW equations

Owing to the dominance of nonlinearity during wave run-up, the problem of wave run-up on a plane beach is describe by the NSW equations (2.6). Carrier and Greenspan (1958) solved the NSW equations based on the hodograph technique which transforms the coordinates of Eq. (2.6) from (x, t) to (ϱ, φ) which are the Riemann invariants. Then, new independent variables with the relation

$$\psi \equiv -\frac{1}{2g\gamma}(\varrho + \varphi),\ \rho \equiv \frac{1}{2g\gamma}(\varrho - \varphi) \tag{3.66}$$

are introduced by Madsen and Schäffer (2010). Then, the NSW equations are reduced to a single linear differential equation in terms of the velocity potential Φ

$$\frac{\partial^2 \Phi}{\partial \rho^2} + \frac{1}{\rho}\frac{\partial \Phi}{\partial \rho} - \frac{\partial^2 \Phi}{\partial \psi^2} = 0. \tag{3.67}$$

The solutions of η, u, x and t are obtained as below

$$\left.\begin{aligned} u(\rho,\psi) &= -\frac{1}{\rho}\frac{\partial \Phi}{\partial \rho}, \quad \eta(\rho,\psi) = -\left(\frac{\gamma}{2}\frac{\partial \Phi}{\partial \psi} + \frac{u^2}{2g}\right) \\ t(\rho,\psi) &= \psi + \frac{u}{g\gamma},\ x(\rho,\psi) = -\left(\frac{1}{2}\frac{\partial \Phi}{\partial \psi} + \frac{u^2}{2g\gamma} + \frac{g\gamma\rho^2}{4}\right) \end{aligned}\right\} \tag{3.68}$$

where u and x are opposite to Madsen and Schäffer (2010)'s as the x axis is in the opposite direction here. To identify the waves as non-breaking or breaking, Madsen and Schäffer (2010) proposed the breaking criterion

$$\frac{1}{g\gamma}\frac{\partial u}{\partial \psi} \to -1,\ \rho \to 0, \tag{3.69}$$

as $\rho \to 0$ indicates the shoreline location.

Madsen and Schäffer (2010) noted that the wave information at the beach foot is used as the incident wave where it is far away from the shoreline with small slope and the nonlinearity can be ignored. Here, the linear solution (3.37) at the foot location in a tank with infinite long propagation distance (unbounded domain) but without beach is used as η_i. With the incident wave η_i, the solutions

of the shoreline velocity U_s and the run-up height R are given by

$$U_s(\psi) = \frac{1}{\gamma}\int_{2t_0}^{\psi} Z(s)\, F_u(\psi - s)ds,\; F_u(t) \equiv \frac{\partial^2 \eta_i}{\partial t^2} \tag{3.70}$$

$$R(\psi) = \int_{2t_0}^{\psi} Z(s)\, F_\eta(\psi - s)ds - \frac{U_s(\psi)^2}{2g},\; F_\eta(t) \equiv \frac{\partial \eta_i}{\partial t} \tag{3.71}$$

and

$$Z(\psi) = \begin{cases} 0, \psi \leq 2t_0, \\ 2\sqrt{t_0}(\psi - 2t_0)^{-1/2}, \psi > 2t_0, \end{cases}$$

with $t_0 > 0.4T$ and $t_0 = h_0/\gamma/\sqrt{gh_0}$. Note that ψ is linearised as $\psi = t$. Using the analytical solutions in terms of the convolution theorem provides a quick approximation.

3.2.2 Numerical modelling by WENO finite volume method

Large increase of the nonlinear effects can cause the wave break, which consumes a lot of energy and decreases the wave run-up height. Thus, modelling for breaking waves during wave run-up is crucially important. The NSW equations are still suitable to build the model since the nonlinear effects become more significant and the hyperbolic equation permits shocks as solutions. The one-dimensional NSW equations with a bottom friction term in the conservative form are given by

$$\left.\begin{aligned} &H_t + (Hu)_x = 0, \\ &(Hu)_t + (Hu^2 + \tfrac{1}{2}gH^2)_x = gHh_x - C_d u|u|, \end{aligned}\right\} \tag{3.72}$$

where C_d denotes the drag coefficient in the friction term $C_d u|u|$. The conservative form is beneficial to dealing with the discontinuous solutions. Moreover, breaking waves are modelled as propagating bores which are similar to shock waves in gas dynamics, and no additional breaking dissipative terms required.

However, because of the difficulties in treating the shoreline position during run-up and run-down on the beach, a computational domain mapping technique (e.g., Zhang, 1996; Li and Raichlen, 2002) is applied to the numerical scheme

by transforming the moving space domain into fixed space domain. The length of the initial computation domain is represented by Γ. Thus, it is defined that $x = -\Gamma$ is the seaward boundary and $x = 0$ is the initial shoreline as shown in Fig. 3.3. Hence, the real coordinates are described by the transformed coordinates as below

$$\left.\begin{aligned} x &= (1 + X/\Gamma)x^* + X, \\ t &= t^*, \end{aligned}\right\} \tag{3.73}$$

where $X(t)$ is the shoreline position function, x^* and t^* are the transformed coordinates for space and time marked by $*$, respectively. Note that only the space domain changes, but the time domain does not change. t^* just indicates the time variable in the new coordinate system. Under the transformation, the grid points of the new computation domain will always keep unchanged as the shoreline position $x = X(t)$ always corresponds to $x^* = 0$, and the another boundary $x = -\Gamma$ always corresponds to $x^* = -\Gamma$. In other words, the number of the grids keeps unchanged while the grid size changes. Then, Eq. (3.73) can lead to the following relations:

$$\left.\begin{aligned} \frac{\partial}{\partial t} &= \frac{\partial}{\partial t^*} - \frac{1 + x^*/\Gamma}{1 + X/\Gamma} U \frac{\partial}{\partial x^*}, \\ \frac{\partial}{\partial x} &= \frac{1}{1 + X/\Gamma} \frac{\partial}{\partial x^*}, \end{aligned}\right\} \tag{3.74}$$

where $U(t^*) = \dfrac{dX(t^*)}{dt^*}$ indicates the shoreline velocity.

Then, (3.72) should be modified in the new coordinate system (asterisks dropped from now on) as below:

$$\left.\begin{aligned} &H_t + (-c_1 UH + c_2 Hu)_x = -c_2 UH/\Gamma, \\ &(Hu)_t + \left(-c_1 UHu + c_2 Hu^2 + c_2 gH^2/2\right)_x = c_2 gHh_x - c_2 UHu/\Gamma - C_d u|u|, \end{aligned}\right\} \tag{3.75}$$

where $c_1(x,t) = \dfrac{1 + x/\Gamma}{1 + X(t)/\Gamma}$ and $c_2(t) = \dfrac{1}{1 + X(t)/\Gamma}$.

Similarly, the equations are rearranged as the form in (3.65) with the variables $\mathbf{V}$, the advective flux $\mathbb{F}(\mathbf{V})$ and the source term $\mathbb{S}$ determined by $\mathbf{V} = \begin{pmatrix} H \\ Hu \end{pmatrix}$,

$\mathbb{F}(\mathbf{V}) = \begin{pmatrix} -c_1 UH + c_2 uH \\ -c_1 UHu + c_2 Hu^2 + c_2 gH^2/2 \end{pmatrix}$, and $\mathbb{S} = \begin{pmatrix} -c_2 UH/\Gamma \\ c_2 gHh_x - c_2 UHu/\Gamma - C_d u|u| \end{pmatrix}$. In order to solve these equations, the shock-capturing finite volume method is used with the reconstruction of the conservative variables $\mathbf{V}$ by WENO5 scheme and the flux function $\mathbb{F}(\mathbf{V})$ by Lax-Friedrichs central method as shown below

$$\left.\begin{aligned} &\frac{d\bar{H}}{dt} + \frac{1}{\Delta x}\left[\mathbb{F}_+^{(1)}(\bar{\mathbf{V}}) - \mathbb{F}_-^{(1)}(\bar{\mathbf{V}})\right] = \mathbb{S}^{(1)}, \\ &\frac{d\bar{H}\bar{u}}{dt} + \frac{1}{\Delta x}\left[\mathbb{F}_+^{(2)}(\bar{\mathbf{V}}) - \mathbb{F}_-^{(2)}(\bar{\mathbf{V}})\right] = \mathbb{S}^{(2)}, \end{aligned}\right\} \tag{3.76}$$

where the overbar above variables denotes cell average, $(1, 2)$ denote the first or second component of the corresponding term and $(+, -)$ are the right- or left-going component. In addition, the same Runge-Kutta scheme (3.61) is used for time discretisation.

Ghost cells are used on the seaward boundary which is fully reflective in the way same to Eq. 3.60. For the shoreward boundary, the boundary elevation and velocity in the transformed computing domain can be defined based on the following relations of Lagrangian descriptions proposed by Zhang (1996):

$$\left.\begin{aligned} &h(X(t)) + \eta(X(t), t) = 0, \\ &\frac{dX(t)}{dt} = U(t), \\ &\frac{dU}{dt} = -g\eta_x. \end{aligned}\right\} \tag{3.77}$$

Then, according to Beam-Warming scheme and trapezoidal integration, the boundary velocity $U(t)$ and shoreline position $X(t)$ can be estimated by the following

schemes of second-order in space and time (Zhang, 1996):

$$\left.\begin{aligned} U_N^{n+1} &= U_N^n - \frac{g\Delta t}{2\Delta x}(3\eta_N^n - 4\eta_{N-1}^n + \eta_{N-2}^n) + \frac{g\Delta t^2}{2\Delta x^2}(\eta_N^n - 2\eta_{N-1}^n + \eta_{N-2}^n), \\ X_N^{n+1} &= X_N^n + \tfrac{1}{2}\Delta t(U_N^{n+1} + U_N^n), \end{aligned}\right\} \tag{3.78}$$

where N is the last grid index of the transformed computing domain, which indicates the shoreline position all the time. In addition, the two conservative variables on the shoreward boundary are $H(X(t),t) = h(X(t)) + \eta(X(t),t) = 0$ and $Hu(X(t),t) = H(X(t),t) \cdot U(X(t),t) = 0$.

Bottom friction terms are commonly used to make the numerical results more practical. In this study, a quadratic form $C_d u|u|$ is used in conservative form where C_d is a drag coefficient. C_d also can be defined by $gn^2H^{-1/3}$ where n denotes the Manning's roughness coefficient. It is clearly found from the definition that bottom friction will be very large in shallow water, hence it is not ignorable during run-up since the water depth decreases significantly. On the other hand, C_d can be determined as a constant by comparing the experimental data as did in the present study. The constant used in this thesis is of the order of $O(0.01)$.

3.3 Test cases and validations

3.3.1 Wave generation validation

Test of a solitary wave in constant-depth water is used to validate the finite volume scheme for Boussinesq equations by examining if the solitary wave will always keep its shape and peak height during its propagation. The solitary wave solution $\eta = A_s \operatorname{sech}^2[K_s(x - x_0)]$ at $t = 0$ is used as the initial condition, in which x_0 denotes the position of the initial wave crest. Also, $\mathbb{S} = \mathbf{0}$ is used for constant depth. Figure 3.4 displays the solitary waves solved by the finite volume scheme with UNO2, WENO3 and WENO5, respectively. Note that $t_n = \sqrt{(h_0/g)}$. The standard deviations of the three schemes are listed in Table 3.1. The three numerical methods all closely approximate the exact solution with great agreement.

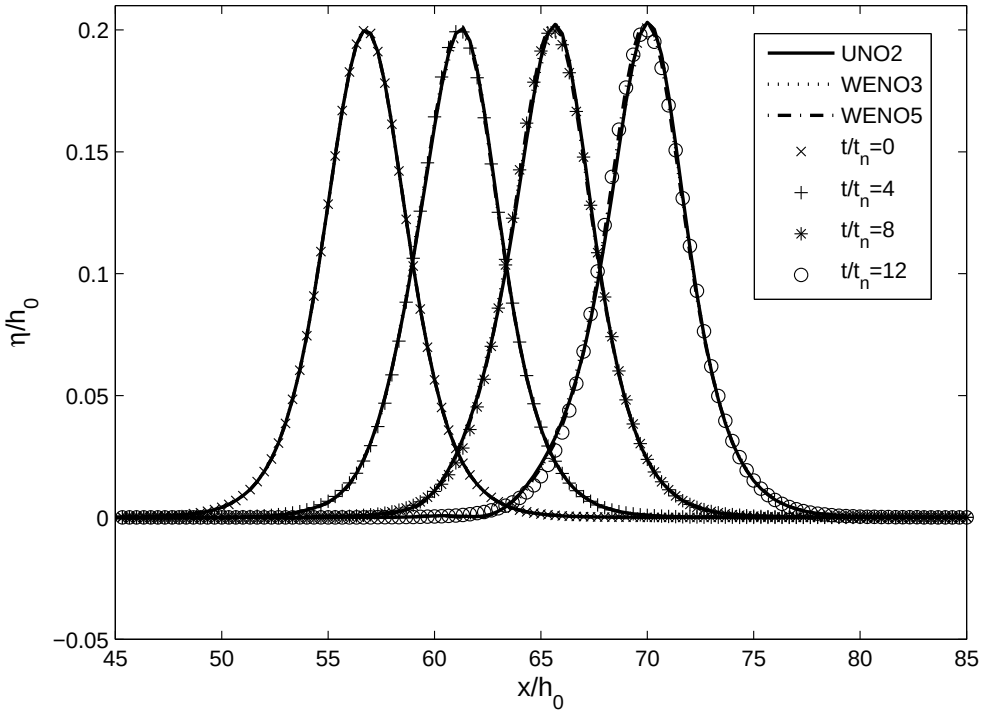

Figure 3.4: Comparisons of solitary wave among the three schemes (distinguished by line style) and the exact solution (markers) to the solitary wave with $A/h_0 = 0.2$.

Table 3.1: The standard deviation of the waves in Fig. 3.4 between the three schemes.

	UNO2	WENO3	WENO5
t/t_n=4	7.6769e-04	7.6523e-04	7.6452e-04
t/t_n=8	6.2907e-04	6.2377e-04	6.2237e-04
t/t_n=12	4.1264e-04	4.1121e-04	4.0689e-04

However, UNO2 reconstruction method is the least time-consuming with comparable accuracy to the other higher-order schemes. Comparably, WENO5 has the highest accuracy with the smallest standard deviation.

To investigate the conservation property of the numerical scheme, Figure 3.5 shows the time history of the total mass and energy denoted by V_s and E respectively with the following normalisation:

$$V_s' = \frac{V_s}{h_0^2}, \quad E' = \frac{E}{\rho g h_0^3}. \tag{3.79}$$

It is clearly seen that the mass and energy are conserved during the computation

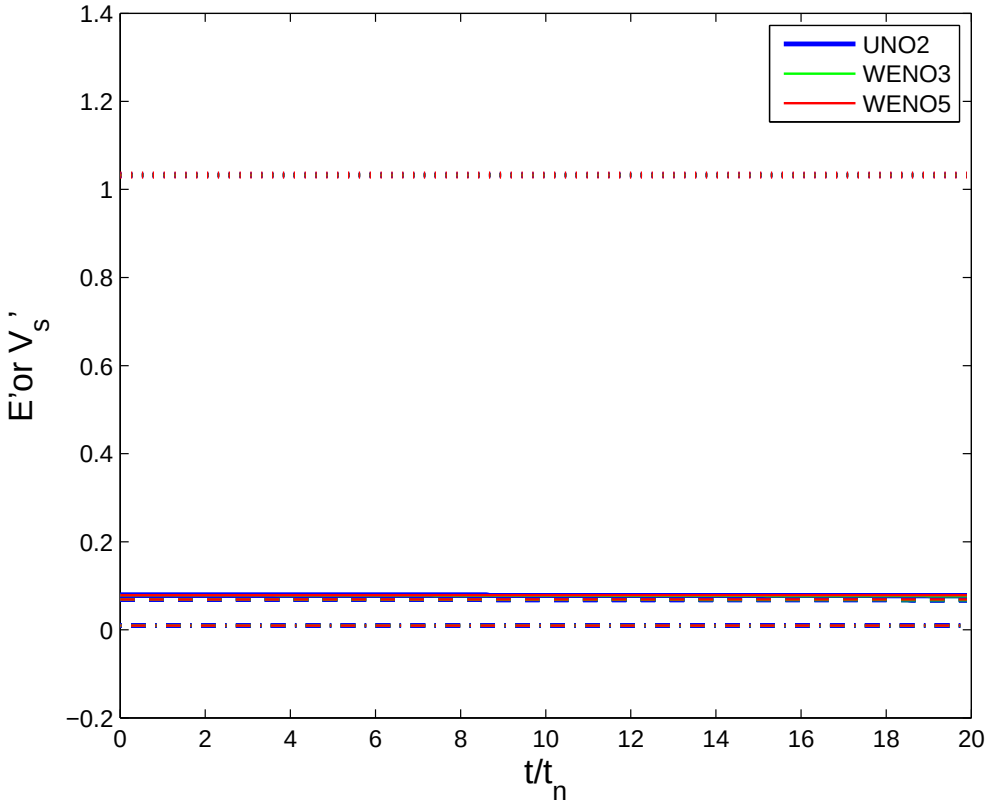

Figure 3.5: Comparisons of the conservation of mass and energy between the three schemes (dashed line, dash-dot, solid line and dotted line indicate potential energy, kinetic energy, total energy and volume, respectively, while the three schemes are distinguished by colour as marked).

for the three reconstruction methods. The conservation laws of the governing equations (3.41) have been ensured. Moreover, there is no wave breaking during the propagation as the energy dissipation cannot be found.

To maintain consistency in terms of accuracy, only UNO2 scheme is chosen to be used with the second order accurate scheme of the dispersive terms for solving Boussinesq equations, while WENO scheme is used for solving nonlinear shallow water system as no dispersive terms considered.

3.3.2 Inversion of bottom motion test cases

Given the time history of some wave elevation, the corresponding bottom motion by using the new wave maker can be obtained based on the convolution theorem in Eq. (3.40). After substituting the time-history of free surface elevation of a given solitary wave with amplitude 0.02 m and water depth 1.0 m as shown in Fig. 3.6 (b) into Eq. (3.40), the vertical velocity of the tilting bottom $W(0,t)$ is obtained by substituting the corresponding $Q(t)$ from Eq. (3.40) into the relation Eq. (3.29) with a=0.02 m in $D_0(x)$, which is shown in Fig. 3.6 (a) and compared to the horizontal velocity u of the solitary wave. The difference is caused by that the horizontal component of the bottom velocity is much smaller than the vertical component on gentle beach. The slight ripple at the beginning of $W(0,t)$ might be caused by the limitation and simplification of the linear wave theory. Thus, this method requires further improvement and verification. In the future study, the experiments of generating solitary waves, for example, by using the bottom motion in Fig. 3.6 (a), should be compared to the solitary wave solution as shown in Fig. 3.6 (b). Nevertheless, the test proves that in principle it is possible to absorb the unwanted reflected waves in this new wave tank by the convolution theorem Eq. (3.40).

3.3.3 Wave run-up test cases

The numerical scheme with WENO5 is used to solve the nonlinear shallow water system and estimate the wave run-up height. The method is verified here by numerically producing the Carrier-Greenspan exact solution of a time-periodic wave on a constant beach with amplitude $A/h_0 = 1$. The following non-dimensional variables are introduced in this test

$$x' = \frac{x}{h_0},\ t' = \frac{t}{\sqrt{h_0/g}},\ \eta' = \frac{\eta}{h_0},\ u' = \frac{u}{\sqrt{gh_0}},\ A' = \frac{A}{h_0} \tag{3.80}$$

while non-dimension indicator prime ($'$) has been dropped for convenience. Note that bottom friction is neglected here. When the initial time $t = 3\pi/4$ are defined,

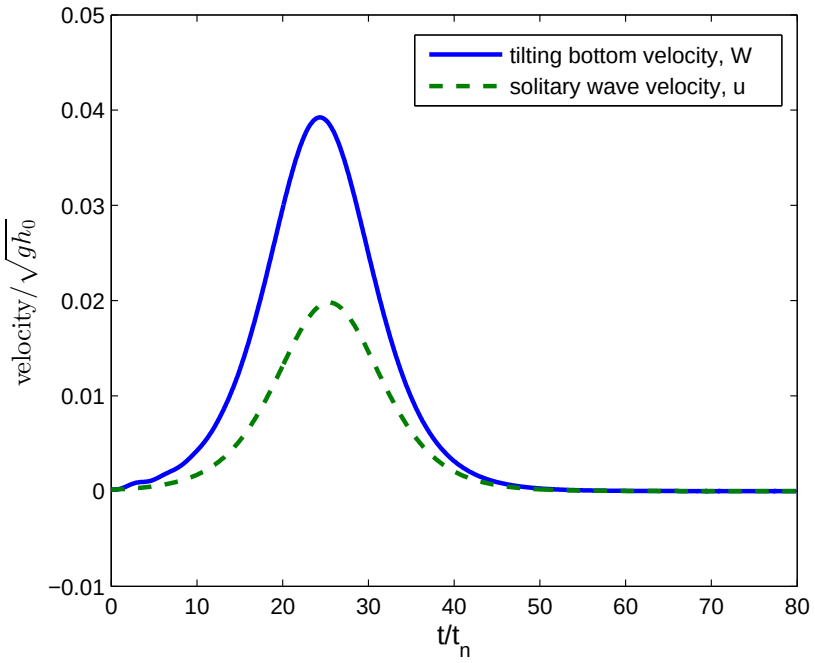

(a) The vertical bottom velocity $W(0,t)$ obtained by inversion calculation compared to horizontal solitary wave velocity

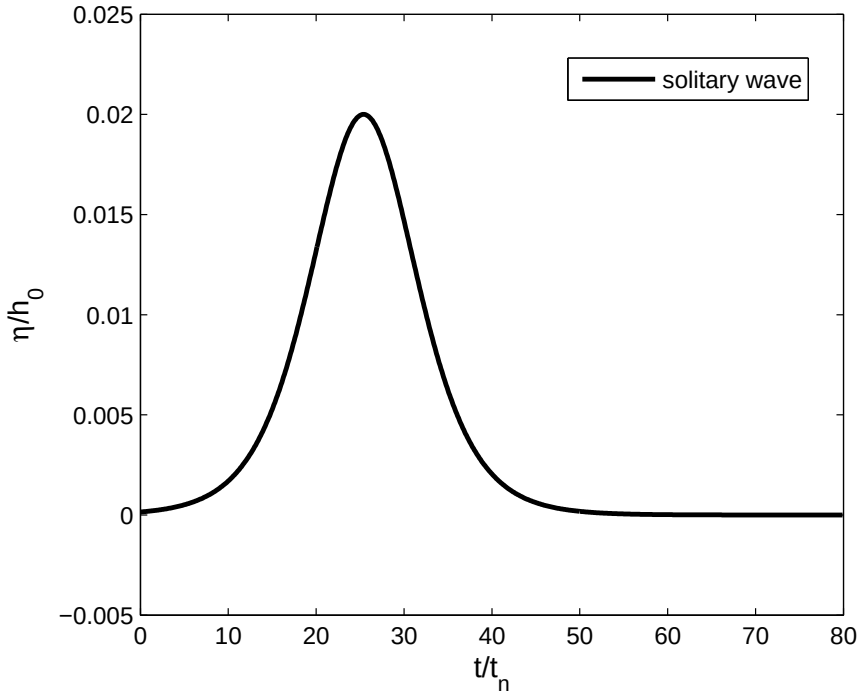

(b) The surface elevation time-history of the solitary wave

Figure 3.6: Test of inversion calculation of a solitary wave.

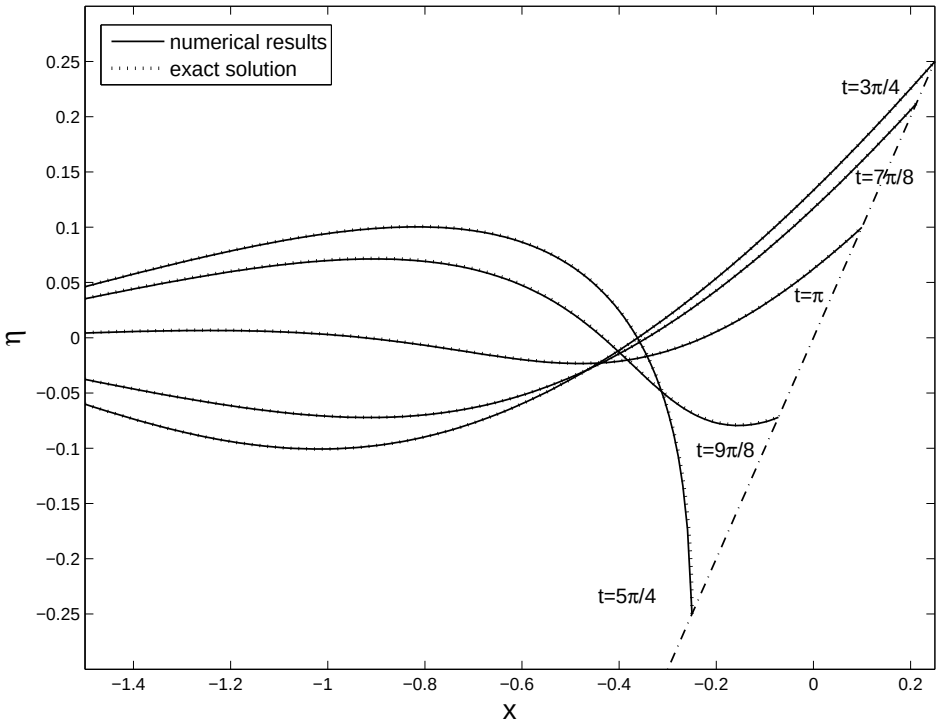

Figure 3.7: Comparison of the wave run-up model to Carrier-Greenspan periodic solution (solid line indicates the numerical results and dotted line indicates the exact solution).

the initial conditions can be obtained from the Carrier-Greenspan exact solution, which are

$$\left.\begin{aligned} \eta_0 &= J_0(\sigma)/4, \\ u_0 &= 0, \\ x &= -\sigma^2/16 + J_0(\sigma)/4, \end{aligned}\right\} \tag{3.81}$$

where σ is a new variable defined as $\sigma = 4\sqrt{-x+\eta_0}$. Given some x, the corresponding σ can be obtained by iteration with Newton-Raphson method and substituted into the first relation in (3.81) for the initial water elevation η_0. Besides, the seaward boundary is also determined from exact solution.

Figure 3.7 presents the comparison between the numerical results and the corresponding Carrier-Greenspan exact solutions. The wave runs down from the initial time $t = 3\pi/4$ and stops at $t = 5\pi/4$ with velocity $u = 0$ instantly. The comparison shows the scheme can closely approximate the Carrier-Greenspan ex-

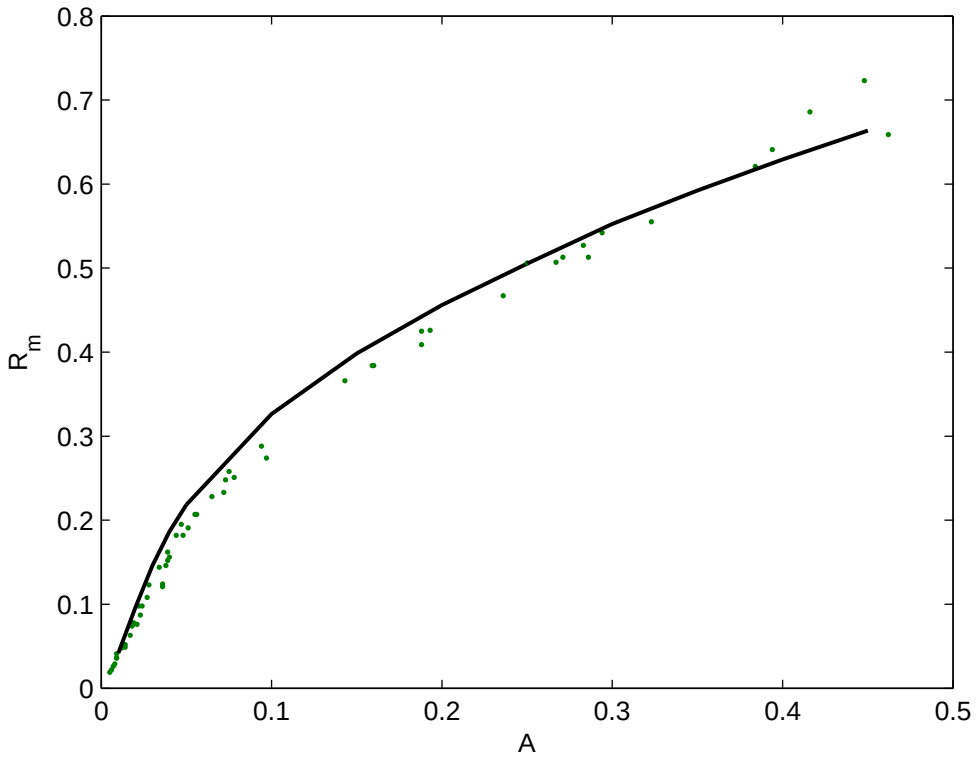

Figure 3.8: Comparison of R_m between the NSW numerical model (solid line) and the experimental data by Synolakis (1986)(dot).

act solution from the beginning, with the standard deviation less than 10^{-3}. This test sufficiently verifies the ability of this numerical model of solving nonlinear shallow water waves on plane beach.

Furthermore, the maximum run-up height R_m as a function of the incident wave height A from the NSW system is compared to the experimental data by Synolakis (1986) for the solitary waves on a slope of 1/19.85, which is shown in Fig. 3.8. The initial wave peak is located one half of the effective wavelength away from the beach foot. The dimensionless incident wave height A/h_o ranges from 0.01 to 0.45, resulting R_m/h_o up to 0.66, which approach to the experimental data in good agreement. It is noted that bottom friction term is included in this test for more practical simulation, where C_d is chosen 0.0015 which is one order of magnitude smaller than the values used for the new wave tank.

Chapter 4

Experimental equipment and procedures

In an effort to generate waves longer than the commonly used solitary-type long wave model (effective wavelength) in laboratory, a new wave maker has been designed. The new wave maker was constructed at the University of Dundee, Scotland. All the experiments were conducted in Fluids Laboratory at the University of Dundee, Scotland. In this chapter, the design and the equipments used are introduced first, followed by the methods and the instrumentation of measurement. Note that only half of the disturbance and fluid domain were considered due to the symmetry of the problem depicted in Figure 3.2.

4.1 Preliminary design

As mentioned earlier, Fig. 3.1 already depicts the main idea of the new wave maker with the associated coordinate system. The wave maker consists of a moving bottom hinged to a fixed bottom, so that the bottom will move in a rotational motion with the vertical displacement of the moving part $\zeta(x,t) \approx (L-x)\theta(t)$.

The purpose in this section is to demonstrate that the wave maker with the specific geometry is capable of generating waves longer than solitary waves in

terms of the effective wavelength. The preliminary design is based on the linear wave theory (3.37), where $Q(t)$ is defined as $Q(t) = 1/b$ within $0 < t < b$ for the simplest upward motion and $Q(t) = -1/b$ within $0 < t < b$ for the simplest downward motion with b denoting the motion duration time. Also it is noted in Eq. (5.7) and Eq. (5.8), as the analytical solution for downward motion is just opposite to that for upward motion, it is efficient to use only upward motion for design purpose. Both motions begin from the initial position where $\theta \neq 0$ and stop at $\theta = 0$ to ensure flat bottom throughout the wave tank for wave propagation, and slope is not considered here. Moreover, as it can be found that the wavelength increases with growing motion duration, the minimum and observable duration time (0.5 s) the actuator can provide is used to generate the shortest wave for the following cases discussed.

Accordingly, Fig. 4.1 shows the preliminary design of the two-dimensional wave tank. For discovering the limit of generating long waves by the wave maker,

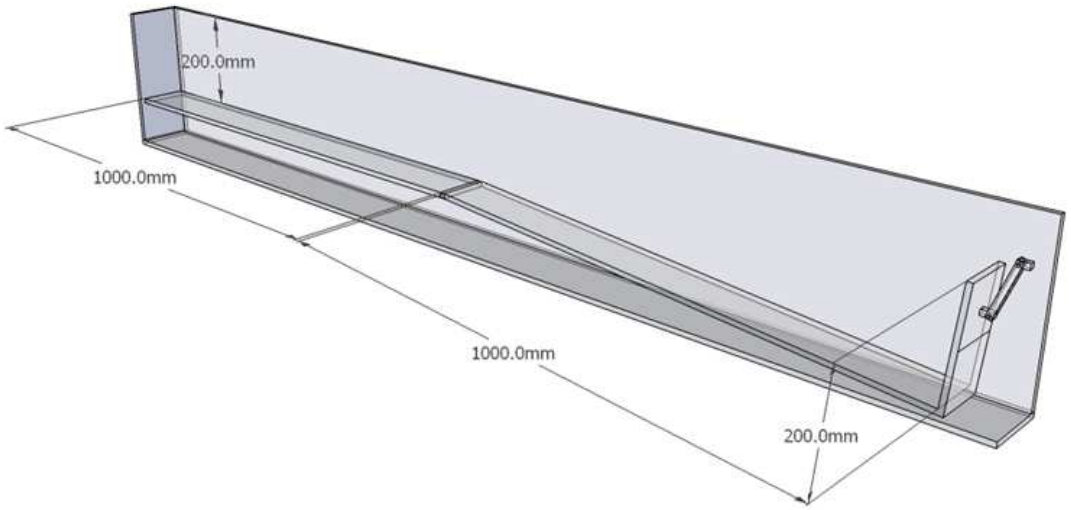

Figure 4.1: Schematic sketch of the design of the two-dimensional wave tank.

the water depth is of interest if the length of the moving bottom is fixed. Hence, a parameter $\alpha = h_0/L$ is introduced. Based on the typical relation of α up to $O(0.1)$ in laboratory for long wave generation, a range of water depth ratio α with different bottom motion amplitude a are calculated as shown in Fig. 4.2. Note that although the practical α of tsunamis will be much smaller, it would be

not meaningful in this size of wave tank by applying very small water depth.

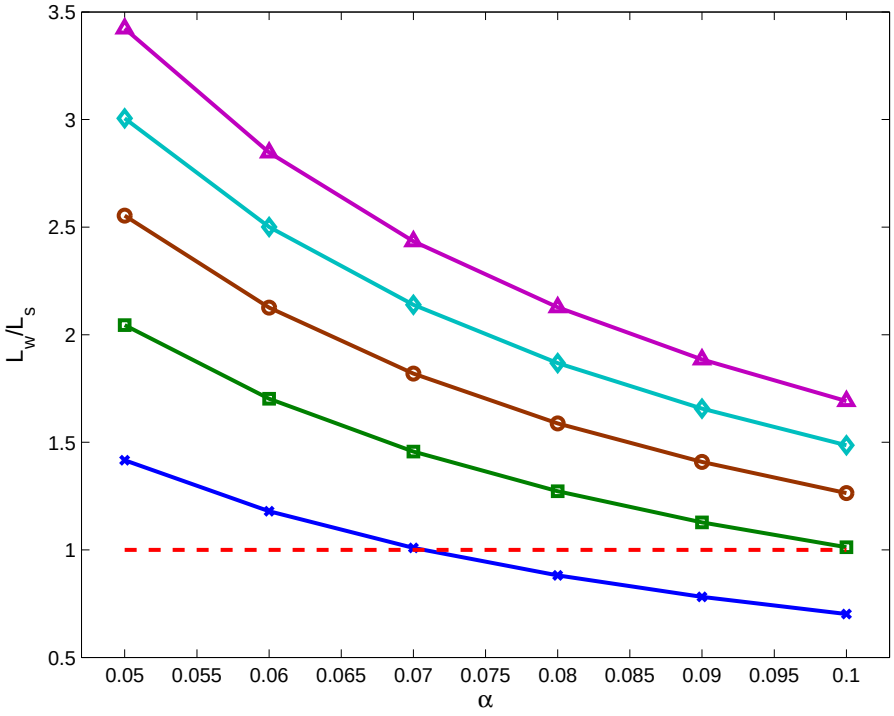

Figure 4.2: The ratios of the generated wavelength to the solitary wavelength, L_w/L_s, plotted against varying α and a: $---$, $L_w/L_s = 1$; $\times$, $a/h_0 = 0.1$; $\square$, $a/h_0 = 0.2$; $\circ$, $a/h_0 = 0.3$; $\diamond$, $a/h_0 = 0.4$; $\triangle$, $a/h_0 = 0.5$.

The analytical solution (3.37) was used to compare the ratio L_w/L_s indicating the ability of the wave maker of generating waves longer than the effective wavelengths of solitary waves. It is observed in Fig. 4.2 that L_w/L_s grows with decreasing α and with increasing a. For the smallest $a/h_0 = 0.1$ tested here, it is expected that the generated wave will be longer than the solitary wave for $\alpha < 0.07$ in terms of the effective wavelength.

4.2 Experimental equipment

The experimental equipment consists of a wave tank including a plane beach, a wave generation system, a water surface elevation measuring system based on

acoustic sensors and a video measuring system. The two states of the equipment set-up are shown in Fig. 4.3 (wave generation) and Fig. 4.4 (wave run-up), respectively. These components are described in detail as below.

4.2.1 Wave tank

A series of experiments were carried out in the wave tank shown in Fig. 4.3. The tank is 2.185 m long, 0.11 m wide and 0.3 m deep, which consists of an adjustable slope and the bottom-tilting wave maker. The sidewalls throughout the tank were made of clear acrylic sheets with thickness of 10 mm. The edges along the acrylic walls were sealed by silicone sealant to prevent leakage. In addition, a 2.3 m long and 0.41 m wide PVC membrane covered the inner surface of the wave tank to ensure waterproofness. The whole wave tank is supported by two steel legs, with a steel stand at the right end holding the actuator system. These steel components created the steel bottom structure for the wave tank. The bottom structure was levelled parallel to the ground.

However, the structure of the right leg is slightly more complicated as shown in the magnified detail in Fig. 4.3. A long and strong threaded rod jointed the tank bottom and the right leg vertically. The wheel on the rod was used to adjust the bottom height according to the desired beach slope. Turning the wheel clockwise (decreasing) or anticlockwise (increasing) can adjust the distance between the top of the right leg and its above tank bottom, which creates the height difference between the left and the right legs. Then, the beach with desired slope was created by a specific height difference, which is demonstrated in Fig. 4.4. The slope can reach up to 1:15, i.e., it can provide a range of gentle slopes for the beach. If the hight difference is zero, the fixed bottom is not regarded as a beach since it is parallel to the ground.

The beach (fixed bottom) is 1 m long and 0.11 m wide made of a 10 mm thick acrylic sheet. It was fixed to the tank walls by screws along the two sides, of which the edges were sealed. The water inlet and outlet were set at the left end

close to the beach. The water inlet supplies water directly into the area covered by the membrane. Water was dyed for colour contrast to the background of the tank wall. A valve installed on the fixed bottom just above the water outlet was used to control water drainage when necessary. Additionally, an air level with regard to three directions was used to ensure the parallel of the tank.

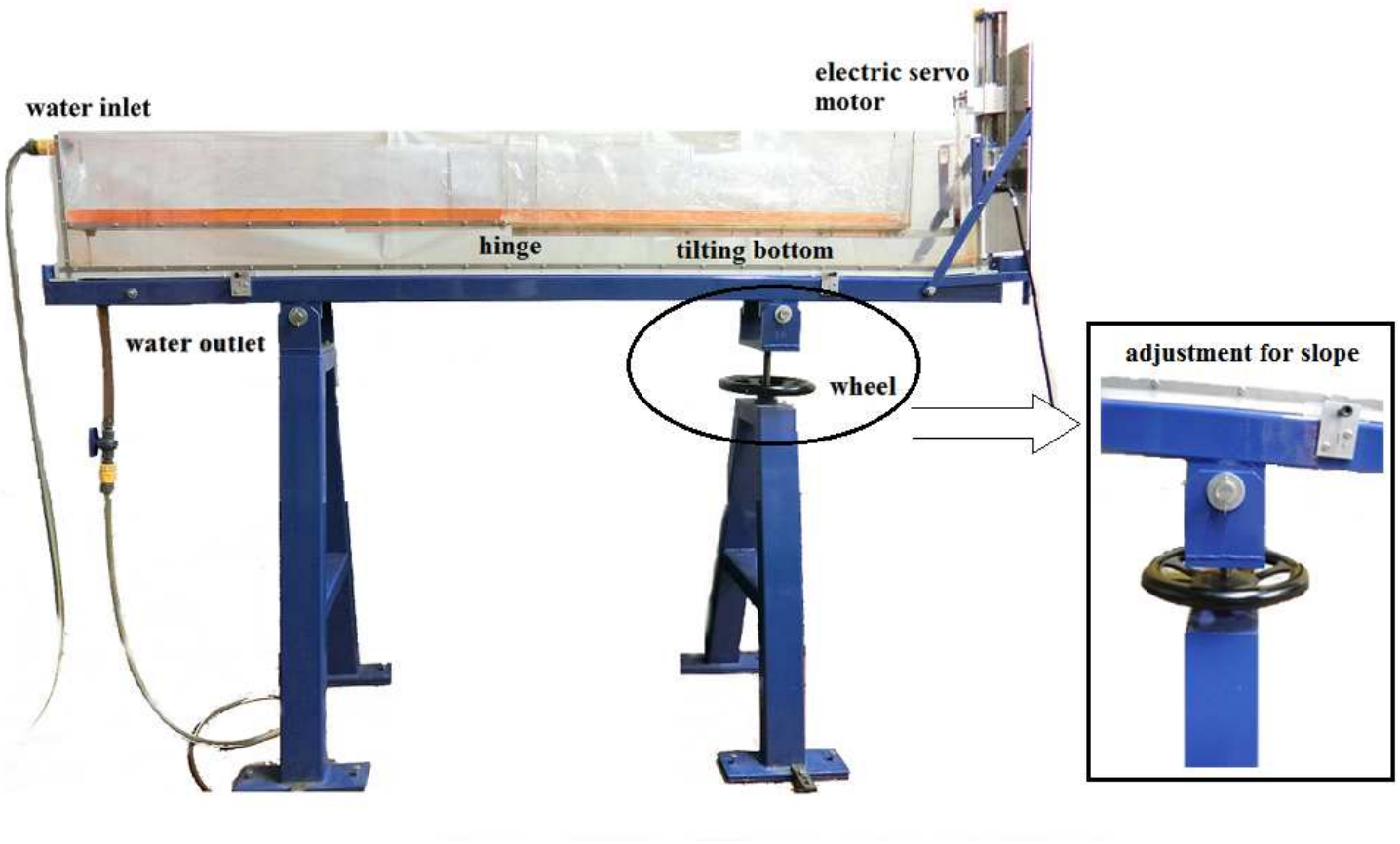

Figure 4.3: Photo of the wave tank with the bottom-tilting wave maker (components are shown as indicated).

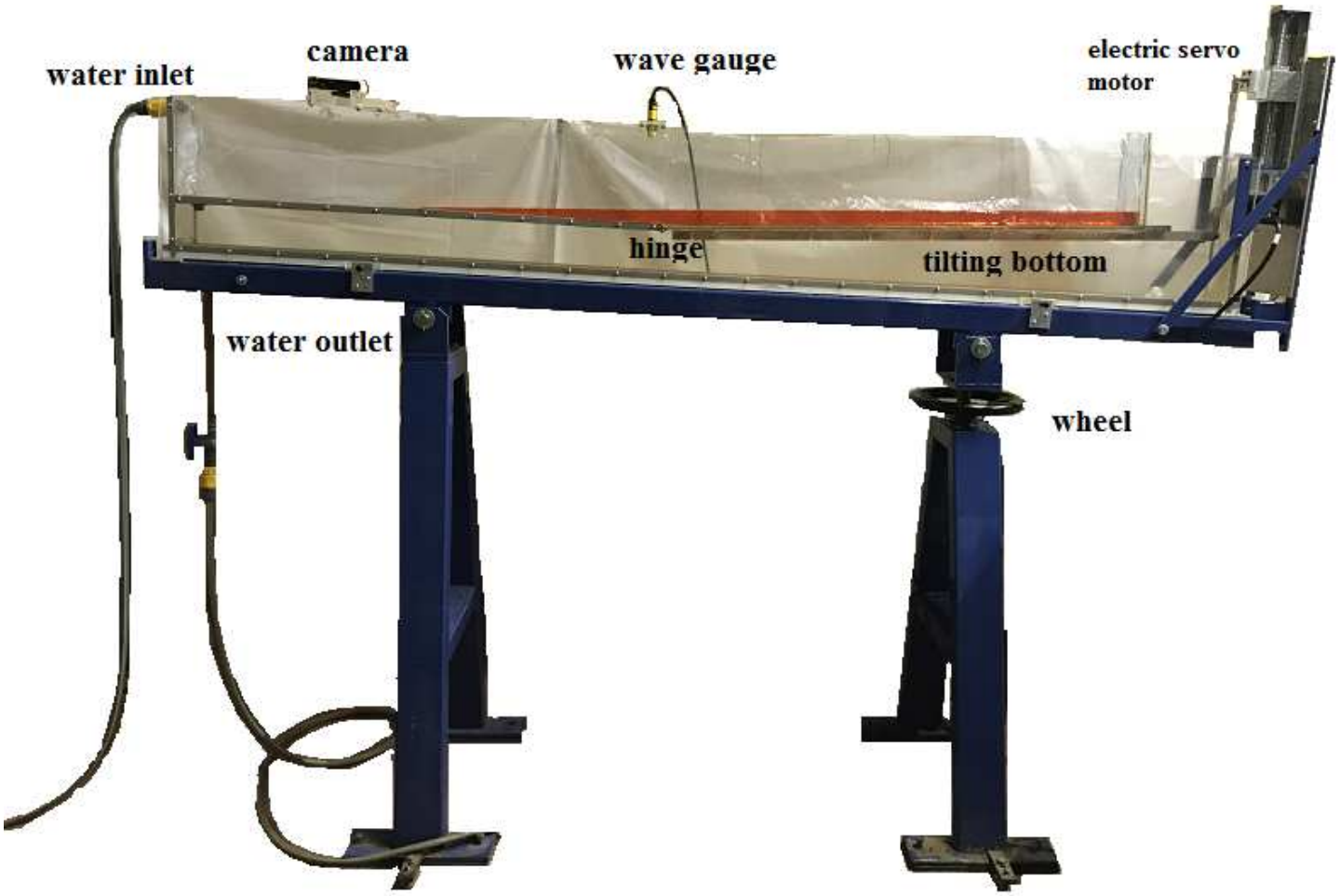

Figure 4.4: Photo of the experimental set-up for wave run-up investigation.

4.2.2 Wave generation system

The wave generation system was built based on an electrical servo control system, which becomes the core of the bottom-tilting wave maker. An actuator system, a steel connector and a moving bottom as shown in Fig. 4.5 constitute the wave generation system. Besides, the actuator system (①) consists of a block (②),

Figure 4.5: Photo of the generation system.

an electrical servo motor (③) and a track (④) sitting at the right end of the tank. The ANIMATICS® SM23165DT electrical-servo motor is located at the bottom of the track. The block is and aluminium block (60×60×40 mm^3) with several threaded holes on its surface. It can move along the track as it is driven by a threaded rod (⑤) through its body. The accuracy of the servo motor is

0.1/300 (mm/mm). The threaded rod was connected to the motor shaft (⑥) and the track top. The aluminium track (0.3 m) was fixed to the aluminium stand supported by two steel triangles (⑦). Thus, it limits the maximum motion displacement of 0.3 m. The power supplies the motor 48 Vdc through a switching regulator MeanWell® DRP-480S-48. The motor accepts many types of communication port. In the present study, through an adapter cable FTDI® US232R-100, the actuator was connected to a computer.

To operate the motor, the unique commands by a user programme were sent through Smart Motor Interface (SMI), which can be seen in Fig. 4.6. SMI can detect the appropriate serial port for users once the communication is built, e.g., the Com4 shown with motor 1 connected. The 'Configuration' window shows the serial port connected and the various ways of communication, e.g., RS-232, RS-485, and other industry standard control networks like ethernet, USB, CANopen and Modbus. Several hundreds of commands satisfy different programming requirements, which are directly sent through 'Terminal' window under the current serial port. A programme file is shown as an example at the right window. The bottom 'Information' window shows the programme status. SMI assists the users to not only control but also monitor the status of the motors.

The programme must have Target Acceleration-Deceleration (ADT), Target Velocity (VT) and Target Position (PT) set to execute the motion, followed by a Go (G) command, which can be found in the example programme in Fig. 4.6. In addition, there are also AT and DT commands for setting the acceleration and deceleration, respectively. The values to set are obtained by multiplying the desired acceleration (rev/sec^2) by 4.096 for ADT and multiplying the desired velocity (rev/sec) by 32768 for VT. Similarly, PT is set by multiplying the number of revolution of the threaded rod by 4000 (10 mm per revolution). As the initial velocity and acceleration are set zero in the present study, only the initial position needs to be adjusted before running the programme.

It is noted that the required speed cannot be obtained instantly as the motor usually accelerates up to the required speed and decelerates to a stop. Thus, for

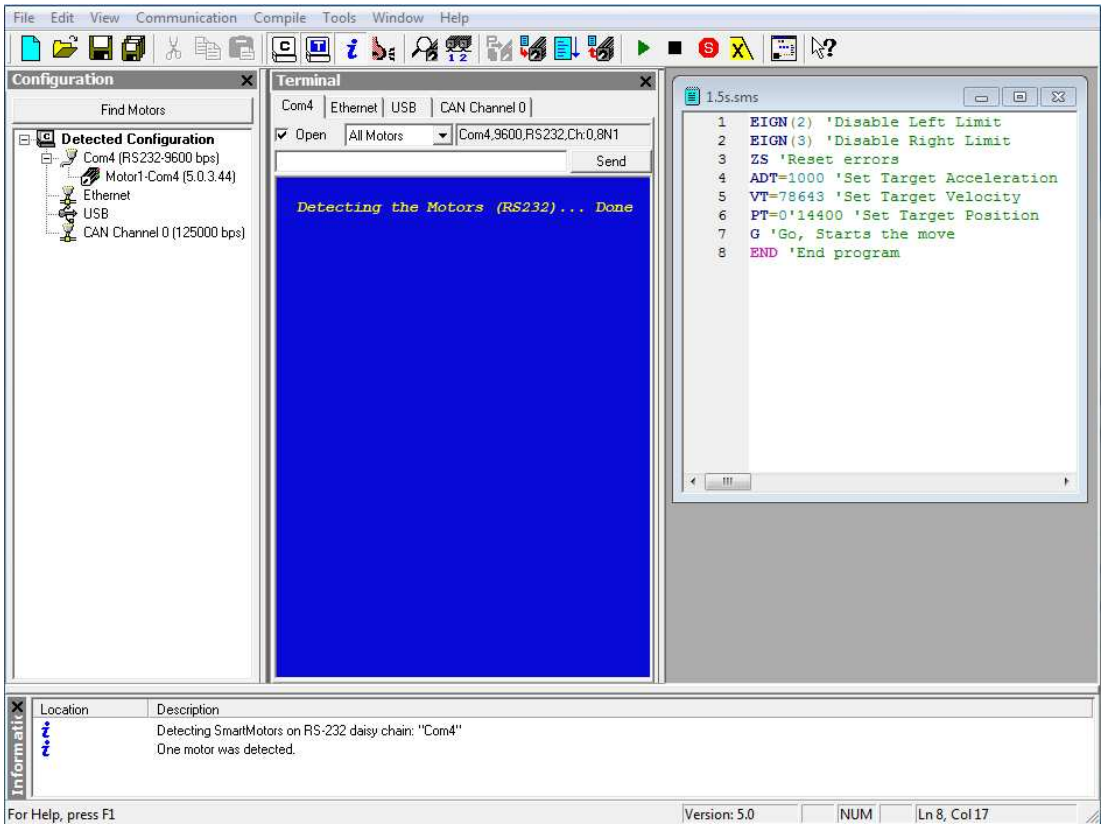

Figure 4.6: Snapshot of Smart Motor Interface (SMI) with an example programme.

a uniform motion, there will be a trapezoidal velocity profile, but not constant speed throughout the timeline. However, with great acceleration, the motions were assumed as uniform motion in the present study, e.g., the example velocity profile (upper curve) in Fig. 4.7. ADT has a typical value 100, but 1000 was normally used here. In addition, since 10 rev/sec is already very quick for the tank, it is defined as a velocity limit in this study. Due to the length of the track and the tank depth, PT could have a maximum value of 30*4000. Therefore, a wide range of motions can be created.

The servo motor has a controller, an amplifier and an encoder. After transmitting the programme to the motor, the controller will move the motor to follow a specified trajectory by controlling the power level. In detail, a PID (Proportional, Integral, Derivative) control section will direct the amplifier to deliver the current exactly that much as required to reach PT, with the frequency of 8000 Hz of updating the power level. The motor gives the moving bottom the expected

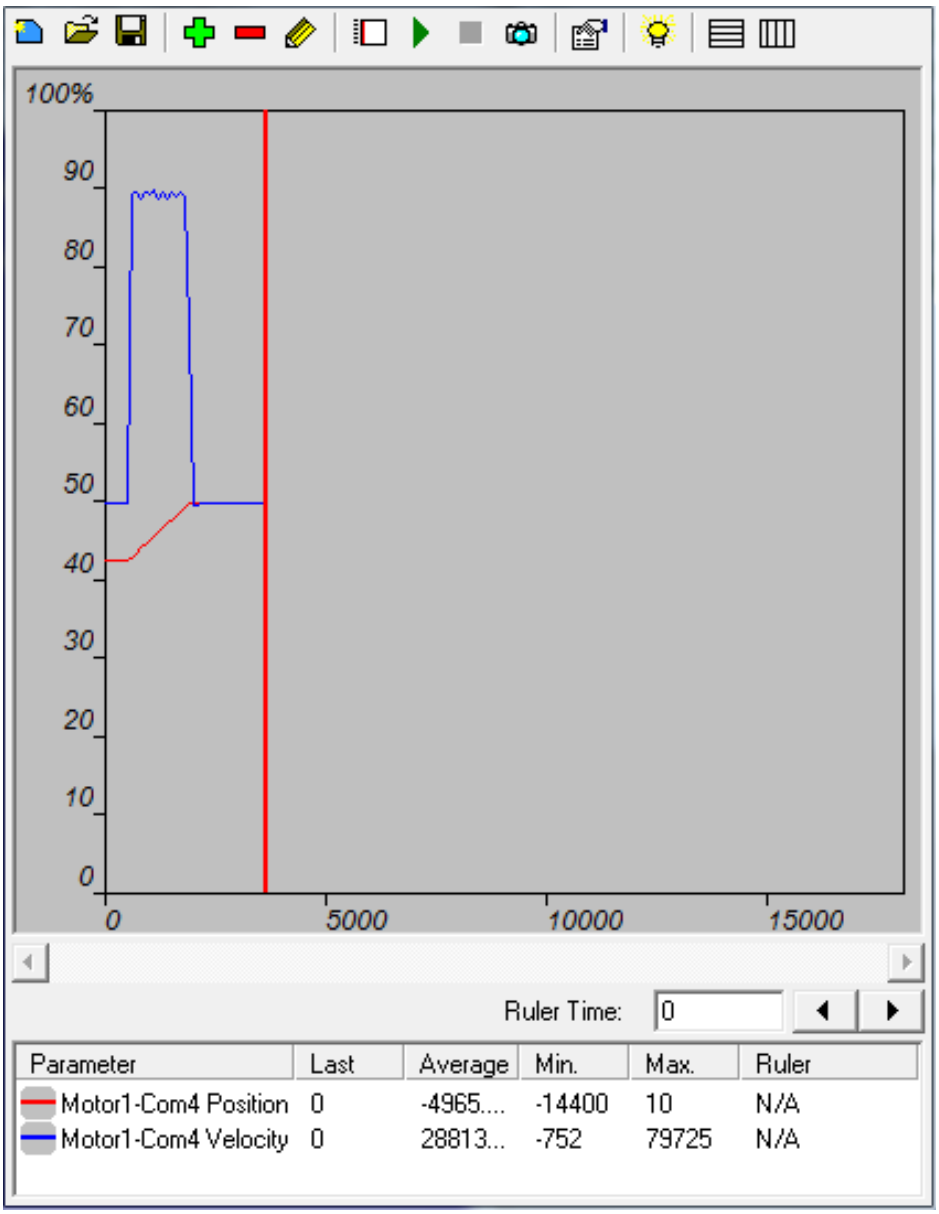

Figure 4.7: Snapshot of the chart-view for a motion described in Fig. 4.6.

vertical velocity and displacement directly through a steel connector attached to the back of the bottom.

The steel connector is a 1.2 m long straight steel support hinged to a 0.3 m long rod which connects the steel support and the actuator block. Through the steel connector, the moving bottom follows the actuator to move vertically. However, as the connector is longer than the length of the moving bottom, an amplification parameter 1.2 determined based on the geometrical relation should be applied for precisely driving the moving bottom. For example, the minimum

value of position -14400 in Fig. 4.7 is the initial position of the bottom (-30 mm), which is obtained by $3 * 4000 * 1.2$.

The moving bottom is a 1 m long and 0.11 m wide acrylic sheet hinged to the beach which has the same dimension. Rubber seals were attached around the edges of the moving bottom. The hinge is located at 0.2 m below the top of the tank, which leaves enough space for varying bottom motions (upward, downward or combination). After bottom motion, the moving bottom always keeps parallel to the ground for constant water depth.

To monitor and check the motion status, SMI provides the 'chartview' function as seen in Fig. 4.7. The upper curve indicates the motor velocity while the lower curve is the motor position. As the chart started earlier than the motor, there is a time lag at the beginning. It is noted that 50 % indicates the 0 position. The chart presents an example of an upward motion described in Fig. 4.6 by lifting the bottom from lower position -14400 to 0. The velocity shown in Fig. 4.7 presents a uniform motion, which also verifies that the acceleration $ADT = 1000$ is sufficiently big for the motor to arrive the desired velocity rapidly. The lowest window shows some summarised information of the actuator velocity and position. Accordingly, the maximum error here is 0.07% for motion position and 1.38% for motion velocity owing to the friction and the mechanical response. Thus, it has been verified that the motor is able to provide the bottom the expected velocity and position with high accuracy.

4.2.3 Ultra-sonic wave gauge

The time histories of free surface elevation are often measured by wave gauges, e.g., resistance type and capacitance type (Li, 2000). In the present study, acoustic sensors were used as wave gauges. A photo of the wave gauge BANNER® U-STAGE™S18UUA in straight housing is shown in Fig. 4.8. It is an ultrasonic sensor consisting of a 2 m long unterminated wire, status indicators, a TEACH mode button and a transducer packed in a 0.054 m long threaded cylinder with

two threaded rings for fixing itself. It is powered by 12-30V dc. The ultrasonic frequency is 300 kHz with the time resolution 30 ms.

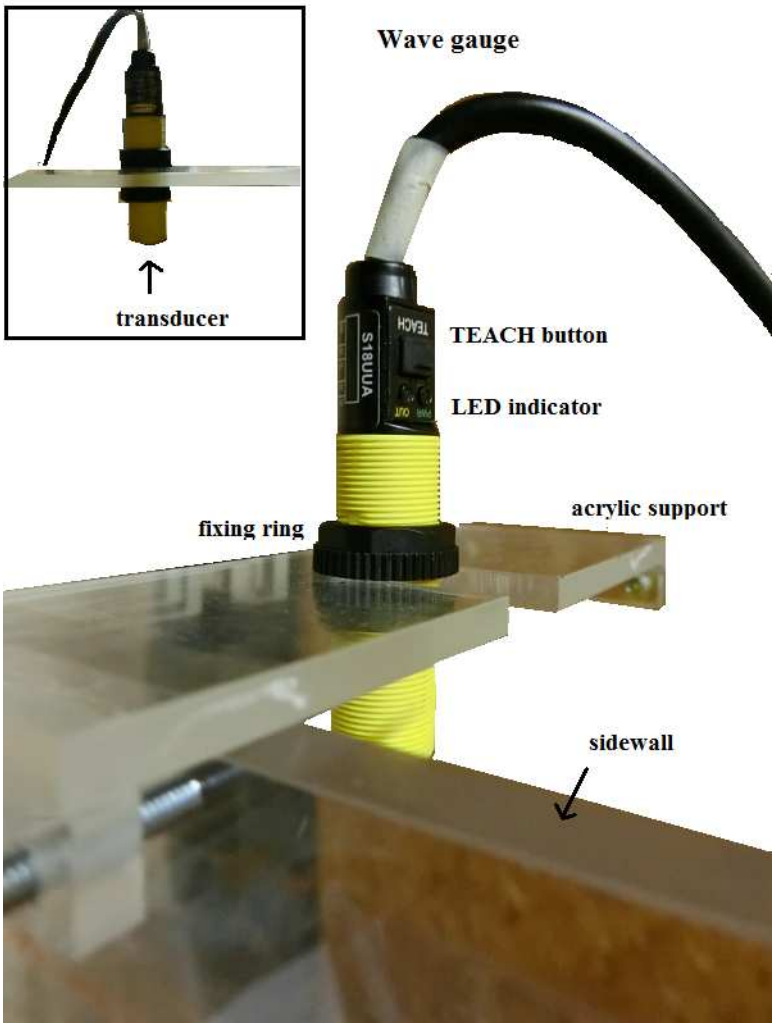

Figure 4.8: Photo of the ultrasonic sensor fixed above the tank.

The wave gauge provides two models for analog output: current-sourcing model and voltage-sourcing model. The voltage-sourcing model was chosen in the present study, which means that the analog output (0-10V) relies on the time-varying voltage proportional to the time history of the water surface displacement. The sensing distance is ranging from 0.03 m to 0.3 m. Thus, the wave gauge cannot be too close or too far to the water surface. Furthermore, the TEACH mode can be used to set individual minimum and maximum limits of a sensing area, which gives the wave gauge the limitation of how much should be located above the water free surface. According to the programmed sensing area, the output will be uniformly distributed along the length between the two setpoints.

The wave gauges were calibrated before the experiments in order to convert the electrical signal precisely, accompanying the tolerant error of the ultrasonic sensor as ±0.5 mm in the mode that the output response time was chosen 30 ms. In principle, the ultrasonic sensor measures the time of the ultrasonic pulse travelling to the object and returning back to the sensor (t_g) at the speed of sound (c_{sd}). Then, the distance from the sensor to the target (Ψ_g) is obtained by

$$\Psi_g = c_{sd} t_g / 2. \tag{4.1}$$

Then, in voltage-sourcing model, the measured distance is represented by voltage signals.

By measuring a ruler of a length of 250 mm at every 5 mm, Fig. 4.9 shows the calibration results with a linear fitting function. The linear function was fitted to the data well with a determined coefficient by averaging the coefficients from the several calibration tests. According to the fitting function, the time-history of free surface elevation can be obtained by the time history of the surface displacement calibrated from the voltage outputs and the initial water surface determined at the beginning.

4.2.4 Video equipment

A high-speed video camera has been used mainly for recording the shoreline movement during wave run-up (overhead recording) and also for verifying that the bottom movement is precisely executed following the programme by SMI (sideview recording). The two ways of recording are shown in the schematic drawings in Fig. 4.10. The video camera is CASIO® EXILIM EX-ZR3500, a high-speed digital camera manufactured by CASIO Computer Company, Limited. It consists of a 25 mm wide-angle lens, a tilt-type 3.0-inch LCD monitor screen and a control panel. The frames were stored in a SanDisk® Class 4 SDHC card with the capacity of 32 GB.

One of the highlights is its ExilimEngineHS3 technology for high-speed oper-

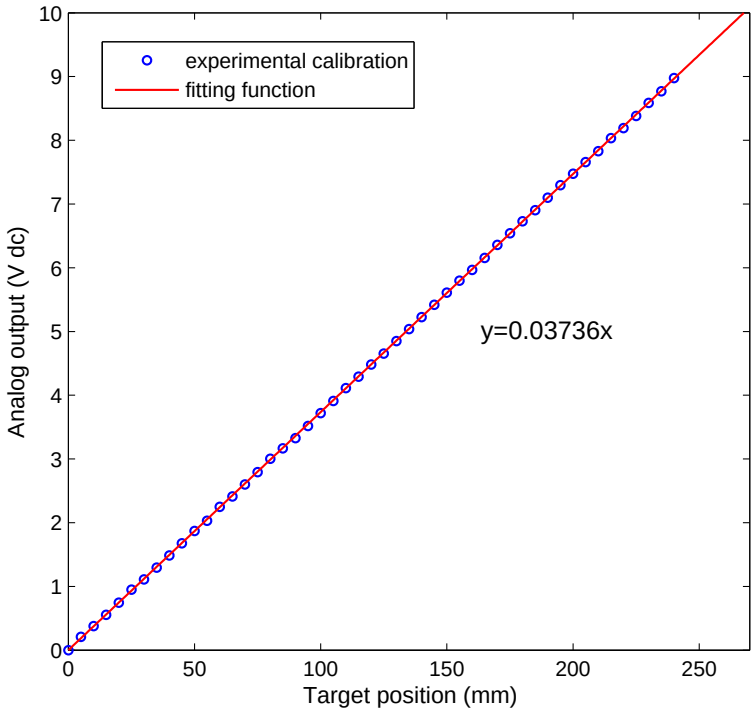

Figure 4.9: Fitting function for the analog outputs.

ation with 1/1.7 inch high-speed CMOS. For videos, it provides the frame rate up to 120 frames per second with the resolution of 640×480 pixels per frame in high-speed mode. In the present study, the standard mode was chosen with 640×480 pixels at 30 frames per second, which already satisfies the required accuracy and saves time in processing data.

Sideview recording is used to capture how the bottom moves. Furthermore, the camera was located parallel and overhead of the tank bottom surface for recording the wave run-up as presented in the lower part in Fig. 4.10. To prevent the water splash, the camera cannot be located too close to the water surface. Thus, two acrylic blocks with the same size were used to support the camera sitting on the top of the tank sidewalls and keep the camera lens parallel to the surface. Then, the shoreline movement can be measured uniformly regardless of the distortion caused by the angle between the lens and the surface. On the purpose of recording the shoreline motion simultaneously with the start of the bottom motion and the data acquisition, remote control is necessary.

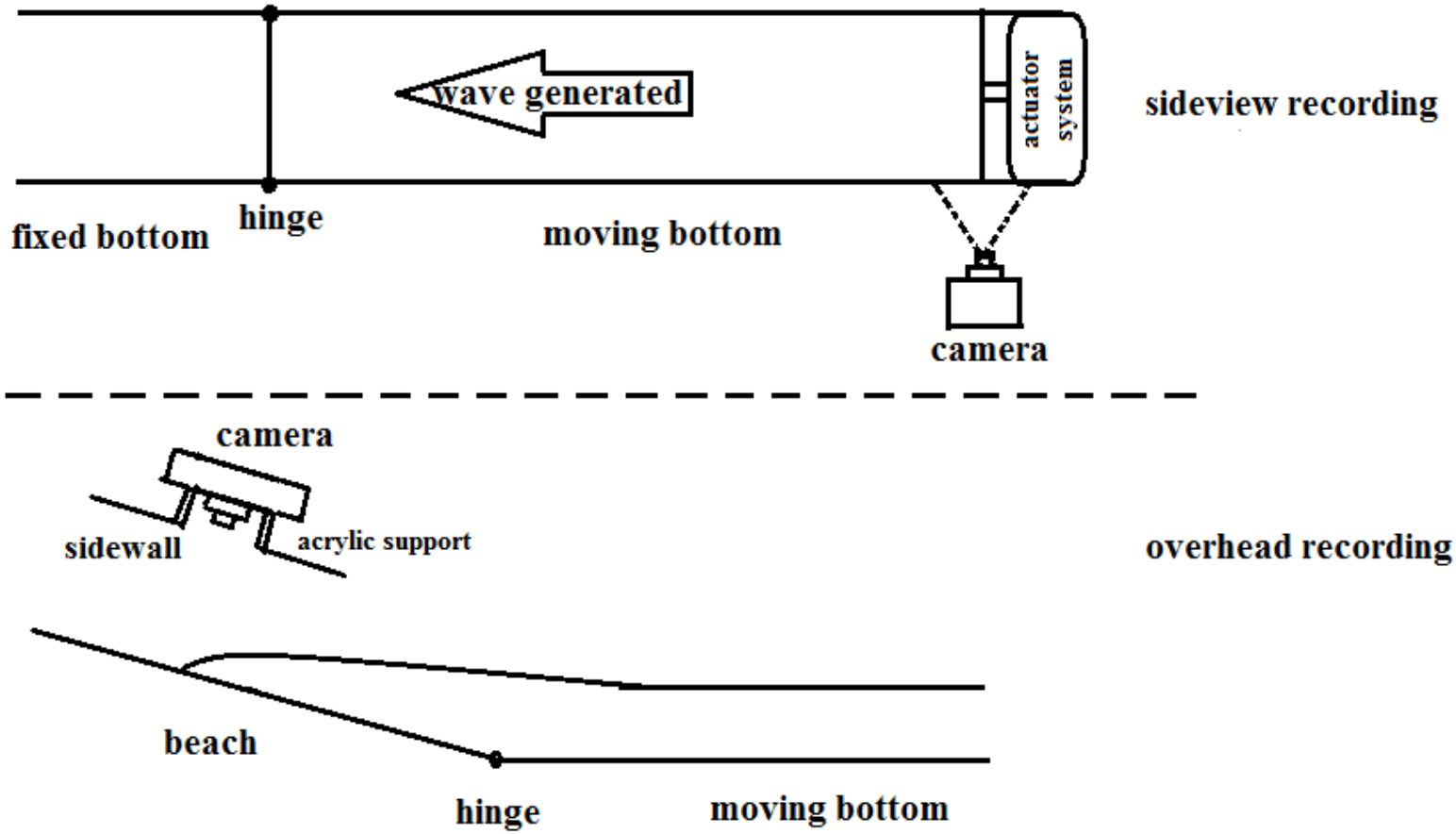

Figure 4.10: Camera configuration for bottom motion verification and wave run-up investigation.

The camera allows wireless connection for controlling the camera remotely through a smartphone based on its Bluetooth® Smart technology. Meanwhile, a specified smartphone app 'EXILIM Connect' is required which involves smartphone-pairing option, remote-control option and a monitoring screen. Fig. 4.11 shows a snapshot of the remote mode with a screen monitoring the shoreline motion. The button at the mid bottom is used to start shooting, while the button at the right bottom is a switch of choosing either picture capturing or video recording.

Figure 4.11: Snapshot of the remote mode of EXILIM Connect.

4.2.5 Data Acquisition System

The wave gauge was powered and connected to a data acquisition device on the circuit as shown in Fig. 4.12. By connecting the ultrasonic sensors to the National

Instruments^{TM}Low-Cost USB Data Acquisition (DAQ) 6003, the analog outputs can be collected and processed by a computer through a USB port. The DAQ device can be found in Fig. 4.12 as well, which has a 16-position connector and a prototyping circuit board packed in the plastic housing. Meanwhile, the device has eight analog input (AI) channels and two analog output (AO) channels with 16 bits of resolution for the analog-to-digital converter, which is sufficient for the present study.

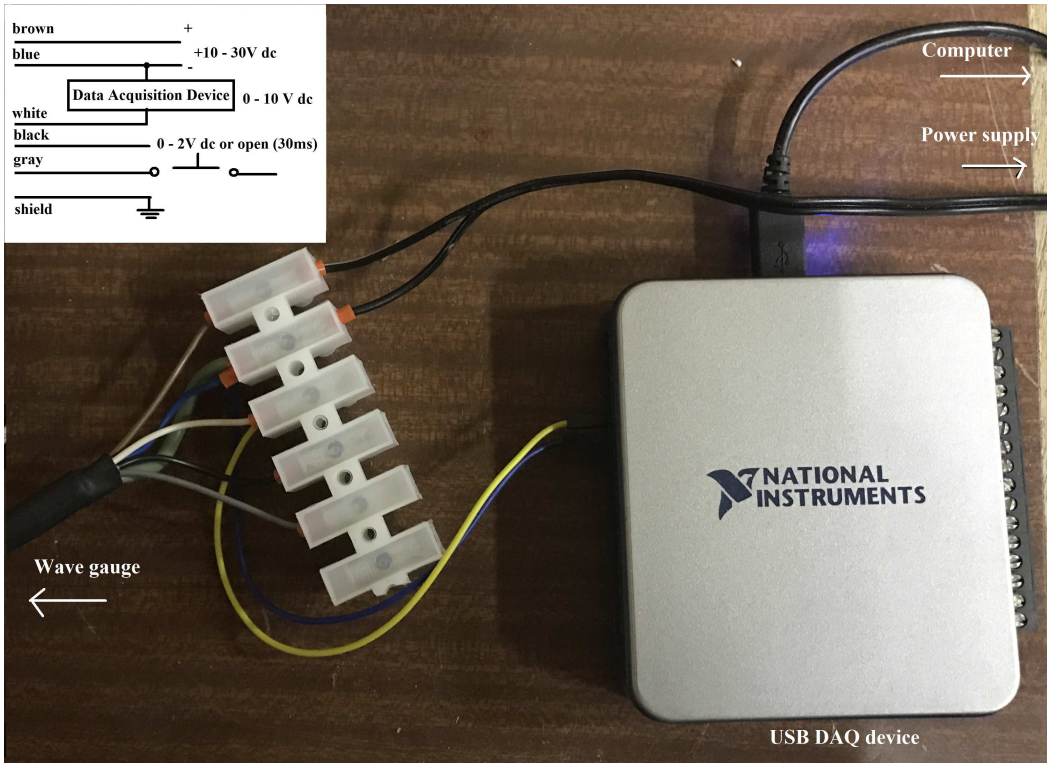

Figure 4.12: Snapshot of the block diagram of connecting the wave gauges to the National Instruments^{TM}DAQ device.

To enable the data monitored and processed efficiently, it requires NI LabView and NI-DAQmx both installed which were developed by National Instruments^{TM}. Once the device is identified by NI-DAQmx, NI LabView is used for further measurements. Fig. 4.13 presents the block diagram of the data acquisition by NI LabView. 'DAQ Assistant' can collect the voltage outputs from the channel connected and transfer them into digital outputs shown in the 'Waveform Graph'. Through 'DAQ Assistant', the voltage signals were determined in the range between 0 to 10 V which corresponds to the mode chosen for the wave gauge. The acquisition rate was chosen 50 Hz (up to 100 kHz) with 10 samples to read at

every loop. The total number of loops was defined 50 in the module of 'Numeric 2' while the number of every loop was shown in the numeric indicator. Moreover, it was programmed that the digital outputs were written in spreadsheets and saved as Excel files through the module 'Write to Measurement File'.

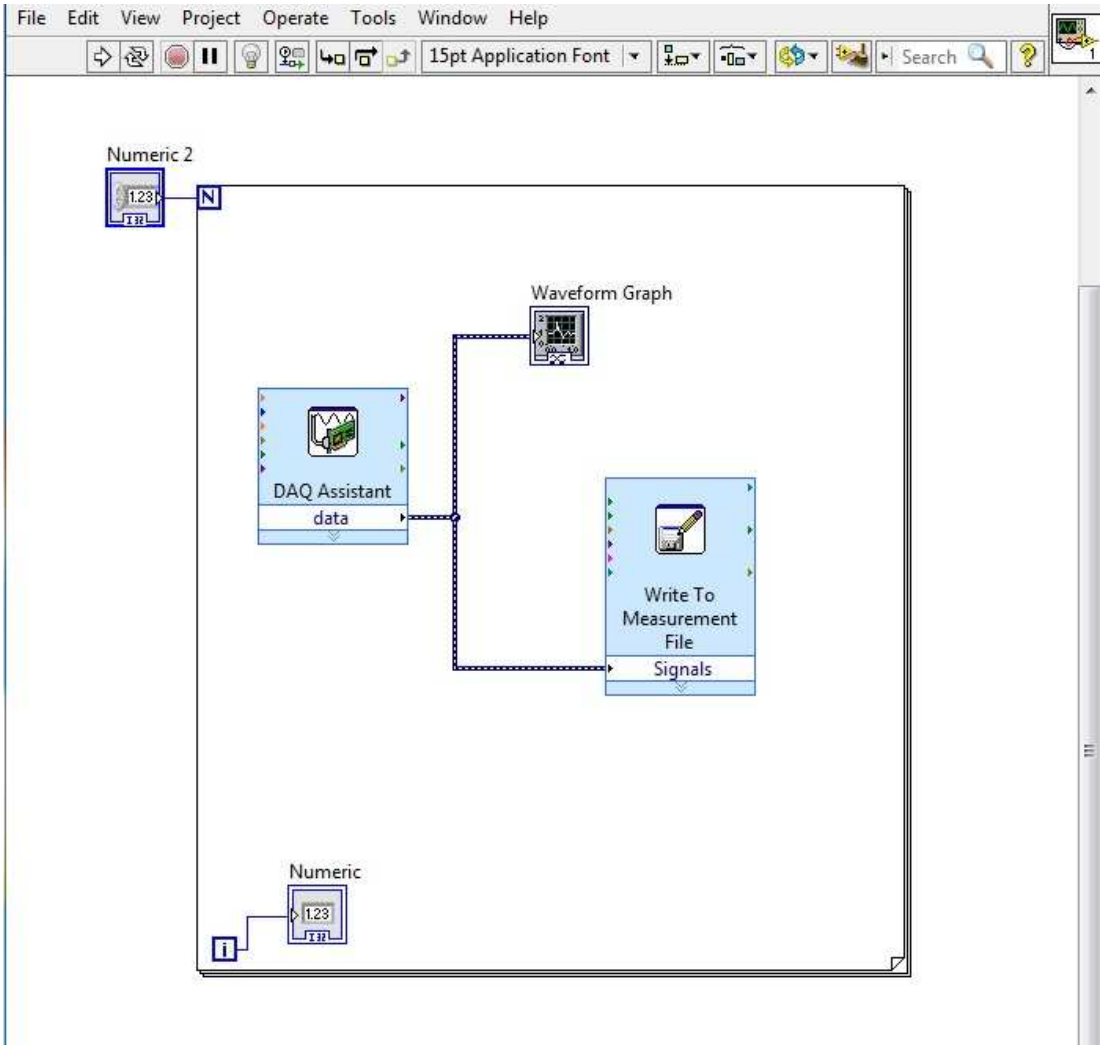

Figure 4.13: Snapshot of the block diagram of NI LabView.

4.3 Experimental procedure

This section presents the experimental procedures and the methods of processing the experimental data. Two measurements were performed as the set-up shown in Fig. 4.14 (wave generation) and Fig. 4.15 (wave run-up), respectively. Water surface elevation at a specified location was measured by acoustic wave gauges

in conjunction with a USB DAQ device. Wave run-up height was measured by a parallel overhead video camera which provides imaging information to be transferred into distance.

4.3.1 Measurements for wave generation

A schematic drawing of the experimental measurement for wave generation is depicted in Fig. 4.14. Waves were generated by different types of bottom motions driven by an electrical servo motor which was controlled by a computer. Two acoustic wave gauges were used to measure the free surface elevation at hinge (1 m from the right end) and middle of the fixed bottom (1.5 m from the right end) respectively with the accuracy of ± 0.5 mm. Both wave gauges were located at least 0.1 m above the still water surface which is within the sensing range of 0.03 m to 0.3 m and away from possible water splash. The two acoustic wave gauges were calibrated separately before the experiments as mentioned before. Note that the fixed bottom had no slope here.

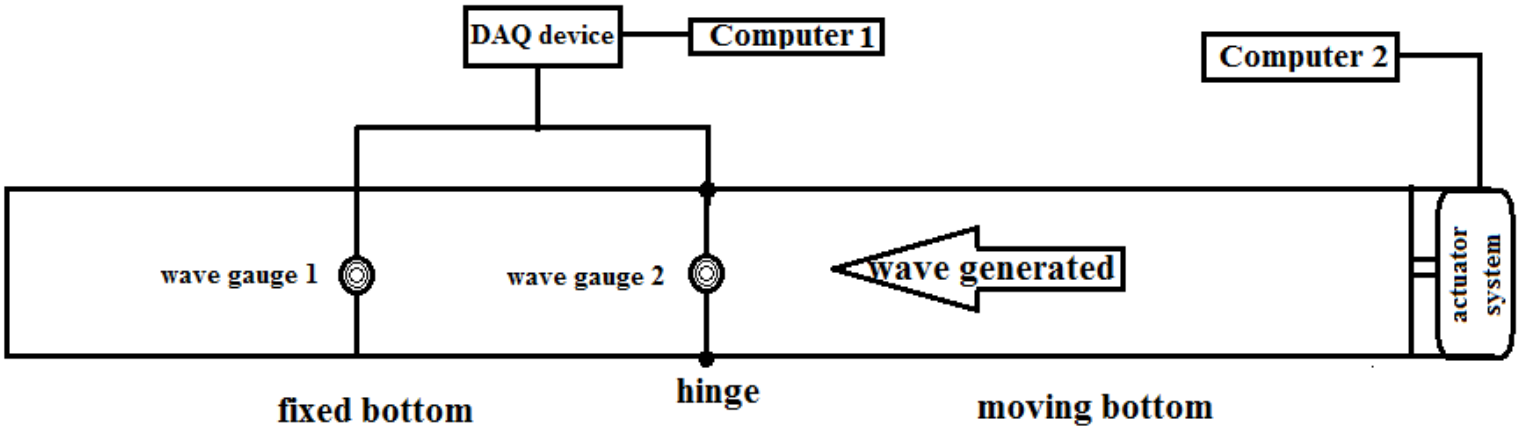

Figure 4.14: Experimental set-up for wave generation investigation.

The very first step of the experimental procedure is to measure the initial water surface (the initial voltage reading) and meanwhile ensure the constant water depth by a constant voltage reading. Once the computer 2 sends the programmed commands to the electrical servo motor, the actuator system will move the bottom to follow the expected trajectory at the required speed. As the bottom motion will generate a long wave propagating to the left end, the two overhead wave gauges measure the free surface elevation at two specified locations simultaneously for at least 10 s. Computer 1 monitors and controls the DAQ device to collect the analog outputs at 50 Hz from the two wave gauges.

Based on the outputs from the two wave gauges through two separative channels of the DAQ device, the voltage signals can be transferred into displacement as a function of time by the linear fitting function. After processing all the data, the time histories of the free surface elevation can be obtained. Note that it took 5 minutes between two consecutive runs of one case of experiments to ensure the same initial conditions. After adding water into the tank when necessary, dye was added to keep the colour of the water roughly in the same degree. The experiments are reproducible.

4.3.2 Measurements for wave run-up

The run-up height measurement was conducted in another manner of imaging processing. The experimental set-up for measuring the wave run-up is demonstrated in Fig. 4.15. The adjustable beach was controlled by a specific height difference between the two legs by turning the wheel on the right leg for a specific slope. The wave generation was executed in the same way to the wave generation experiments that computer 2 was used to control the electrical servo motor. As the hinge is the intersection point of the generation part and beach part, the waves at the hinge have been regarded as the incident waves for running up the beach. One acoustic wave gauge was used to measure the free surface elevation at the hinge.

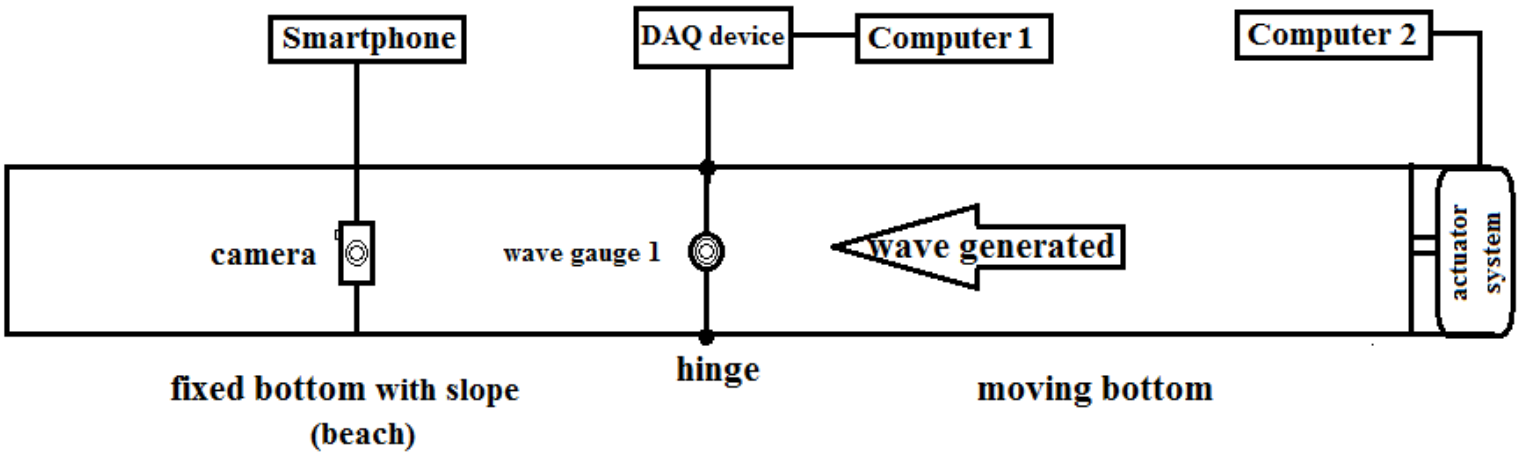

Figure 4.15: Experimental set-up for wave run-up investigation.

Computer 1 was used for data acquisition from the wave gauge 1 through a DAQ device. Moreover, a smartphone was used to control the video camera remotely. The two computers and the smartphone triggered the device they need to control simultaneously. In other words, the wave gauge began to measure the water surface displacement and the camera started its recording at once the bottom moved. The experiments were repeated two or three times to ensure the synchronicity as it was realised manually. The video camera CASIO® EXILIM ZR3500 was mounted overhead of the beach and parallel to the beach. A scale was attached to the beach surface under the membrane as a reference for measurement as shown in Fig. 4.16. The grid lines spacing on the scale was 0.02 m, supplying sufficient spatial precision. Then, the maximum run-up height can be measured by finding the furthest location the wave front can reach, which is easily identified by the interface between wet and dry area, in particular when the water is dyed. Note that run-down cannot be observed as the interface would be too wet and vague to identify the shoreline position.

Figure 4.16: Photo of a wave front at its maximum run-up.

For processing the graphical data from the videos, all the frames of the video files were saved as individual .jpg files by MATLAB firstly. The pictures with the

furthest shoreline location captured were picked visually and manually. Then, software called PlotDigitizer was used to digitise the shoreline location, by defining the scale of x and y axes and tracking the shoreline curve. Here, the physical grid lines on the scale aided to determine the coordinates for digitisation precisely. As the shoreline cannot be straight perfectly, the furtherest location was determined by averaging a large amount of points along the shoreline curve. Hence, in order to get the maximum run-up height, the horizontal distance between the slope foot and the shoreline were transferred into height according to the beach slope. Furthermore, as all the frame files were named chronologically, the time of the maximum run-up can be obtained easily due to the shooting frequency of 30 fps.

The time histories of free surface elevation at hinge were obtained in the same way used in the wave generation experiments. Similarly, at least 5 minutes between two consecutive runs of experiments was required for reproducibility. Dye should be supplemented when necessary.

4.3.3 Scale effects

Although this study does not aim to simulate in-situ tsunamis in the wave tank of this size now, the scale effects are discussed compared to a realistic tsunami as shown in Fig. 1.1 as a prototype and a wave tank with larger size (enabling deeper water depth tested). The deviation of the force ratios between the model scale and the prototype scale can give rise to inaccuracy, in particular for wave run-up owing to the small water depth. Table 4.1 shows the comparison of scale effects between the in-situ tsunami, the experiments based on the varying water depth in Table 4.2 and 4.3, and a model in a wave tank of larger size with h_0 =0.3 m. The scale effects discussed in this section are due to the Froude number, the Reynolds number and the Weber number. The Froude number is a ratio between inertia and gravity, which is defined as $F_r = c^2/gh_0$ with wave phase velocity $c = \sqrt{gh_0}$ for simplicity. Thus, it is $F_r = 1$ for the models in this wave tank, but actually greater than 1 in terms of wave height. Compared to the prototype scale, the

Froude number is well scaled. The Reynolds number is a ratio between inertia and viscous forces. The Reynolds number in constant water depth is defined as $R_e = \sqrt{gh_0}h_0/\nu$ with the kinematic viscosity of water ν of 10^{-6} for simplicity. It is seen from Table 4.1 that the values are still large for the experiments done in this wave tank. Surface tension may play a role in small scale models when the waves reach the scale of capillary waves. The Weber number, a ratio between inertia and surface tension forces, is defined as $W_e = \rho g h_0^2/\iota$ with the water density ρ and the surface tension for 20^oC water ι of 0.073 Nm^{-1} for simplicity. Peakall and Warburton (1996) suggested the range of critical values of Weber numbers from 10 to 120, within which the model will induce the effect of surface tension. Water depth h_0=0.02 m and 0.025 m fell into the range which may cause a degree of distortion of the experimental results. However, as water depth decreases significantly during wave run-up on slope, the Reynolds number and the Weber number decrease accordingly at the wave front where viscous force or surface tension could become dominant.

Table 4.1: Scale effects between the in-situ tsunamis and experiments in laboratory.

	Iwate South	Experiments	Experiment (h_0 =0.3 m)
Froude number (F_r)	1.02	1	1
Reynolds number (R_e)	9.13×10^9	0.88 to 4.6×10^4	5.15×10^5
Weber number (W_e)	5.59×10^9	54 to 484	1.21×10^4

4.3.4 Reducibility of experiments

Experiments are repeated a second time to ensure the repeatability. For example, Fig. 4.17 shows two repetitions of the time history of the free surface elevation at the hinge with small difference which is acceptable due to the accuracy of the wave gauge ($\pm$0.5 mm).

Moreover, the bottom motion driven by the actuator should be verified before experiments. For this purpose, the camera was located normal to the right end of the moving bottom at roughly 0.5 m far from the tank sidewall, which can be

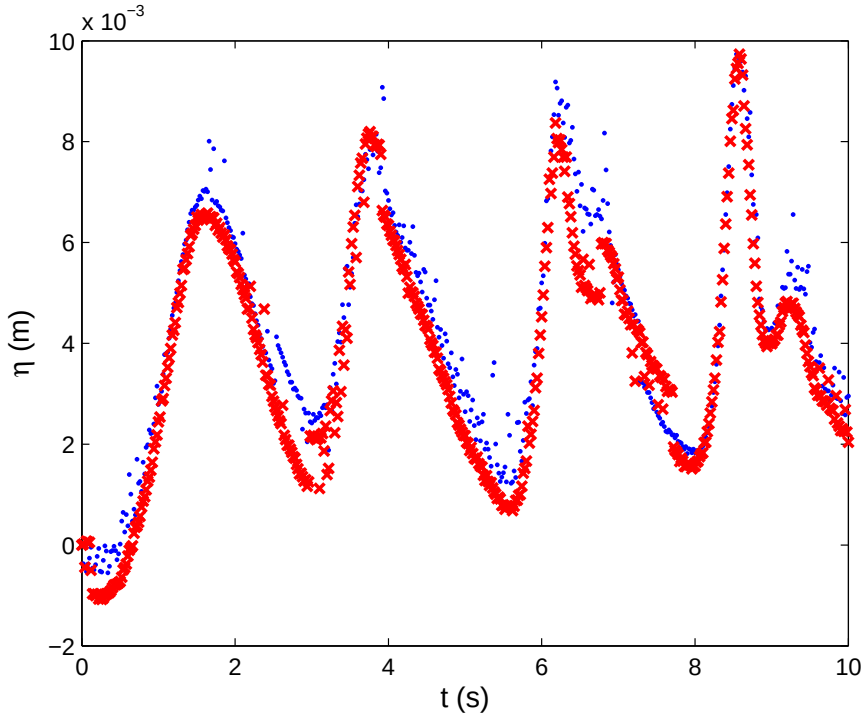

Figure 4.17: Comparison of two repetitions of the time history of η at the hinge.

found in the upper part in Fig. 4.10. A tripod was used to adjust the position of the camera. The lens was adjusted to be as high as the initial location of the moving bottom end. Based on the recorded videos of different bottom motions, the marked points at the bottom end were tracked as a function of time. Finally, the tracked time histories of the bottom motion were compared to the theoretical trajectories for verification. Fig. 4.18 shows a verification test with the bottom motion amplitude of 0.03 m for upward, downward and up-downward motions, respectively. A duration time of 1.5 s was applied to the first two motions while 3.0 s was applied to the last up-downward motion. Acceptable agreements can be found for the three different types of bottom motion, respectively. The difference can be caused by the ignorance of the acceleration in the theoretical solutions. This may also cause the deviation between the theoretical and the experimental results discussed in the next chapter (e.g., Fig. 5.1, 5.2 and 5.18). However, as the motion duration time is small compared to the time history, this should not be the main reason for the deviation.

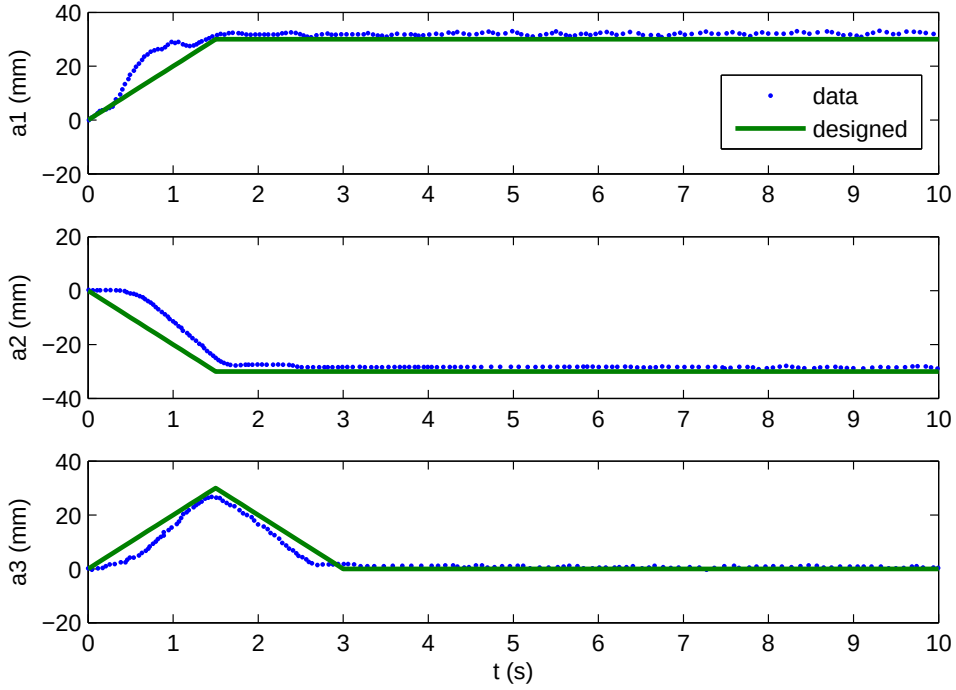

Figure 4.18: Verification of the physical bottom motion compared to the designed motion (blue dot indicates the tracking data and solid line indicates the designed motion curve).

4.3.5 Bottom motion parameters

The ranges of the motion characteristics for conducting the experiments and available investigations are demonstrated in detail here. Motion displacement a and duration time b are the two defining parameters of the basic upward, downward or combined bottom motions as shown in Fig. 4.19 which depicts the practical motions based on the general concept of Fig. 3.2. It is noted that the water depth is limited by the maximum value of the ratio $\alpha = h_0/L$ being 0.07 as concluded in section 4.1. After some trials, the maximum allowable bottom motion displacement without causing splash-up at the end wall was found to be $a \leq 40$ mm. On the other hand, the corresponding rotating angle would be 0.013π, which is small enough to ignore the horizontal velocity induced by the moving bottom as long as the bottom motion is not very strong.

For wave generation investigation, three values of α 0.04, 0.05 and 0.06 were tested. Thus, the bottom motion displacement within the range of 5 to 40 mm

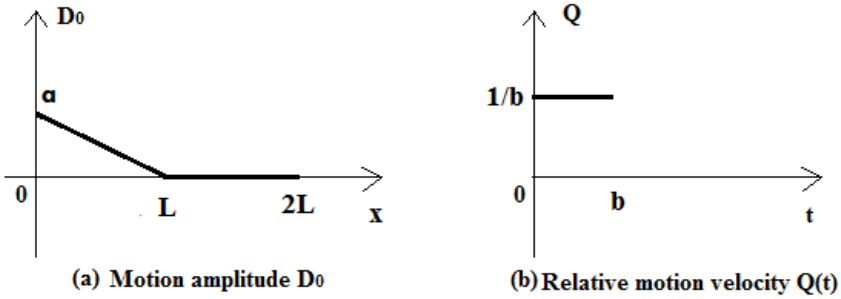

Figure 4.19: The bottom motion of the wave maker used in the experiments.

Table 4.2: Parameters (a and b) of the bottom motions with different h_0 for wave generation investigation.

$h_0(mm)$	$a(mm)$	$b(s)$
40	5, 10 $\cdots$, 40	0.5, 1.0, 1.5, 2.0
50	5, 10 $\cdots$, 40	0.5, 1.0, 1.5, 2.0
60	5, 10 $\cdots$, 40	0.5, 1.0, 1.5, 2.0

were chosen in this study. Moreover, the bottom motion duration time ranges from b=0.5 to 2.0 s. Ranges of the parameters used are summarised in Table 4.2.

For wave run-up investigation, available water depth would be smaller limited by the length of the beach. Thus, three values of α 0.02, 0.025 and 0.03 were tested. Accordingly, the bottom motion displacements tested were reduced to the range of 5 to 25 mm. Similarly, bottom motion duration time ranging from b=0.5 to 2.0 s were still used. Table 4.3 shows the ranges of the parameters used in the run-up experiments. Moreover, the results were compared between three slopes of 1/15, 1/20 and 1/25.

Table 4.3: Parameters (a and b) of the bottom motions with different h_0 and slope γ for wave run-up investigation.

$h_0(mm)$	$a(mm)$	$b(s)$	γ
20	5, 10 $\cdots$, 20	0.5, 1.0, 1.5, 2.0	1/15, 1/20, 1/25
25	5, 10 $\cdots$, 20	0.5, 1.0, 1.5, 2.0	1/15, 1/20, 1/25
30	5, 10 $\cdots$, 25	0.5, 1.0, 1.5, 2.0	1/15, 1/20, 1/25

Chapter 5

Results and discussion of results

This chapter shows the experimental measurements compared to the theoretical results for wave generation investigation (Section 5.1) and wave run-up investigation (Section 5.2), respectively. Parametric analyses aim to examine the effects of the bottom motion on the generated long waves and the wave run-up height.

In this chapter, results are described in terms of dimensionless variables. The constant water depth h_0 is used to normalise the length parameters, so the relevant dimensionless variables marked by $'$ are given by

$$L' = \frac{L}{h_0},\ x' = \frac{x}{h_0},\ h' = \frac{h}{h_0},\ \eta' = \frac{\eta}{h_0},\ \zeta' = \frac{\zeta}{h_0},\ a' = \frac{a}{h_0},\ A' = \frac{A}{h_0}, \tag{5.1}$$

while time is normalised by $L\left(gh_0\right)^{-1/2}$:

$$t' = t\sqrt{gh_0}/L,\ b' = b\sqrt{gh_0}/L,\ T' = T\sqrt{gh_0}/L, \tag{5.2}$$

where b, A and T denote the bottom motion duration time, the wave amplitude and the wave period, respectively. Moreover, as the length of the moving bottom is fixed in reality, the aforementioned depth ratio α is applied, denoting the constant water depth for each of the cases discussed later. Different α provides a wider range of a' and b' dimensionlessly. For convenience, primes denoting non-dimensionality have been dropped in the following discussions. After nor-

Table 5.1: Bottom motion parameters (a and b) of the bottom motions with different α in dimensionless form for wave generation investigation.

α	a	b
0.04	0.125, 0.250 $\cdots$, 1.000	0.31, 0.62, 0.94, 1.25
0.05	0.100, 0.200 $\cdots$, 0.800	0.35, 0.70, 1.05, 1.40
0.06	0.083, 0.167 $\cdots$, 0.677	0.38, 0.76, 1.15, 1.53

Table 5.2: Bottom motion parameters (a and b) of the bottom motions with different α and beach slope γ in dimensionless form for wave run-up investigation.

α	a	b	γ
0.020	0.25, 0.50 $\cdots$, 1.00	0.22, 0.44, 0.66, 0.88	1/15, 1/20, 1/25
0.025	0.20, 0.40 $\cdots$, 0.80	0.25, 0.50, 0.75, 1.0	1/15, 1/20, 1/25
0.030	0.167, 0.333 $\cdots$, 0.833	0.27, 0.54, 0.81, 1.08	1/15, 1/20, 1/25

malisation, the ranges of the parameters used for wave generation investigation and wave run-up investigation in Table 4.2 and Table 4.3 are shown in Table 5.1 and Table 5.2 in dimensionless form, respectively.

5.1 Wave generation investigation

In this thesis, simple bottom motions with constant velocity are considered. Based on the wave generation set-up shown in Fig. 4.3, the waves generated by the new wave maker are observed experimentally. Given the bottom motion, the numerical method enables to approximate the evolution of the free surface waves, while the analytical solution gives a rough estimation according to the coordinate system shown in Fig. 3.1.

The purpose of this section is to relate the wave amplitude A and the wave period T of the waves generated in the new wave tank in terms of the two parameters (a and b) of the simple upward and downward motions. First, it will be shown that there is good agreement between the experimental and theoretical results for all the cases in Table 5.1, even with the multiple reflections on both ends of the tank. It is straightforward to get A from experimental data, but T is more difficult to measure due to the presence of the reflected wave. Instead, the theoretical solutions in semi-infinite domain are used to estimate T. The good

agreement justifies this indirect way of measuring the period.

5.1.1 Analytical solutions of the tested cases of the bottom-tilting wave maker

Cases in which the bottom moves at constant speed from the initial position θ_m ($\theta_m > 0$) upwards or downwards are considered in the present study, where θ_m is also the maximum amplitude of the rotating angle. As shown in Fig. 3.1, the rotating angle θ can be represented as $\theta(t) = \theta_m(1 - t/b)$. Hence, the trajectory of the moving bottom $Y_w(x,t) = -h_0 + D_0(x)B(t)$ for the upward motion is described as

$$\begin{aligned} Y_w(x,t) &= -h_0 - (L-x)\tan\theta \\ &\approx -h_0 - (L-x)(\theta_m - \theta_m/b \cdot t) \\ &\approx -h_0 - D_0(x)(1 - t/b), \end{aligned} \tag{5.3}$$

or for the downward motion similarly:

$$\begin{aligned} Y_w(x,t) &\approx -h_0 + D_0(x)(1 - t/b) \\ &= -h_0 + B(t)D_0(x), \end{aligned} \tag{5.4}$$

where motion amplitude D_0 is already determined by (3.28). Thus, $B(t)$ is defined as

$$B(t) = \begin{cases} -(1 - t/b), & \text{upward motion,} \\ 1 - t/b, & \text{downward motion,} \end{cases} \tag{5.5}$$

so its time derivative $Q(t)$ is defined as

$$Q(t) = \begin{cases} 1/b, & \text{upward motion,} \\ -1/b, & \text{downward motion.} \end{cases} \tag{5.6}$$

Therefore, by substituting (5.6) into (3.37) for upward motion, the free surface

elevation at the hinge becomes

$$\eta\left(L,t\right) = \begin{cases} \dfrac{aL}{b\pi}\displaystyle\int_0^t du\int_0^\infty dk\,\frac{\sin^2\left(kL/2\right)}{\left(kL/2\right)^2}\frac{\cos kL}{\cosh kh}\cos\omega\left(t-u\right), & 0\le t\le b, \\ \dfrac{aL}{b\pi}\displaystyle\int_0^b du\int_0^\infty dk\,\frac{\sin^2\left(kL/2\right)}{\left(kL/2\right)^2}\frac{\cos kL}{\cosh kh}\cos\omega\left(t-u\right), & t>b. \end{cases} \tag{5.7}$$

Similarly, for downward motion, the bottom motion displacement leads to the free surface elevation at the hinge

$$\eta\left(L,t\right) = \begin{cases} -\dfrac{aL}{b\pi}\displaystyle\int_0^t du\int_0^\infty dk\,\frac{\sin^2\left(kL/2\right)}{\left(kL/2\right)^2}\frac{\cos kL}{\cosh kh}\cos\omega\left(t-u\right), & 0\le t\le b, \\ -\dfrac{aL}{b\pi}\displaystyle\int_0^b du\int_0^\infty dk\,\frac{\sin^2\left(kL/2\right)}{\left(kL/2\right)^2}\frac{\cos kL}{\cosh kh}\cos\omega\left(t-u\right), & t>b. \end{cases} \tag{5.8}$$

5.1.2 Comparison of experimental and theoretical results

The numerical results of the time-histories of the free surface elevation at the hinge and the mid bottom are compared to the experimental data, and examples are shown in Fig. 5.1 and Fig. 5.2 covering a wide range of bottom motion amplitude a and duration b. Note that the linear solutions are not included as they do not consider the wave reflection. The good agreements in Fig. 5.1 and Fig. 5.2 have verified the performance of the two numerical models based on the BE (Boussinesq equations) or NSWE (nonlinear shallow water equations) system with the bounded domain same to the wave tank. Clearly, due to the shorter distance away from the right tank end, the free surface waves at the mid bottom are much more easily influenced by the reflection than the waves at the hinge. Note that the measurements at the mid bottom are just used to facilitate the verification of the numerical models. The interest of observation is the free surface waves at the hinge.

For small a, the wave amplitude is small and sometimes in the order of the

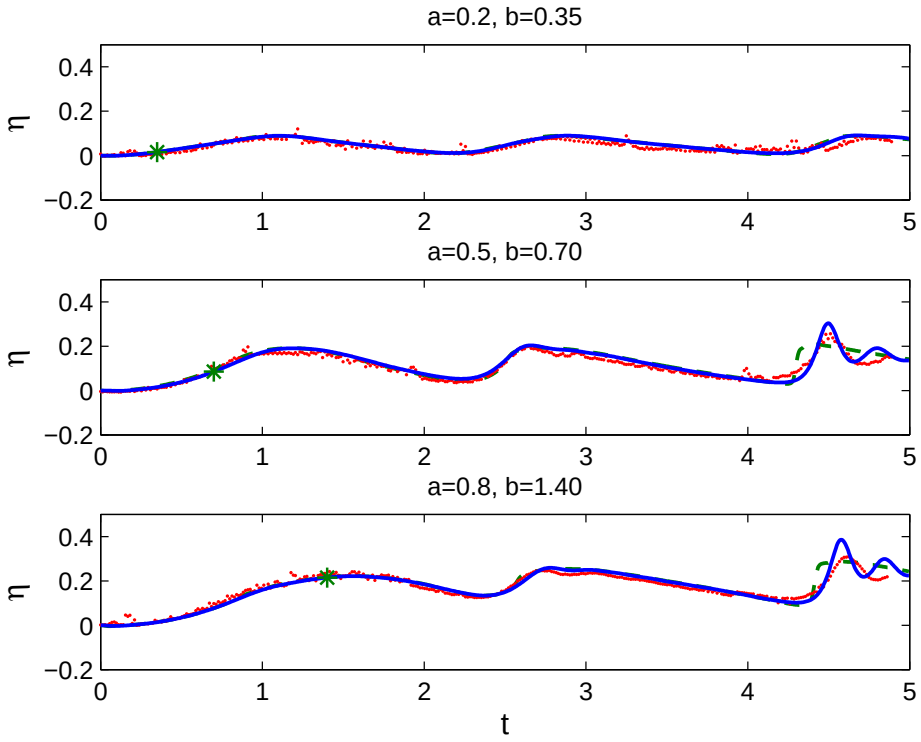

(a) upward motion

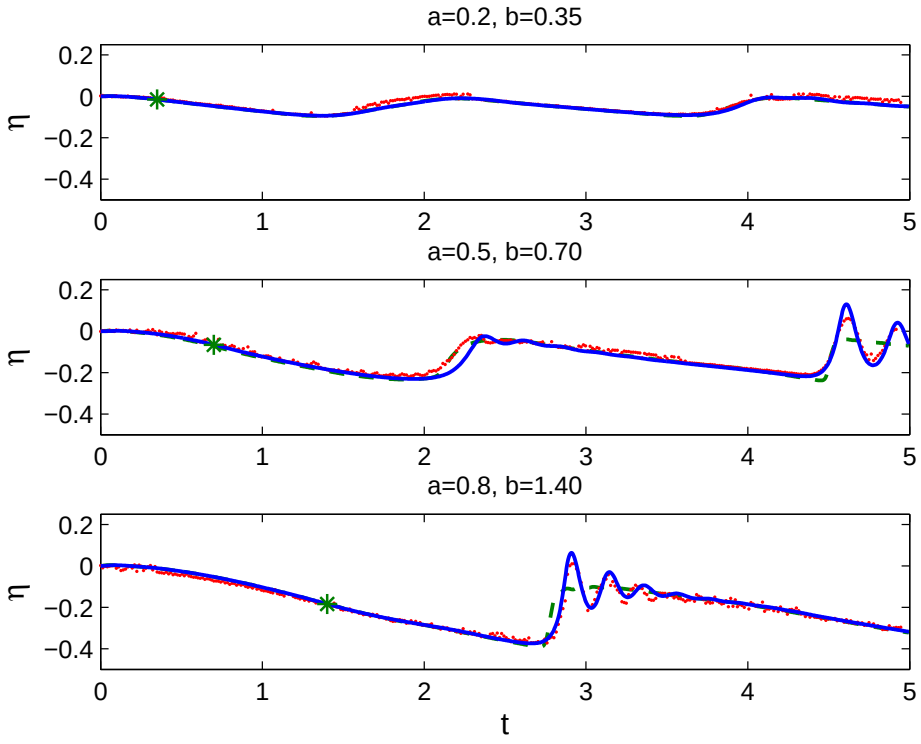

(b) downward motion

Figure 5.1: Comparison of the free surface elevation at the hinge with $\alpha = 0.05$: solid line, numerical results by BE; dashed line, numerical results by NSWE; dotted line, experimental data; asterisk, time when the bottom motion stops.

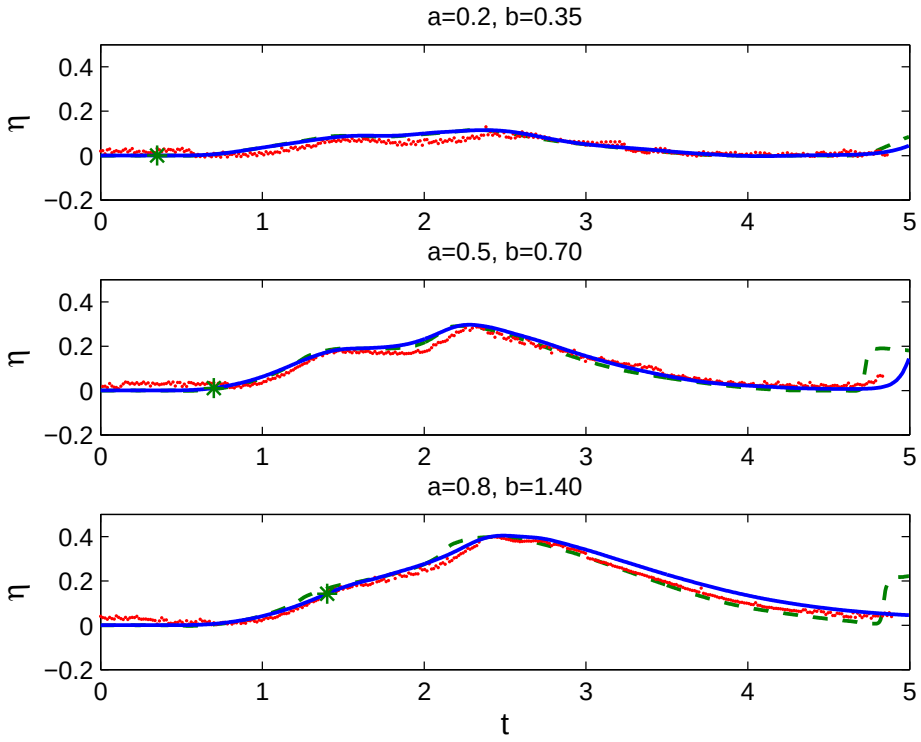

(a) upward motion

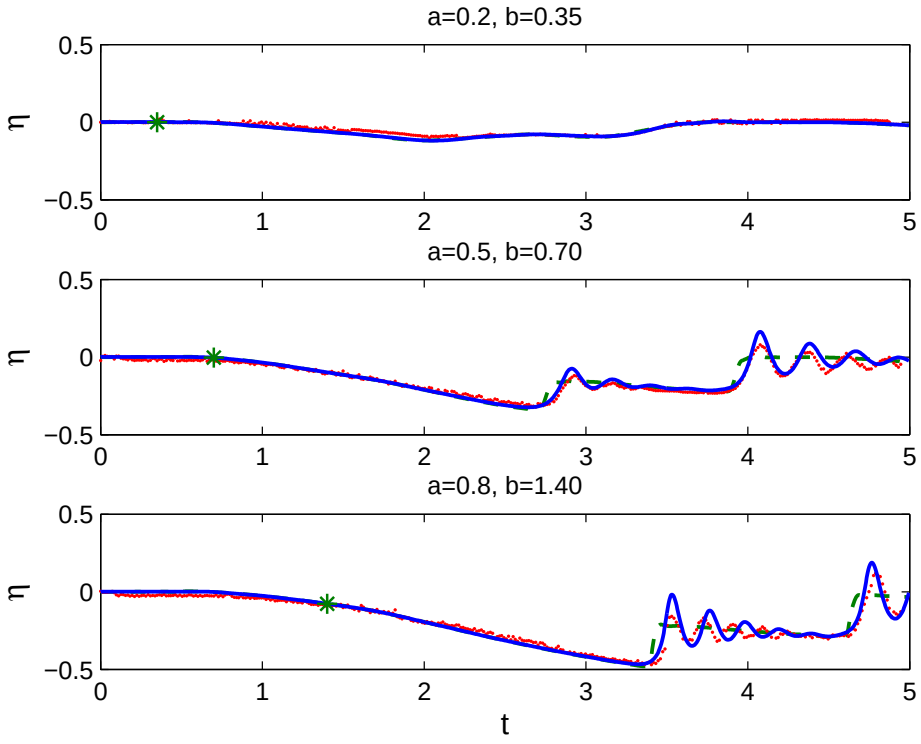

(b) downward motion

Figure 5.2: Comparison of the free surface elevation at the mid bottom with $\alpha = 0.05$: solid line, numerical results by BE; dashed line, numerical results by NSWE; dotted line, experimental data; asterisk, time when the bottom motion stops.

uncertainty ($\pm$ 0.01 non-dimensionally for $\alpha = 0.05$) of the wave gauges, which resulted in scattering of the experimental data for $a = 0.2$ in Fig. 5.1 and Fig. 5.2. Nevertheless, both the Boussinesq equations and the NSW equations show good agreement with the experimental data. Eventually after the first peak of the positive wave generated by the upward motion or the first nadir of the negative wave generated by the downward motion, dispersion becomes no longer negligible, and the Boussinesq equations capture it better than the NSW equations. Thus, only the model based on the Boussinesq equations is used to estimate the wave amplitude and period of the generated waves numerically as discussed in subsection 5.1.3 and 5.1.5. It is also observed that the resulting waves become increasingly asymmetric with greater motion displacement because of the growing nonlinearity, in particular the negative waves. In addition, it can be found that the maximum wave amplitudes of the resulting waves are smaller than the corresponding motion displacement, roughly half as much as the relevant motion amplitude for the most cases.

5.1.3 Wave amplitudes of the waves generated using the bottom-tilting wave maker

The amplitudes of the waves generated in the new wave tank are plotted as a function of the bottom motion amplitude a and the duration b for the three water depth ratios $\alpha = 0.04$, $\alpha = 0.05$ and $\alpha = 0.06$ in Fig. 5.3, Fig. 5.4 and Fig. 5.5, respectively. The smallest waves by the bottom motions with the smallest a and the greatest b for $\alpha = 0.05$ and $\alpha = 0.06$ are not included. The scattering of the data for the smallest waves limited by the accuracy of the wave gauge makes it difficult to determine the wave amplitude and period.

The amplitude was defined by the elevation of the first peak for the positive waves or the first nadir for the negative waves. It is observed that greater motion amplitude a and smaller bottom motion duration b leads to increasing wave amplitude A for both upward and downward motions. Hence, the wave amplitude is greater at smaller α accompanying with greater a and smaller b. However

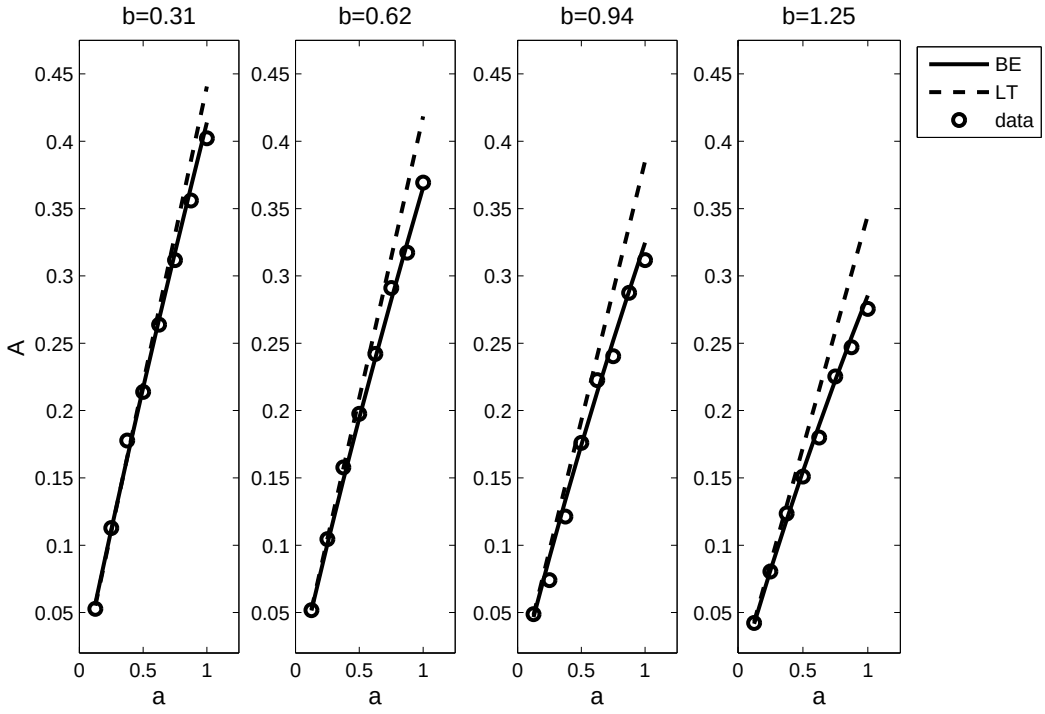

(a) Amplitude A for upward motions

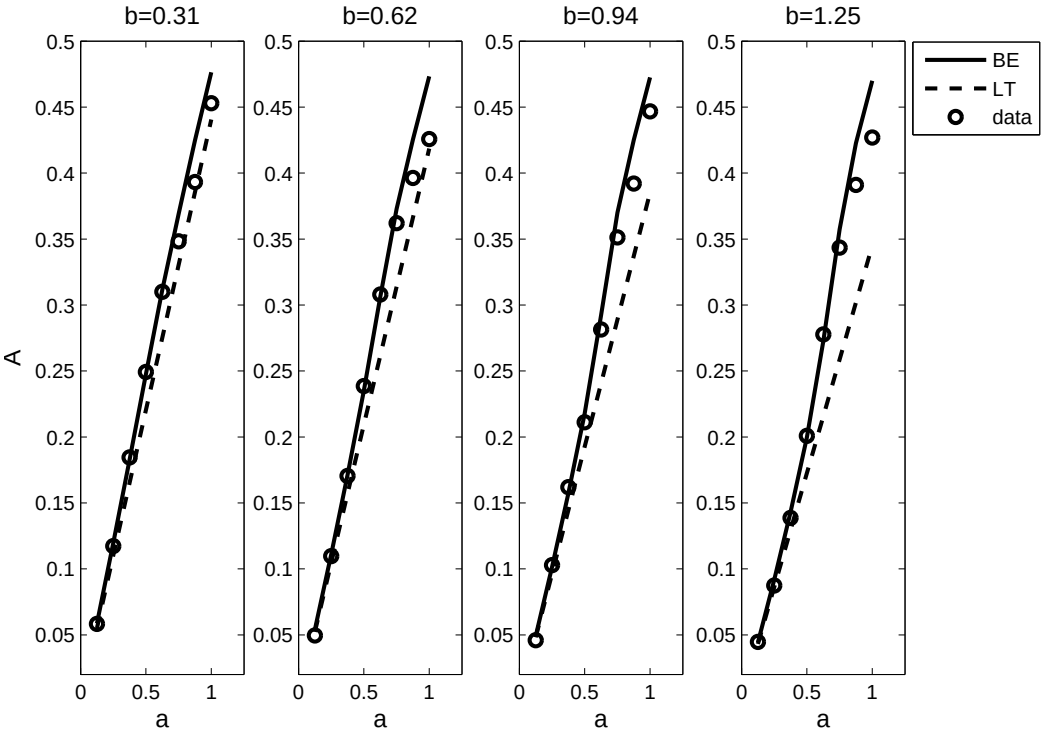

(b) Amplitude A for downward motions

Figure 5.3: Wave amplitude A plotted against varying a and b with $\alpha = 0.04$: circle, experimental measurements; solid line, numerical results by BE; dashed line, analytical results by LT.

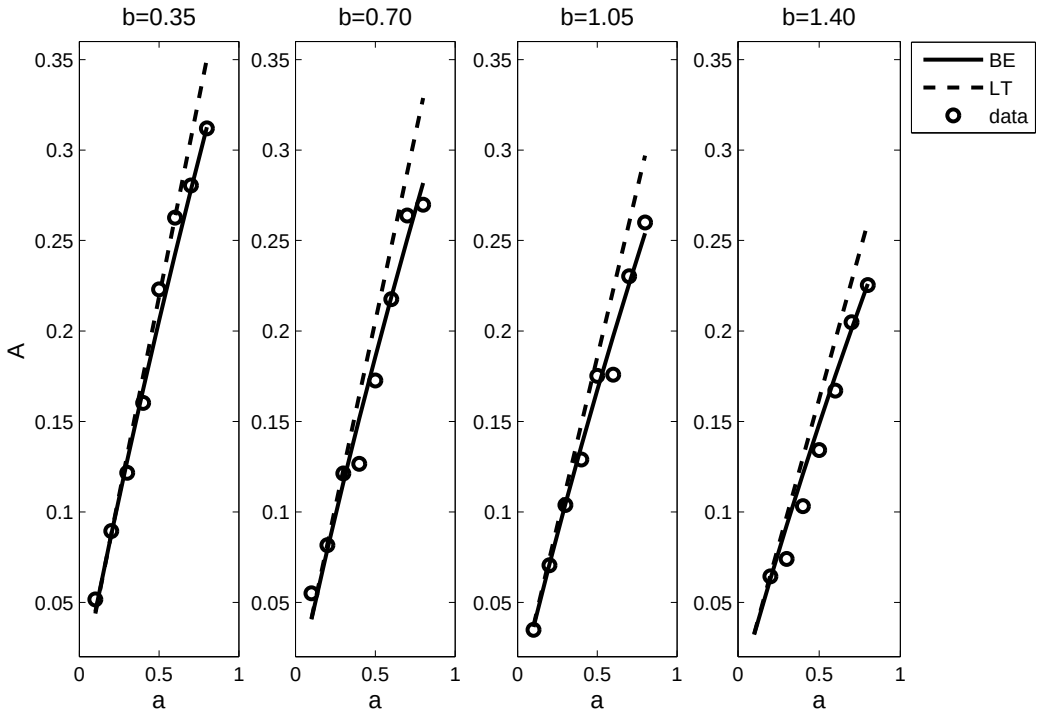

(a) Amplitude A for upward motions

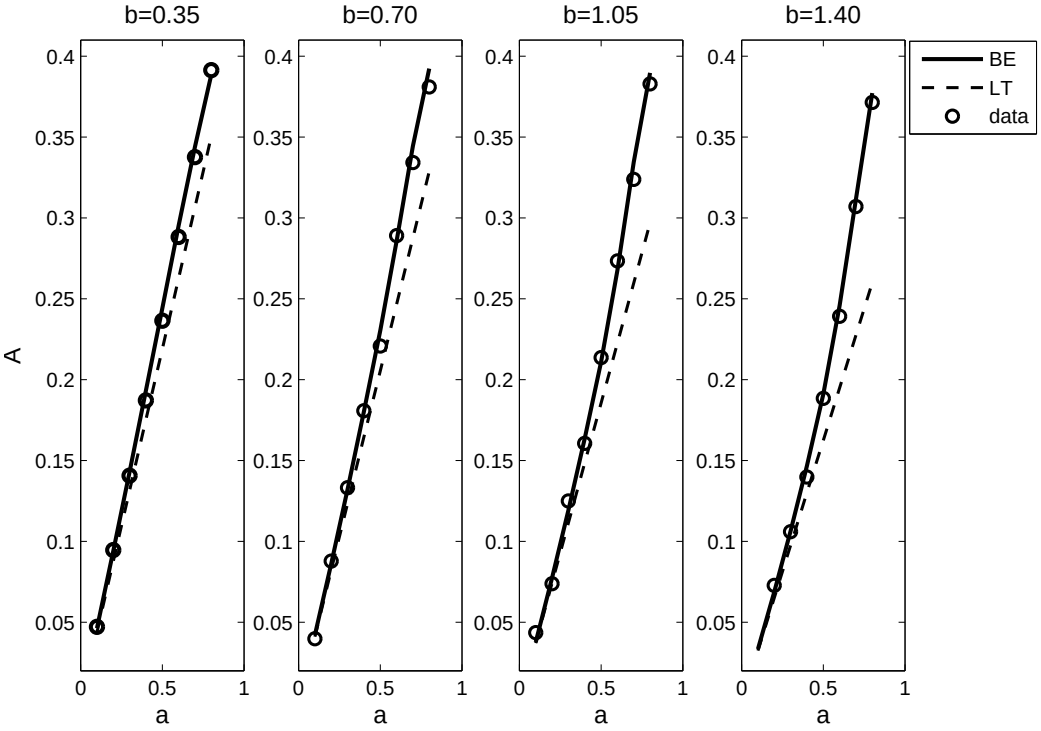

(b) Amplitude A for downward motions

Figure 5.4: Wave amplitude A plotted against varying a and b with $\alpha = 0.05$: circle, experimental measurements; solid line, numerical results by BE; dashed line, analytical results by LT.

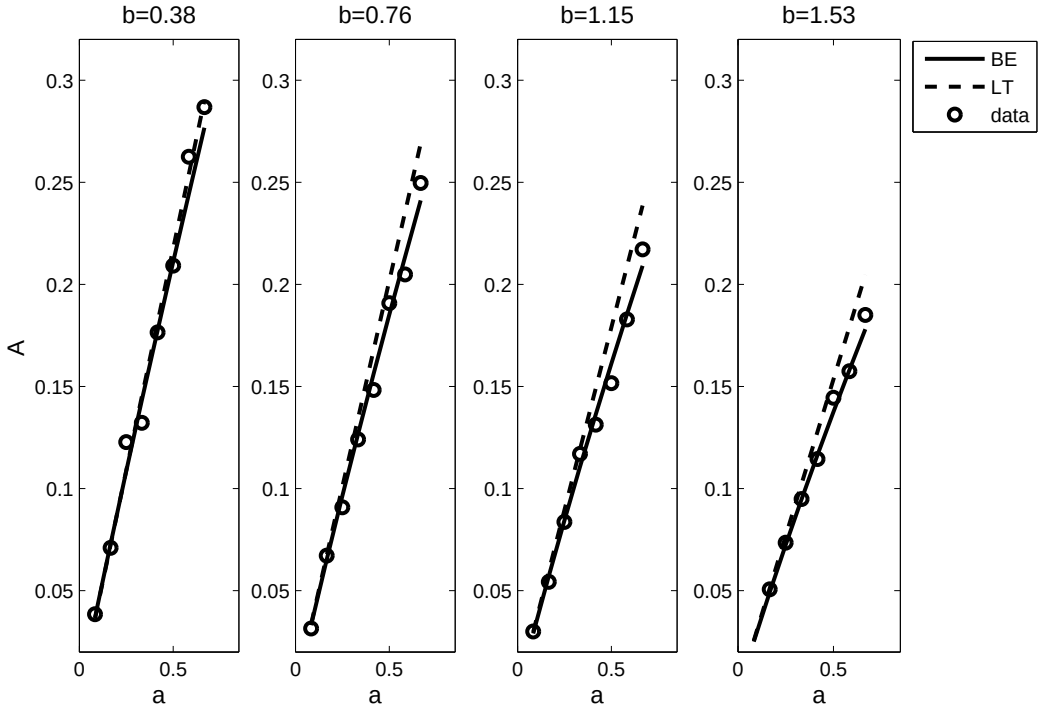

(a) Amplitude A for upward motions

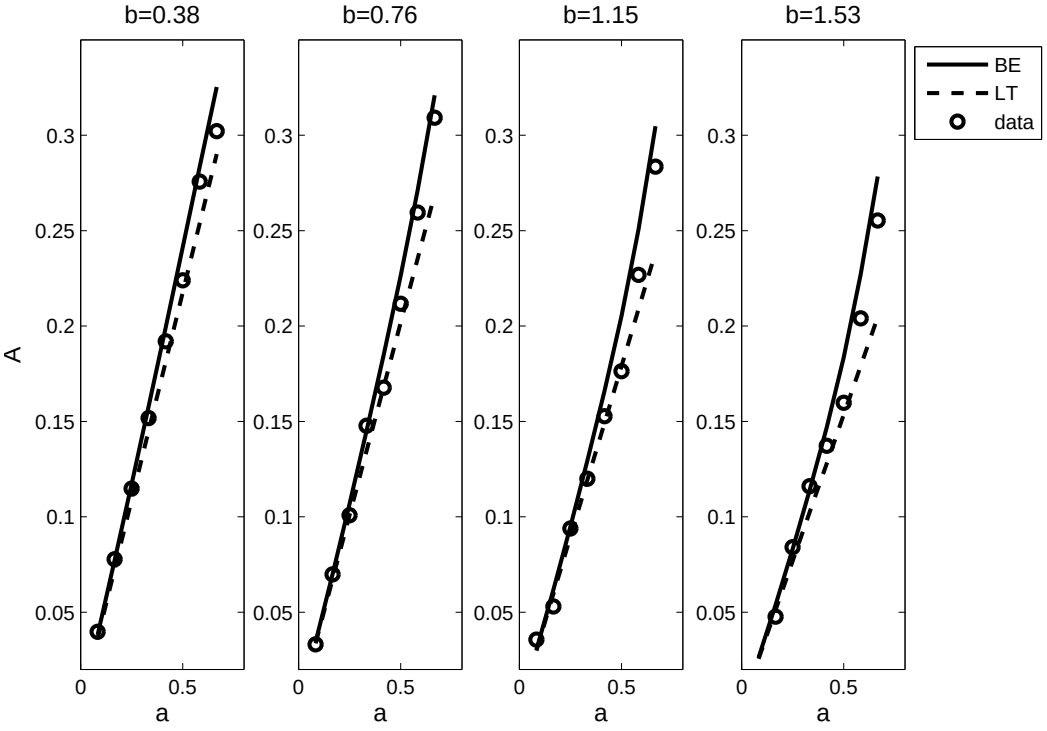

(b) Amplitude A for downward motions

Figure 5.5: Wave amplitude A plotted against varying a and b with $\alpha = 0.06$: circle, experimental measurements; solid line, numerical results by BE; dashed line, analytical results by LT.

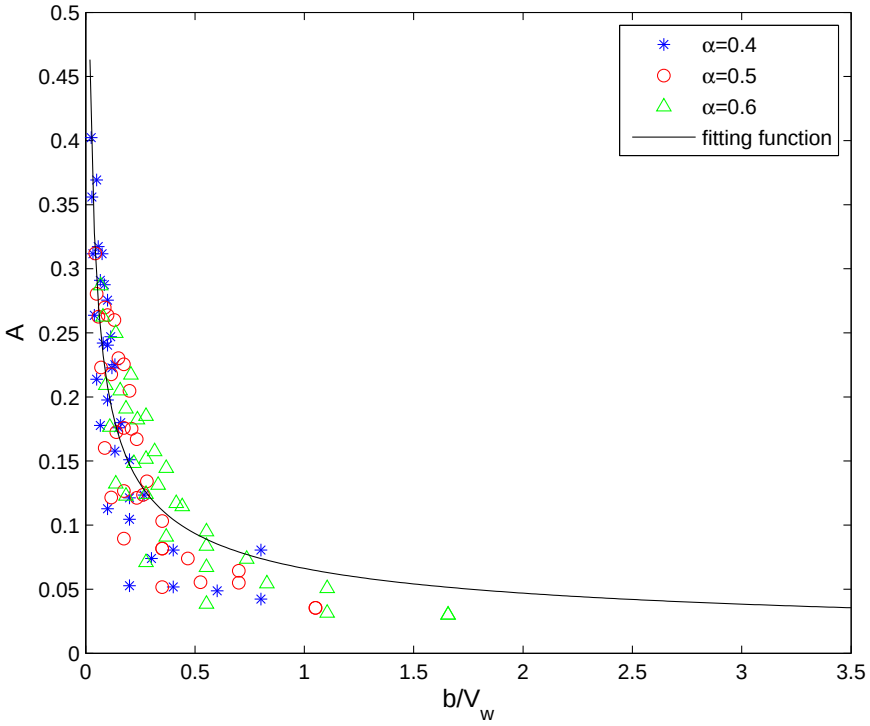

(a) upward motion

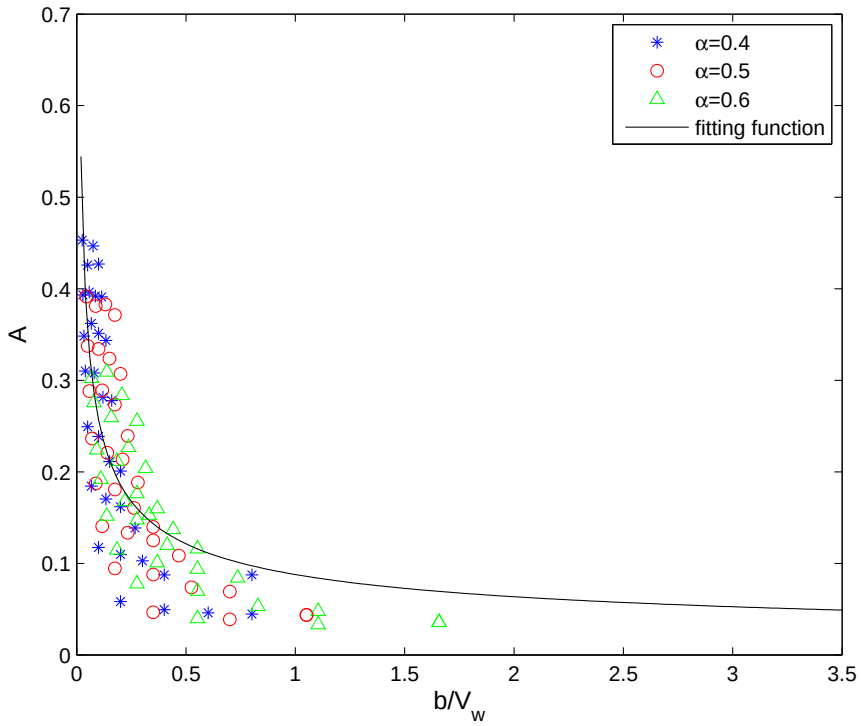

(b) downward motion

Figure 5.6: Plots of wave amplitude A as functions of b/V_w: solid line, the fitting function; $*$, $\alpha = 0.04$; $\circ$, $\alpha = 0.05$; $\triangle$, $\alpha = 0.06$.

effects of the motion duration on the wave amplitude become less important for downward motions as the motion amplitude increases. In particular in cases with $\alpha = 0.04$, wave amplitudes are almost the same at the maximum a regardless of the varying b. This suggests that early disintegration of the high-amplitude leading depression wave caused by dispersion plays a main role in determining the wave amplitude of negative waves. Early disintegration can be seen in Fig. 5.1 and Fig. 5.2 for greater downward motions.

In an effort to succinctly describe the wave amplitude in terms of a and b, it is instructive to consider scaling analysis. Similarly, Walder et al. (2003) solved the problem of waves generated by sudden change of water volume on a sloping bottom. In their experimental study of tsunami generation due to subaerial mass flow, Walder et al. (2003) argued that amplitude of tsunami is mainly a function of volume flux of displaced water. In the present research, the volume (per unit width) of displaced water by the bottom-tilting wave maker is $V_w = aL/2$, which was in motion for the duration time of b. Following Walder et al. (2003), wave amplitudes measured from the experiments are plotted against the inverse of the volume flux, that is b/V_w, in Fig. 5.6. It can be found that the wave amplitude is able to be describe by a function of a, b and L. The two fitting functions are of form $A = m(b/V_w)^{-n}$, and the results are summarised in Table 5.3. Walder et al. (2003) reported $m = 1.32$ and $n = 0.68$. On the other hand, the values of m for our experimental data are smaller possibly because of the different time normalisation, different generation mechanism and absence of acceleration for most of the bottom displacement in our cases.

Table 5.3: Parameters (m and n) of the fitting functions for different bottom motion type.

motion type	m	n
upward	0.06622	0.4972
downward	0.08745	0.4663

5.1.4 Estimation of wave period

Due to the limited length of the wave tank, the reflected wave makes measuring T rather difficult. Two different methods were employed to estimate the wave periods. Based on the time-history of surface elevation at the hinge, one way is to measure time from the beginning of the wave (where the water surface elevation is 1% of the wave peak amplitude) to the peak of the wave, namely wave peak time T_a. Then the wave period is estimated to be $T = 2T_a$. Note that the theoretical estimation of T_a is obtained in the domain same long to the wave tank. This method, however, works only for the waves that are more or less symmetric. Waves generated using the bottom-tilting wave maker become increasingly skewed as the ab^{-1} grows. In those cases, theoretical solutions in semi-infinite domain are used instead. Using the numerical results from the Boussinesq equations in semi-infinite domain, the wave period T was estimated as the time difference between two points where the surface elevation is 1% of the amplitude of the wave.

To prove the T determined in semi-infinite domain works for the study, different theoretical methods are compared in Fig. 5.7. It presents the comparison between the theoretical results for $\alpha = 0.05$, $a = 0.5$ and $b = 0.70$ and the experimental data up to the arrival of the reflected wave. Both the Boussinesq equations and the NSW equations in semi-infinite domain show good agreement with the experimental data before affected by the reflected wave. On the other hand, the linear analytic solution from unbounded domain is quite different from the data for wave amplitude, which means that nonlinear effects are not negligible in wave generation.

5.1.5 Wave periods of the waves generated using the bottom-tilting wave maker

Figure 5.8 ($\alpha = 0.04$), Figure 5.9 ($\alpha = 0.05$) and Figure 5.10 ($\alpha = 0.06$) show the wave period T in terms of the peak time T_a plotted as a function of a and b for both upward and downward motions, where the theoretical results are obtained by BE

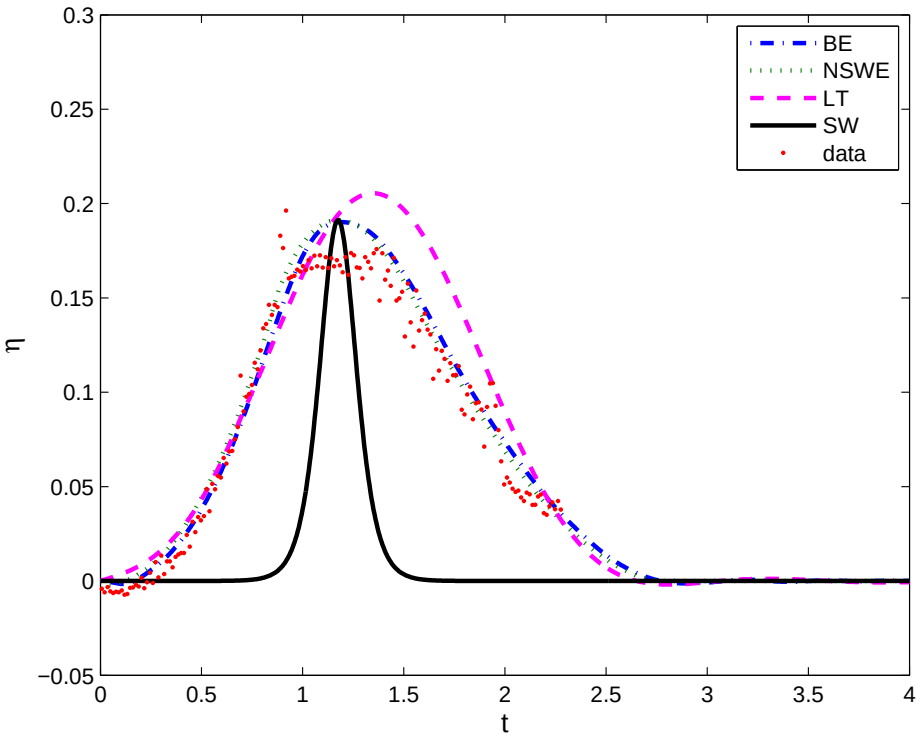

(a) upward motion

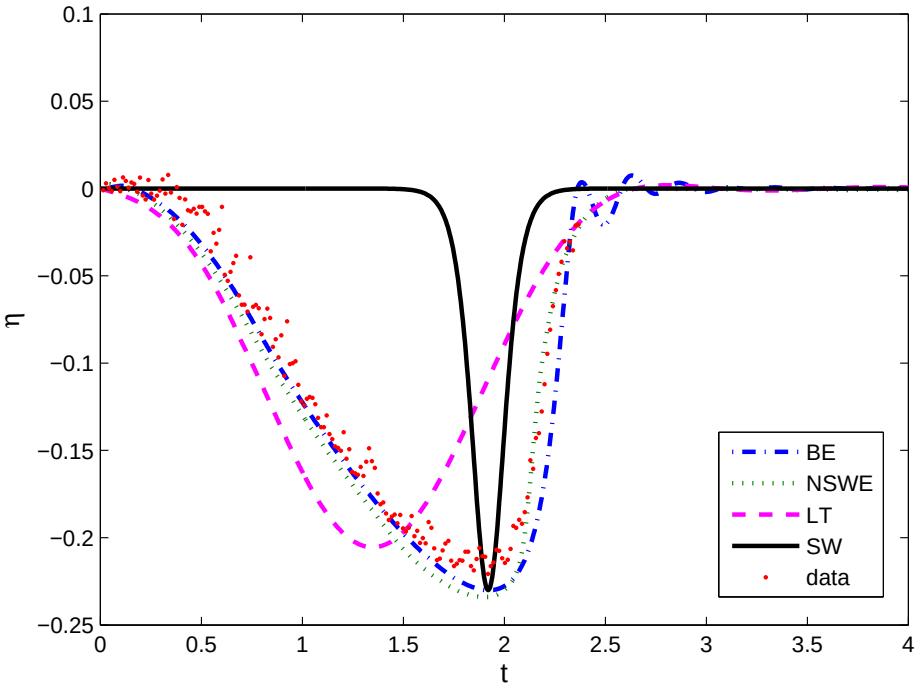

(b) downward motion

Figure 5.7: Theoretical results for waves in semi-infinite domain compared to experimental data: dash dotted line, results by BE; dotted line, results by N-SWE; dashed line, linear analytical results (LT); solid line, solitary wave solution Eq. (2.1) (SW); dot, experimental data.

system in wave tank domain. Similar to the observation of wave amplitude, the smallest waves for $\alpha = 0.05$ and $\alpha = 0.06$ are not included. It is observed that greater bottom motion duration b results in greater wave peak time T_a. However, dependence of T_a on a is different according to the direction of bottom movements. More specifically, while T_a decreases with a for upward motions, an opposite trend is found for downward motions. This interesting observation may be attributed to the nonlinear effects. For upward motions, water surface elevation increases from the beginning of the wave to the peak, and the local wave celerity also increases with the surface elevation. Therefore the wave form becomes squeezed to the left (wave peak appears earlier due to strong deformation) and this tendency would be stronger for higher amplitude waves. On the other hand, water surface elevation decreases from the beginning to the (negative) peak of the waves generated by the downward motions, and the wave form will be elongated at least up to the peak. It also can be used to explain the greater T_a found with greater α for upward motions but smaller α for downward motions owing to the decreasing a with α. Of course, this nonlinear effect cannot be expected from the linear analytic solution, which shows no functional dependence of T_a on a.

Wave periods estimated theoretically from the Boussinesq equations in semi-infinite domain are plotted against a and b in Fig. 5.11, Fig. 5.12 and Fig. 5.13 with the varying $\alpha = 0.04$, $\alpha = 0.05$ and $\alpha = 0.06$, respectively. As aforementioned, wave period is difficult to measure in the wave tank. Here, only theoretically estimated wave periods are investigated in terms of the generation parameters a and b. However, small-amplitude waves ($a = 0.1$) are more or less symmetric, and their wave periods can also be estimated using the peak time, that is $T = 2T_a$ (marked with star). Thus, only this one set of data with $a = 0.1$ is included in the figures. In comparison between the data with $a = 0.1$ and the theoretical results, the slightly bigger difference in the downwards motions implies that the negatives waves are easier to get deformed due to the nonlinearity than the positive waves even for the small motion with $a = 0.1$.

As in the case for the wave peak time, the wave period also increases with the bottom motion duration b. Dependence of the wave period on the bottom motion

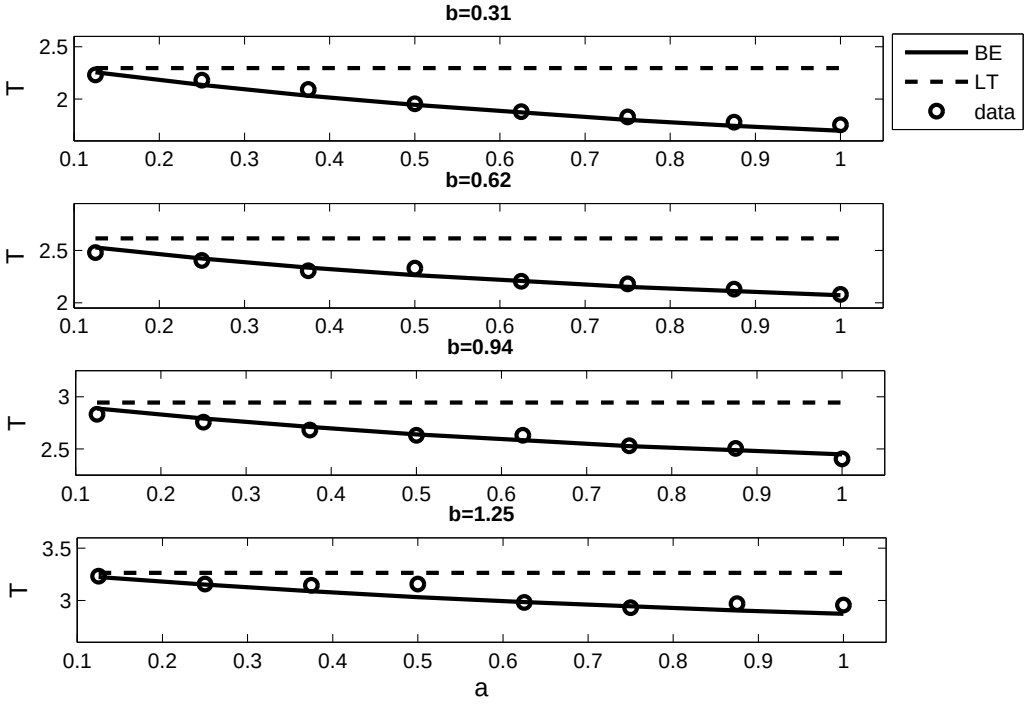

(b) Peak time T_a with varying upward bottom motions

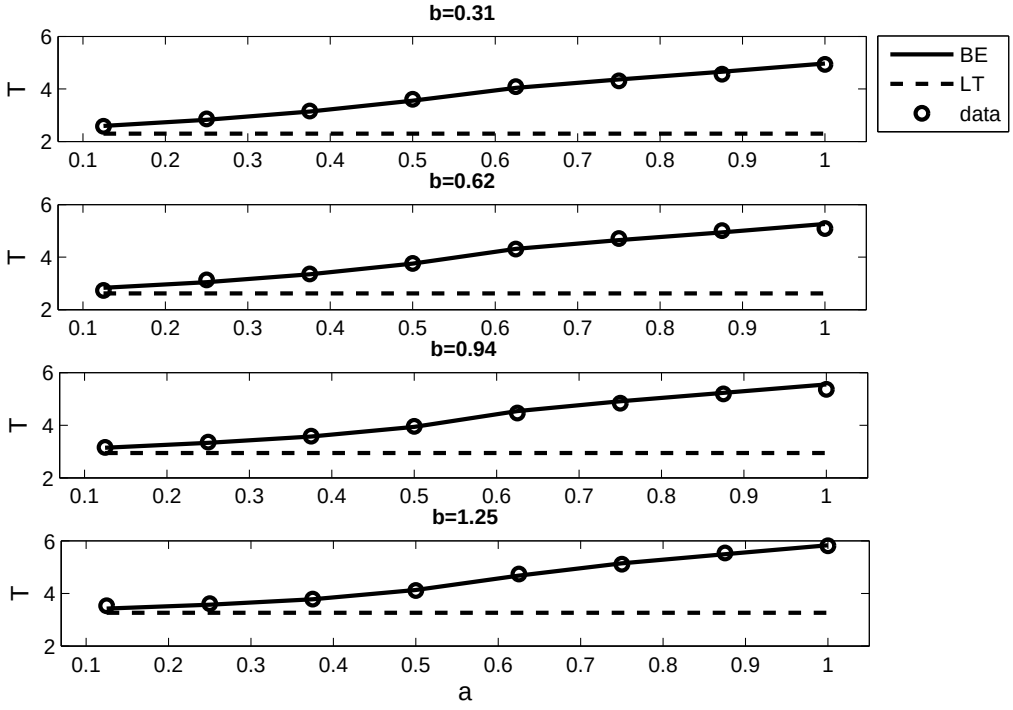

(b) Peak time T_a with varying downward bottom motions

Figure 5.8: Wave period ($T = 2T_a$) plotted against varying a and b with $\alpha = 0.04$: $\circ$, experimental measurements; solid line, numerical results by BE; dashed line, analytical results by LT.

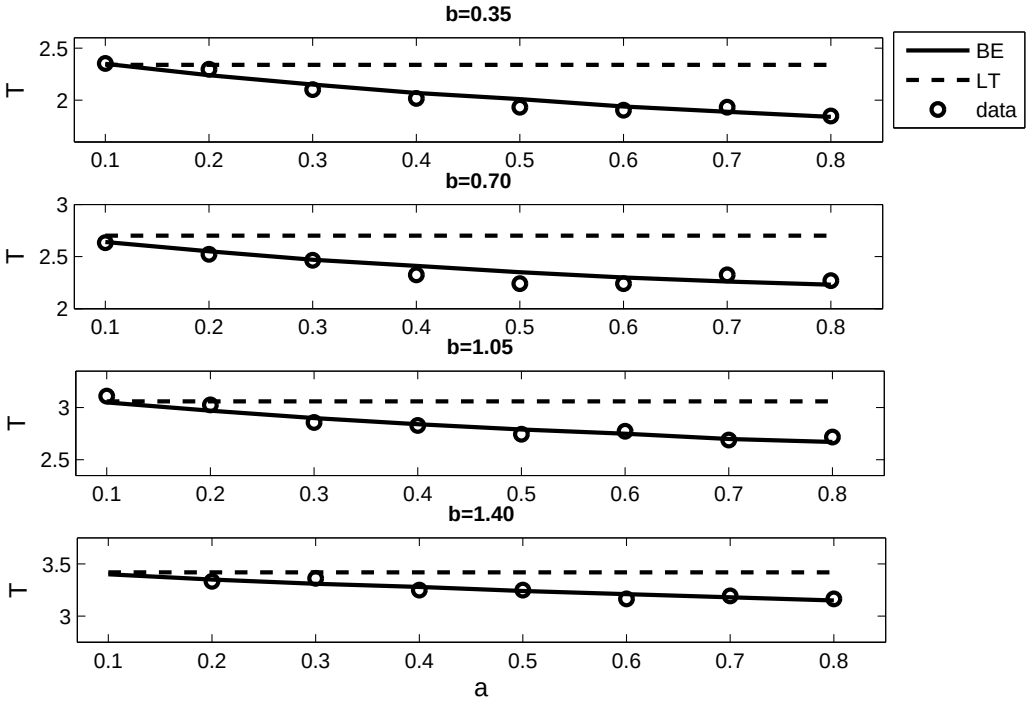

(b) Peak time T_a with upward varying bottom motions

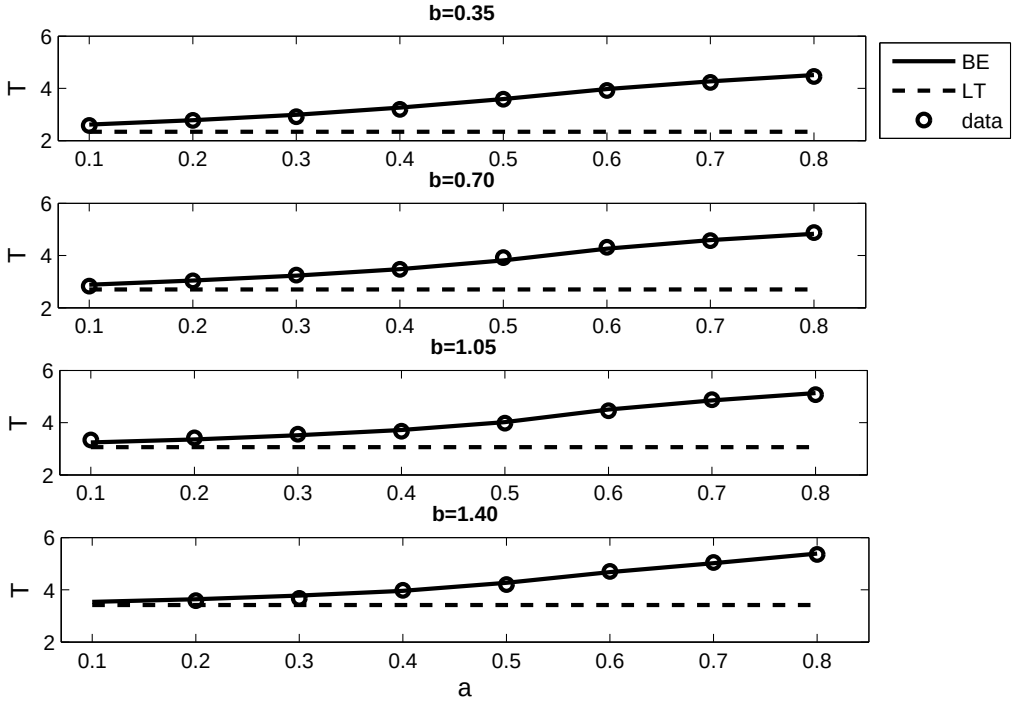

(b) Peak time T_a with downward varying bottom motions

Figure 5.9: Wave period ($T = 2T_a$) plotted against varying a and b with $\alpha = 0.05$: $\circ$, experimental measurements; solid line, numerical results by BE; dashed line, analytical results by LT.

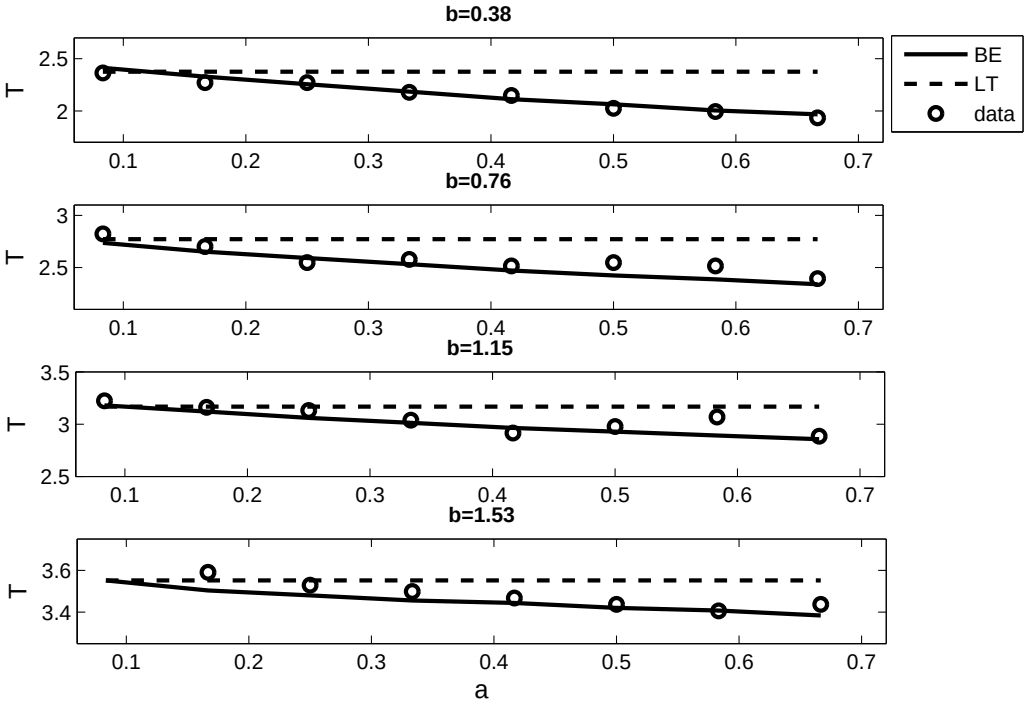

(b) Peak time T_a with upward varying bottom motions

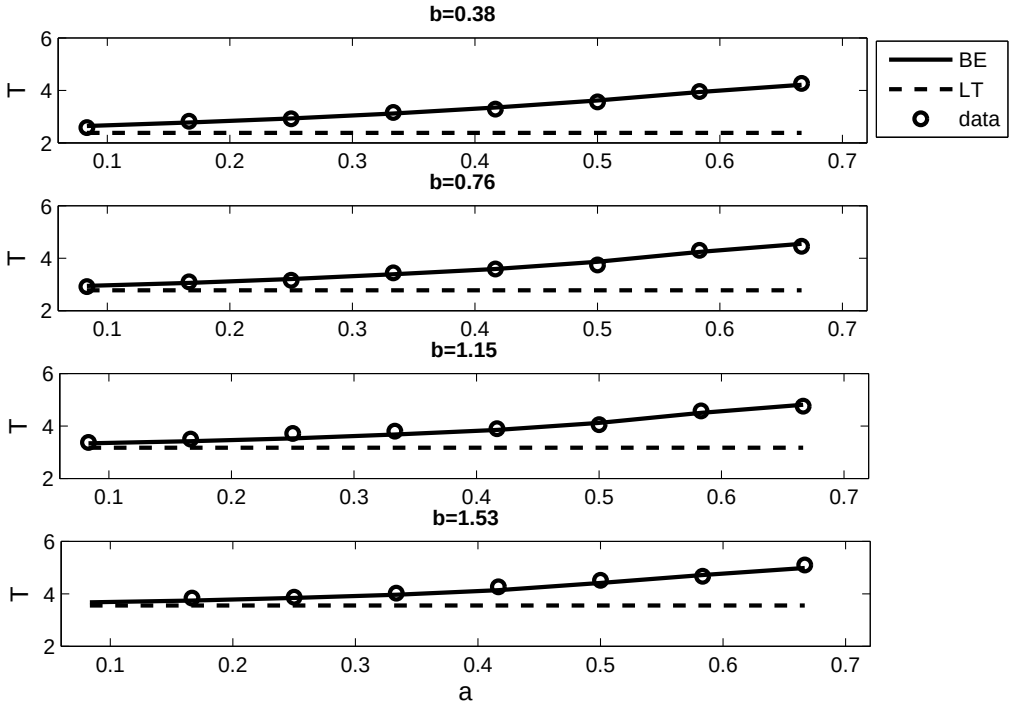

(b) Peak time T_a with downward varying bottom motions

Figure 5.10: Wave period ($T = 2T_a$) plotted against varying a and b with $\alpha = 0.06$: $\circ$, experimental measurements; solid line, numerical results by BE; dashed line, analytical results by LT.

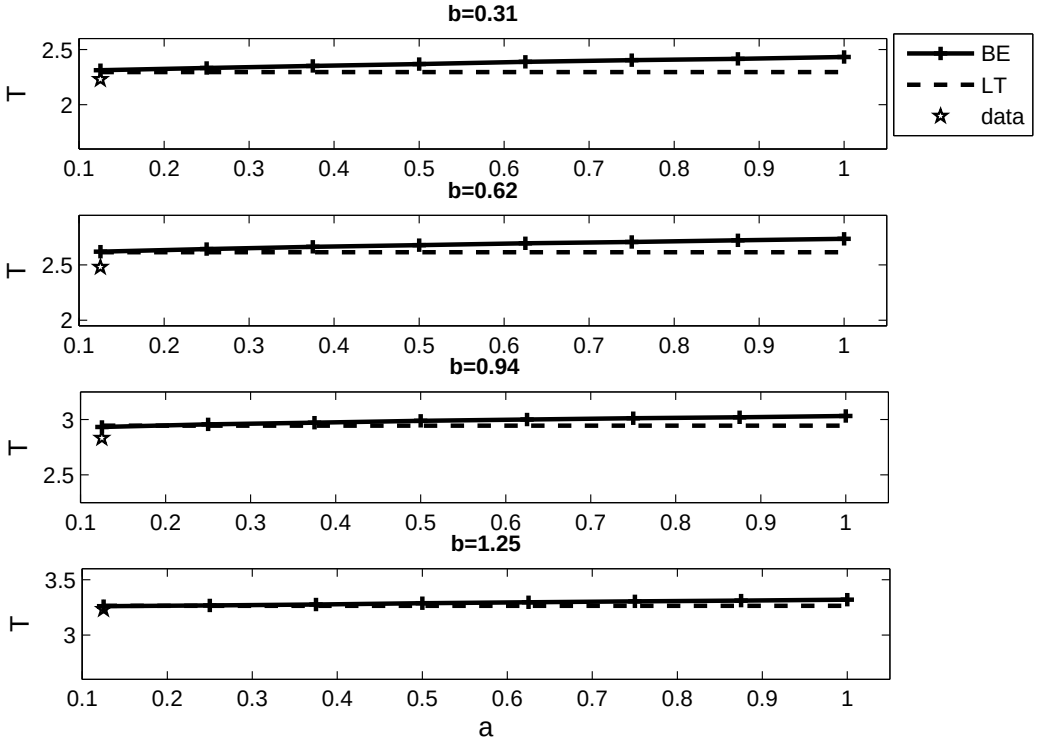

(a) Period T with varying a for upward motion

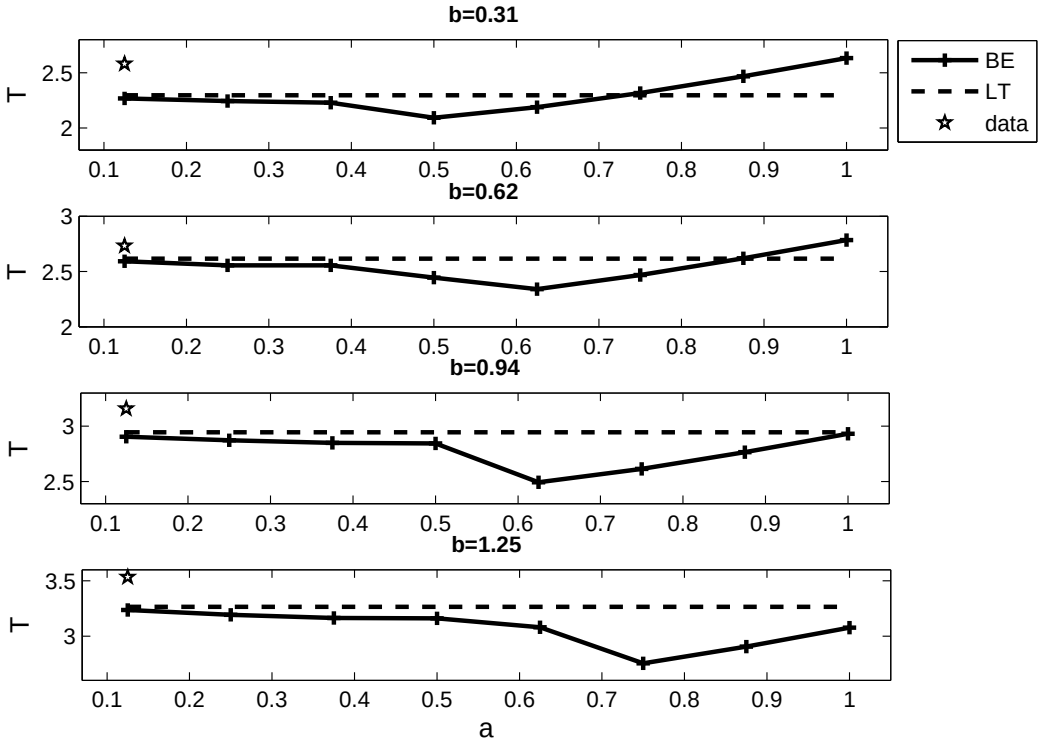

(b) Period T with varying a for downward motion

Figure 5.11: Wave period T plotted against varying a and b with $\alpha = 0.04$: $+$, numerical results by BE; dashed line, analytical results by LT; $\star$, experimental data.

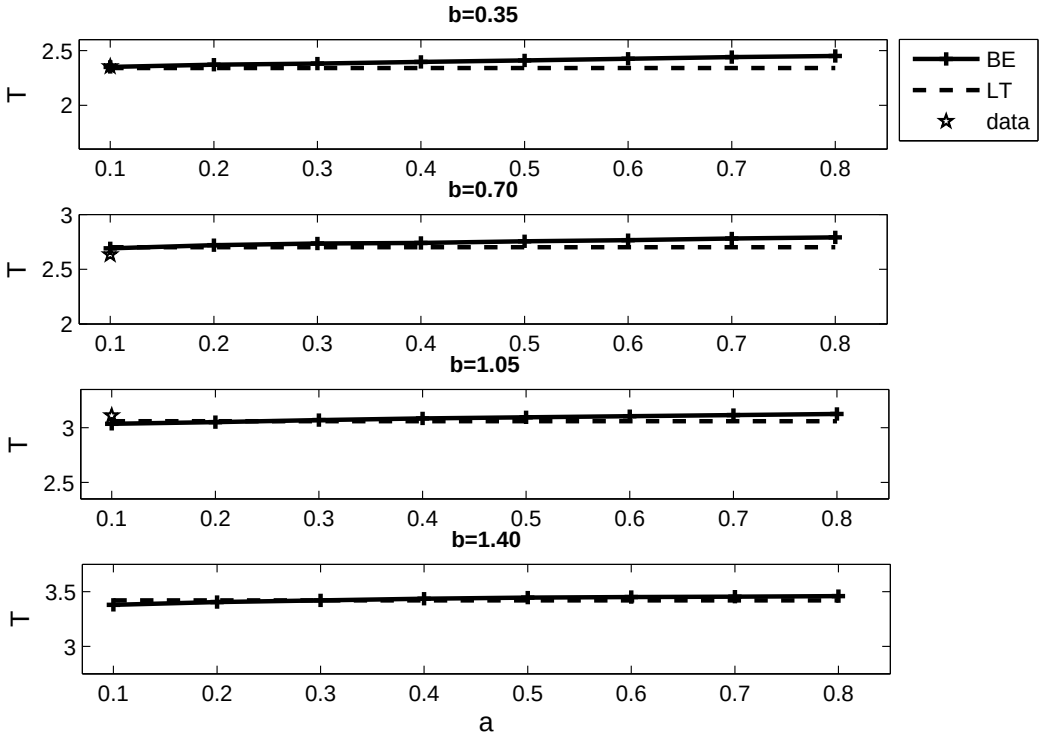

(a) Period T with varying a for upward motion

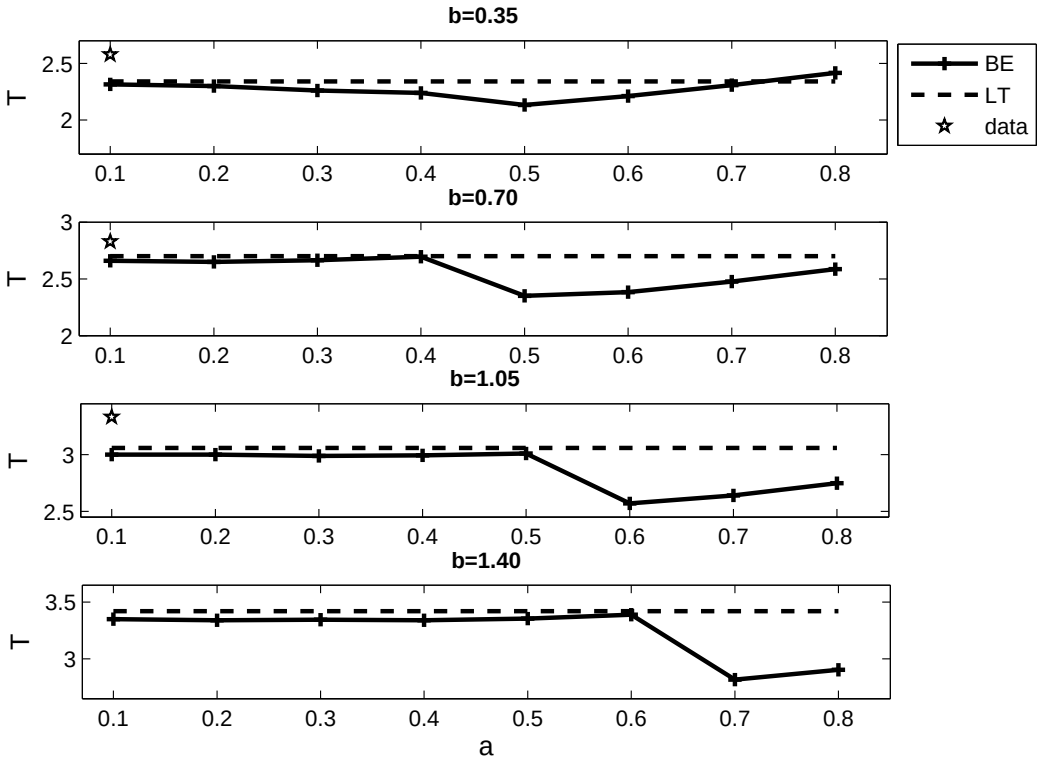

(b) Period T with varying a for downward motion

Figure 5.12: Wave period T plotted against varying a and b with $\alpha = 0.05$: $+$, numerical results by BE; dashed line, analytical results by LT; $\star$, experimental data.

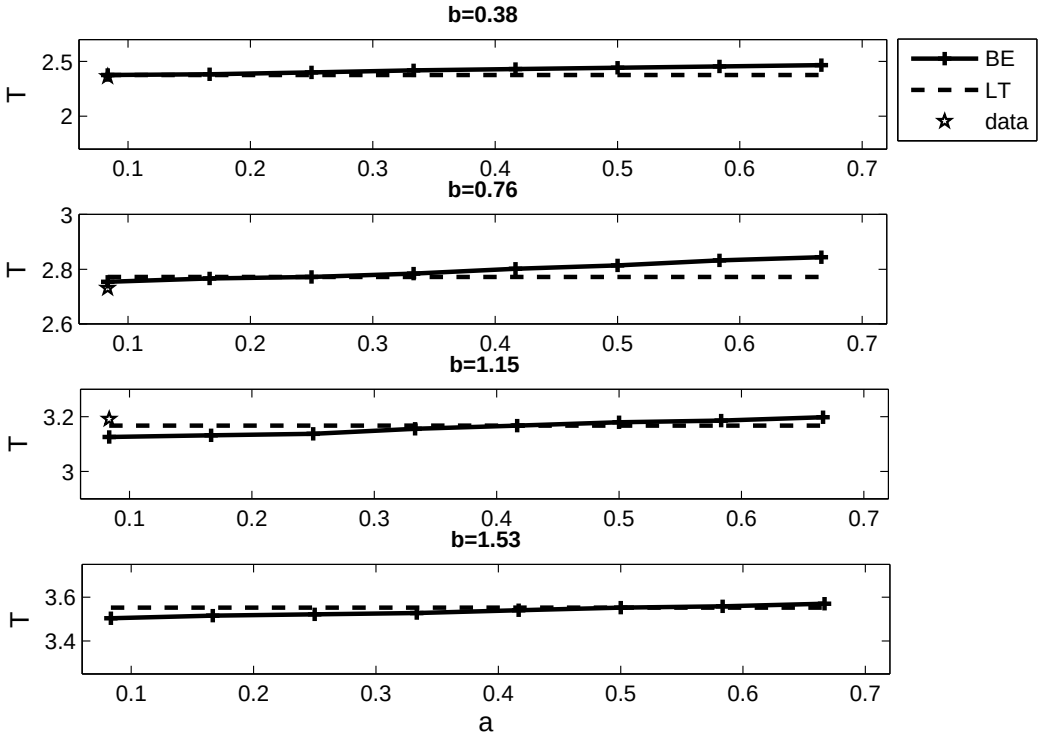

(a) Period T with varying a for upward motion

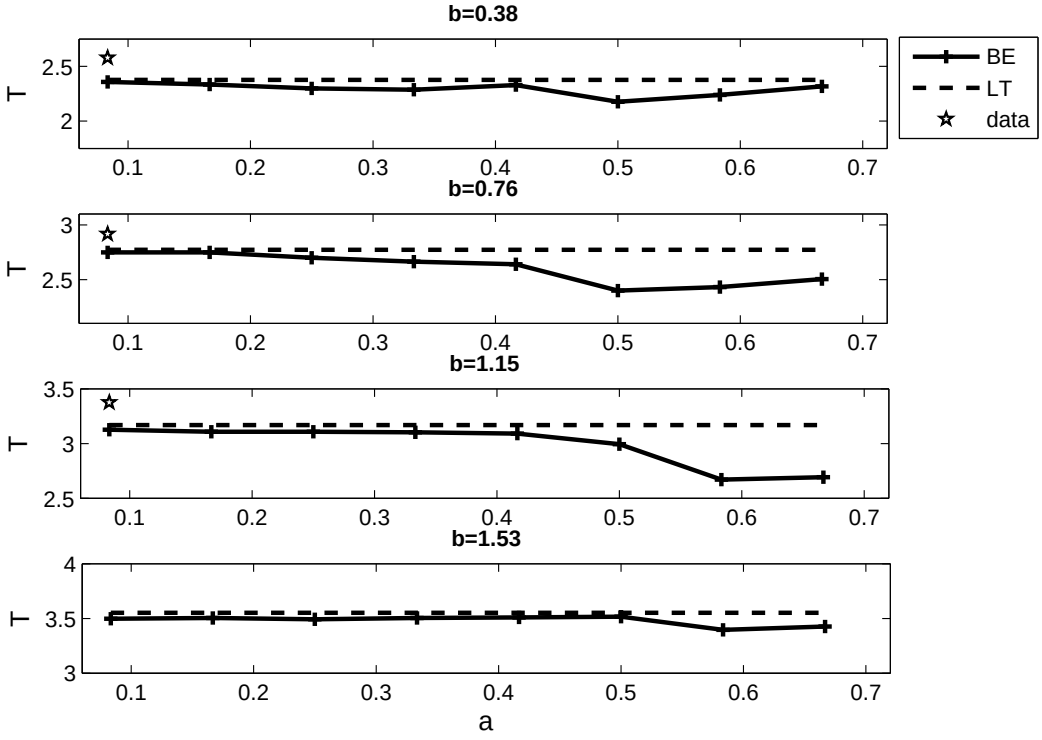

(b) Period T with varying a for downward motion

Figure 5.13: Wave period T plotted against varying a and b with $\alpha = 0.06$: $+$, numerical results by BE; dashed line, analytical results by LT; $\star$, experimental data.

amplitude is, however, much more complicated. Unlike the peak time, now it is observed that the wave period increases monotonously with the motion amplitude for the waves generated by the upward motions. This is only explained if the waves are skewed with long tails so that $T > 2T_a$, which is also due to nonlinearity. As the ranges of the axes of coordinates for wave period (Fig. 5.11 (a), Fig. 5.12 (a) and Fig. 5.13 (a)) are the same to those for wave peak time (Figure 5.8 (a), Figure 5.9 (a) and Figure 5.10 (a)) for upward motions, it is clearly seen that the influences of the motion amplitude appear to be much greater on wave peak time than wave period.

Wave periods of the waves generated by the downward motions show no longer monotonous dependence on a. For small motion amplitudes, the increase of peak time with a is almost cancelled due to the opposite trend of the tail. For larger amplitudes, dispersion manifests itself as disintegration of the wave form, which effectively reduces the wave period. After sudden decrease of the wave period, the nonlinear effects coming to play again, and the wave period starts to increase with increasing a just like the waves generated by the upward motions. The differences between the measurements of T_a and the theoretical results show that the skewness is stronger in waves generated by downward motions even when the motion is small. Therefore, the nonlinear effects caused by increasing motion amplitude contribute more on the skewness of the wave form for both positive and negative waves.

Due to the rather complex response of the wave periods to the motion amplitudes, a simple functional description of T with respect to a and b could not be found.

5.1.6 Further discussion

So far, characteristics of the waves generated by the bottom-tilting wave maker, namely the wave amplitude and the wave period, have been discussed in terms of the parameters (a and b) of simple upward and downward bottom motions.

In this section, the new wave maker is further investigated. First of all, the waves generated in the new wave tank are compared to the relevant solitary waves, demonstrating that the new wave maker can indeed generate waves that are longer than the solitary waves in terms of the effective wavelength. Then the bottom-tilting-generated wave is compared to the field data of 2011 Japan Tohoku tsunami. Finally, effects of the length of the tilting bottom is also discussed.

Fig. 5.14 illustrates the comparison of the ratio L_w/L_s of wavelength between the solitary waves and the bottom-tilting generated waves for $\alpha = 0.05$, where L_w is obtained from the BE system in semi-infinite domain and L_s from Eq. (2.1). The ratio L_w/L_s is always greater than 1 and up to 5.5, demonstrating that the bottom-tilting wave maker can generate waves longer than the effective wavelength of solitary waves. In fact, the maximum L_w/L_s among all the observed waves can be 7.23 which has $a = 1, b = 1.25$ and $\alpha = 0.04$. Also notice that the L_w/L_s grows with mostly increasing motion amplitude and with increasing motion duration, except some sudden drop for downward motion. The variations for downward motion mostly are caused owing to the dispersion discussed in Section 5.1.5 for the wave periods obtained in semi-infinite domain. The dependence of wave length (wave period) on the bottom motion is complicated. Although the dispersion will reduce the wave length (wave period) for big-amplitude waves, wave length (wave period) will be back to increase when the nonlinearity grows later.

The 2011 Japan Tohoku tsunami record shown in Fig. 5.15 (a) by the solid curve was obtained on a gentle slope of 1/42 (if the bathymetry is simplified as a plane beach) with a water depth of 204 m (Chan and Liu, 2012). The amplitude of the leading wave was 6.6 m and the wave period was 1500 s, resulting in the normalised wave amplitude $A = 0.032$ based on the Froude scaling. The upward bottom motion in the new wave maker with $a = 0.1$ and $b = 1.40$ just satisfies $A = 0.032$, and the result is compared to the field data (solid) as shown in Fig. 5.15 (a) by the dash-dotted curve. The corresponding wave period of the bottom-tilting-generated wave is still shorter than the field data, albeit much better than the solitary wave (dotted curve). However, closer inspection of the

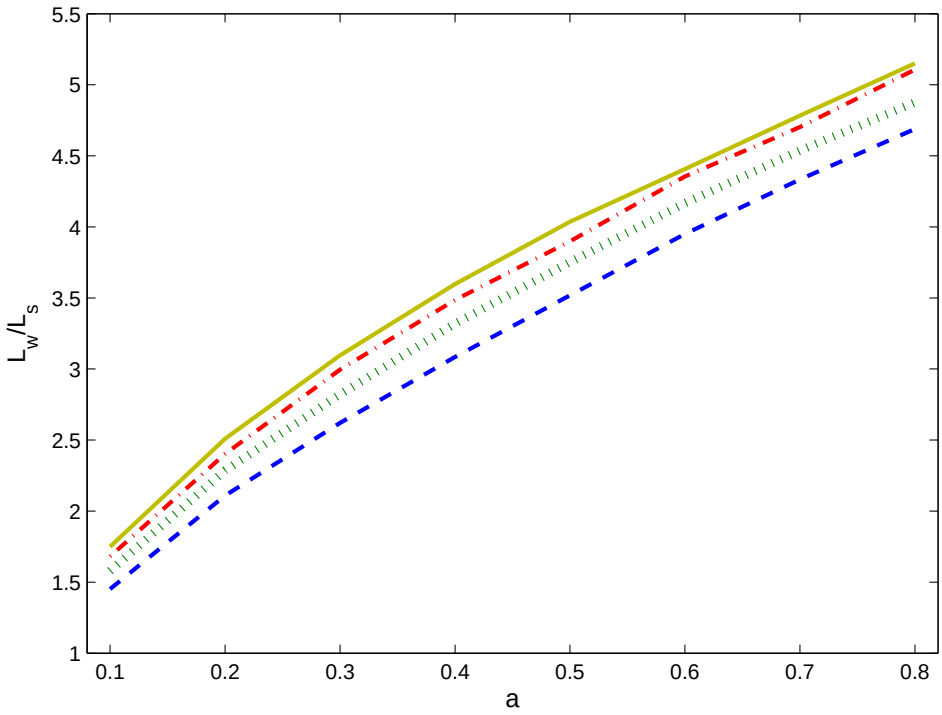

(a) upward motion

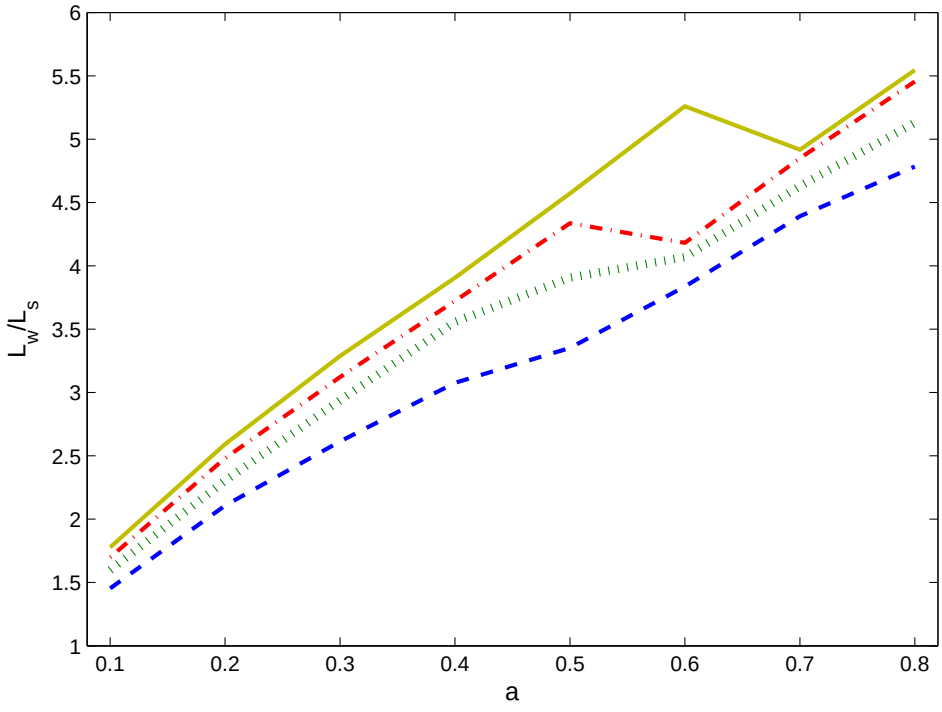

(b) downward motion

Figure 5.14: Plots of the ratio of L_w/L_s with varying a and b for upward motions and downward motions: dashed line, $b = 0.35$; dotted line, $b = 0.70$; dash dotted line, $b = 1.05$; solid line, $b = 1.40$.

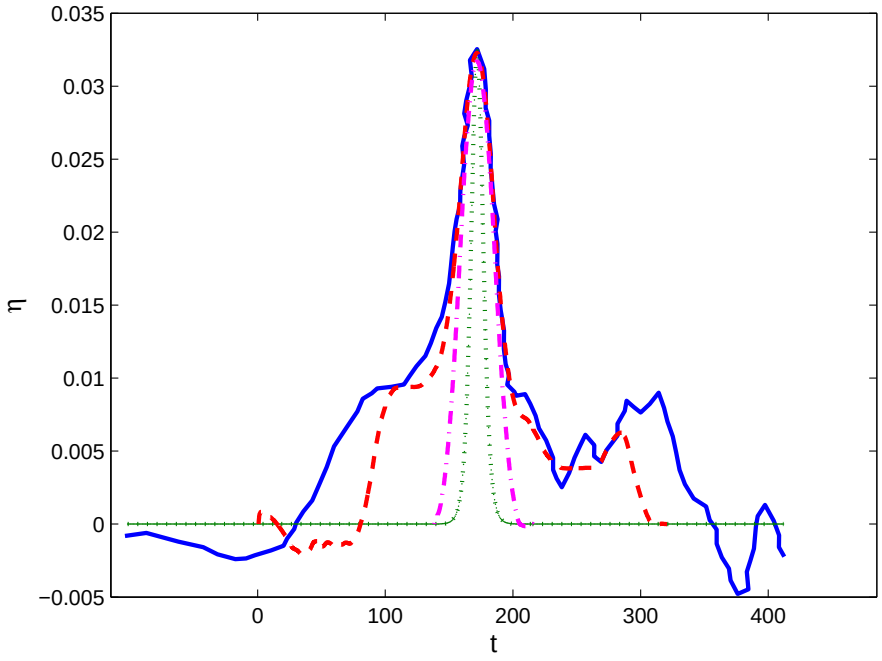

(a) Comparison between field data and fitted waves: solid line, field data; dashed line, fitted wave by sophisticated bottom motion shown in (b) below; dash dotted line, fitted wave by simple upward motion; dotted line, fitted solitary wave .

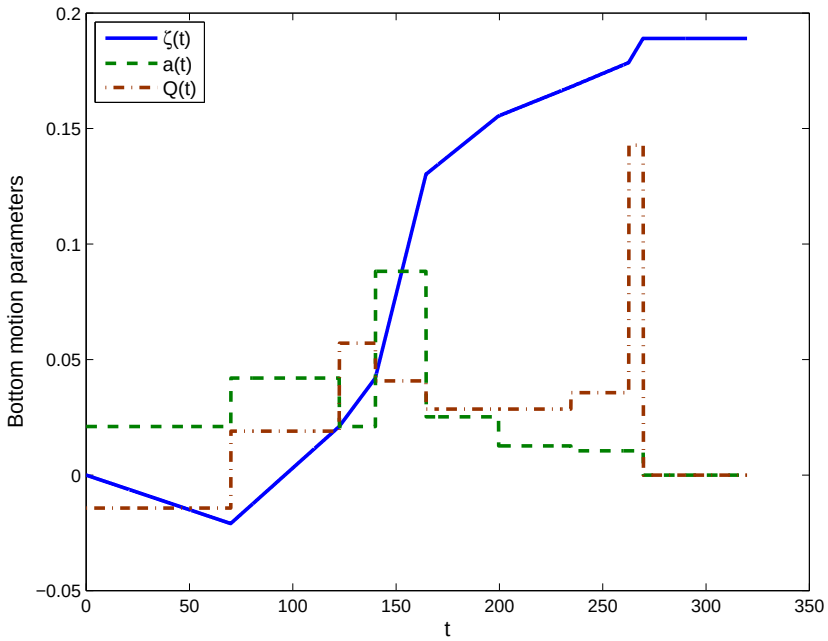

(b) Bottom motion parameters $\zeta(x=0,t)$ (solid line), $a(t)$ (dashed line) and $Q(t)$ (dash dotted line) of the fitted wave by sophisticated bottom motion

Figure 5.15: Comparison between field data at Iwate South from Japan Tohoku tsunami in 2011 (Fujii et al. (2011)), fitted bottom-tilting-generated waves and a fitted solitary wave.

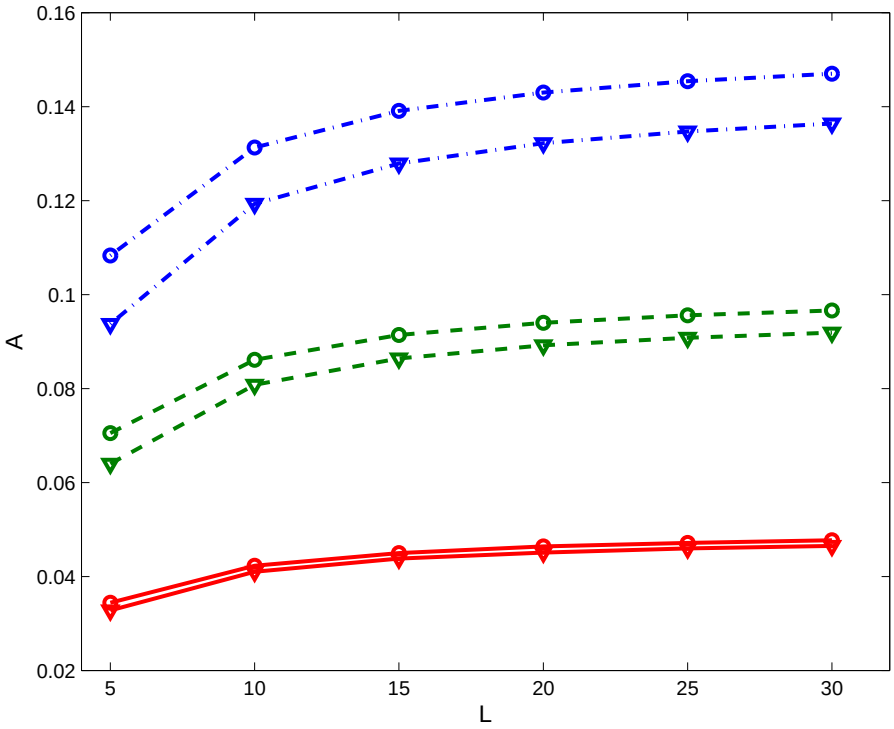

(a) wave amplitude

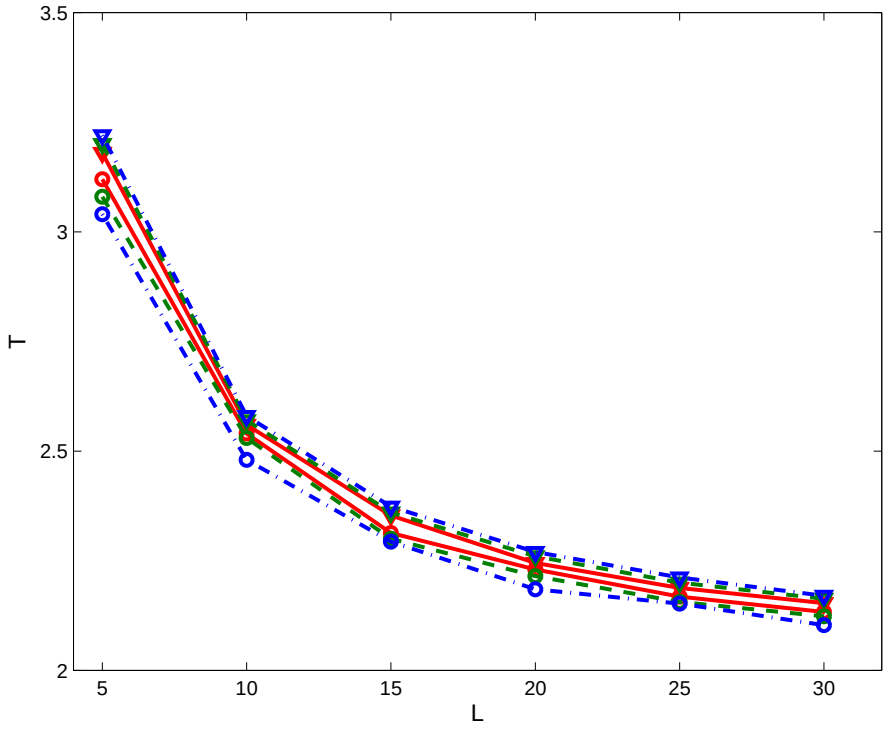

(b) wave period

Figure 5.16: Comparison of wave characteristics with varying moving bottom length: $\bigtriangledown$, upward motion; $\circ$, downward motion; solid line, $a = 0.1$; dashed line, $a = 0.2$; dash dotted line, $a = 0.3$.

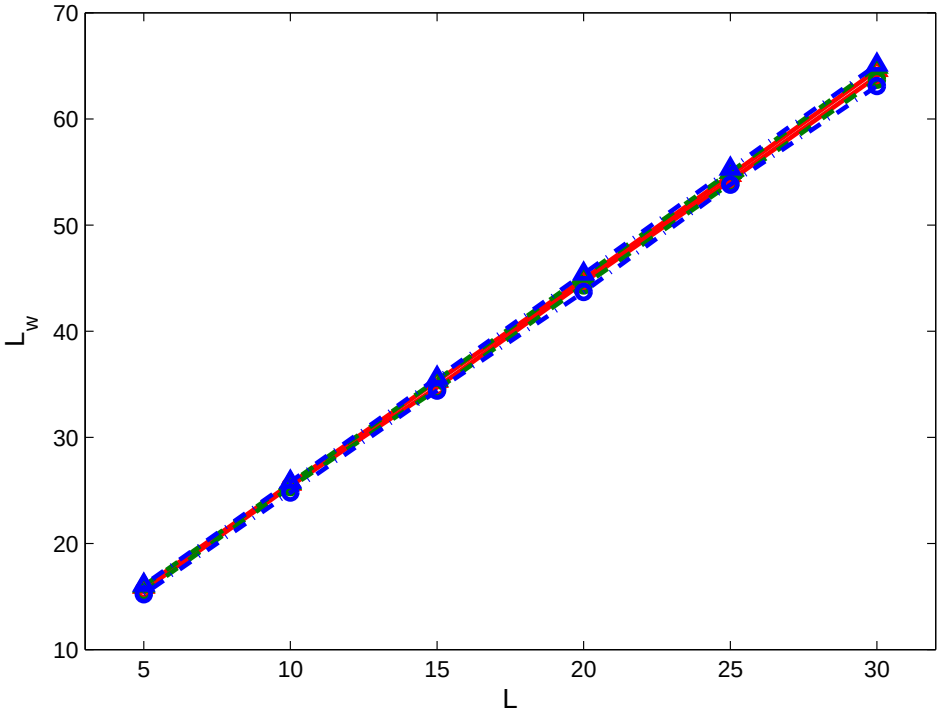

Figure 5.17: Comparison of wavelength with varying moving bottom length: $\bigtriangledown$, upward motion; $\circ$, downward motion; solid line, $a = 0.1$; dashed line, $a = 0.2$; dash dotted line, $a = 0.3$.

figure shows that the new wave agrees well with the field data near the peak of the tsunami record. It is an encouraging result considering that only a simple upward motion was used, which suggests that more sophisticated operation of the tilting bottom should be able to achieve better agreement with the field data. Theoretically, if the wave is allowed to propagate for, by applying the bottom motion displacement $\zeta(x = 0, t)$ (solid) as shown in Fig. 5.15 (b), the new wave maker is able to generate a wave that is very similar to the field data as shown in Fig. 5.15 (a) by the dashed curve based on the BE system in a semi-domain. Furthermore, the time histories of the motion amplitude a and the relative motion speed Q (reciprocal of b) determined by Eq. (3.30) are described in figure 5.15 (b) as well. However, the deviation at the beginning and the end of the wave profile requires further adjustment to enlarge the wave period at the two parts accordingly, for example, further increasing the motion duration.

The wavelengths of the bottom-tilting-generated waves are mainly limited by

the length of the tilting bottom. Previously, in Fig. 4.2, it has been shown that the length of the tilting bottom relative to the water depth plays an important role in determining the length characteristics of the resulting waves. In Fig. 5.16, the dependence of wave amplitude and wave period on the moving bottom length is plotted based on the BE system in a semi-domain. It can be seen that increasing length of the moving bottom leads to growing wave amplitude but decreasing (dimensionless) period for both kinds of bottom motions. The decreasing period is caused by the normalisation of time lies on the bottom length according to Eq. 5.2. With respect to the wavelength L_w, the dependence of wavelength on the length of the moving bottom is shown in Fig. 5.17. It indicates that longer moving bottom results in longer wave, which also verifies the results in Fig. 5.6 that increasing V_w by longer L_w reduces the wave amplitude while longer waves can be obtained.

5.2 Wave run-up investigation

Wave behaviours such as the time history and the wave shape during run-up on a plane beach have been observed experimentally based on the set-up shown in Fig. 4.4 within the range of the parameters in Table 5.2. To facilitate the experimental investigation, a numerical model based on the NSW equations was used to explore the features of wave run-up and the new wave maker with the domain same to the wave tank. In the frame of the coordinates shown in Fig. 3.3, $x = 0$ is the initial shoreline and $x = -1/\gamma$ is the toe of the slope. As previously mentioned, the fixed seaward boundary is at $x = -\Gamma$ and the shoreward boundary is moving with the wave. The focus of this section is the dependence of maximum run-up height on wave shape, motion characteristics, water depth and beach slope.

5.2.1 Long wave generation

In the previous section, it has been proven that the new wave maker can generate very long waves. These long waves were used as the incident waves of the long wave run-up observed. In order to investigate simple leading-elevation and leading-depression waves, upward form and downward form of motions are considered but simplified as motions with constant velocity. Therefore, the bottom motion displacement ζ within $-\Gamma \leq x \leq -1/\gamma$ is given by

$$\zeta(x,t) = -at(x + 1/\gamma)/bL, \quad 0 \leq t \leq b \tag{5.9}$$

for upward motion, or

$$\zeta(x,t) = \begin{cases} at(x + 1/\gamma)/b_1 L, & 0 \leq t \leq b_1 \\ -a(t - b_1)(x + 1/\gamma)/(b_2 - b_1)L, & b_1 < t \leq b_2 \end{cases} \tag{5.10}$$

for down-upward motion with the relation $L = \Gamma - 1/\gamma$. For upward motion, the moving bottom goes up from the initial position $z = -h_0 - a$ to ensure the tank bottom flat after the displacement. For down-upward motion, the motion amplitudes of the upward part and the downward part are determined the same for simplicity, and the moving bottom starts from $z = -h_0$. To further simplify the problem, $b_2 = 2b_1 = 2b$ is assumed to make the constant velocity the same for the upward part and the downward part. The down-upward motions are expected to generate leading-depression waves which is motivated by some field observations (Tadepalli and Synolakis, 1994; Borthwick et al., 2006) that the shorelines first recede before run-up when tsunamis approach the shore. The simple downward motion is not considered here since it is too difficult to capture the shoreline movement.

To observe the incident waves, the experimental results of the surface elevation time-histories at the hinge were compared to the numerical results by the NSW equations in consideration of the reflection. Still, it is reasonable to study the early period of the free surface elevation at the hinge as part of the incident waves

since the reflection of the tank-long waves will not arrive the hinge before the wave peak passes the hinge. Fig. 5.18 shows the comparison for the cases with $\gamma = 1/20$, $\alpha = 0.03$ and $a = 0.67$ for an early period of time. Good agreement between the experimental and the theoretical results validates the numerical model based on the NSWE system with wave tank-long domain. In addition, dispersion becomes less important, which proves that the NSW equations are suitable to be employed. Note that uncertainty ($\pm$ 0.017 non-dimensionally for $\alpha = 0.03$) of the wave gauge resulted in some scattering of the experimental data, in particular in small-amplitude waves.

In general, motion type of the generation source plays an important role in determining the wave form of the resulting waves. From Fig. 5.18, it can be seen that upward motions lead to leading-elevation waves while leading-depression waves with elevated waves following the depression are generated by down-upward motions. However, wave form of the incident waves can change during the run-up process as the waves become more and more asymmetric with sharply decreasing water depth on the plane slope and the rapidly growing nonlinearity. Nonlinear effects can also be found from the wave profile at the hinge. As mentioned earlier, greater motion amplitude increases the nonlinear effects and deforms the waves. When a is fixed, the resulting waves deform with varying b as shown in Fig. 5.18.

The numerical results based on the Boussinesq equations in the semi-infinite tank were used to further describe the incident waves at the hinge in addition to the experimental observations. Fig. 5.19 shows the numerical results of the incident waves in Fig. 5.18 accordingly and two more waves with $b = 0.81$ in addition. It is reasonable to consider weak dispersion included in the Boussinesq equations in the wave generation due to the small dispersion found in the peak of the leading-depression waves from the measurement, in particular the ones at $b = 0.27$ and $b = 0.54$ in both Fig. 5.18 (b) and Fig. 5.19 (b). It appears that greater bottom motions with higher speed lead to early disintegration, especially for down-upward motions.

According to the wave profiles in Fig. 5.19, the wave behaviour with varying b

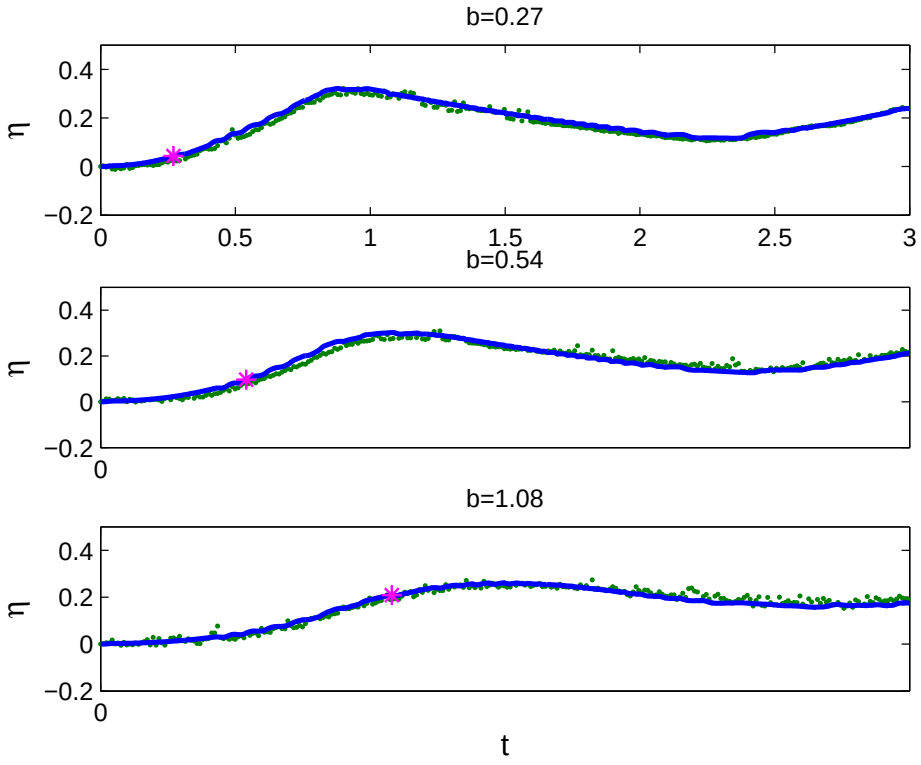

(a) upward motion

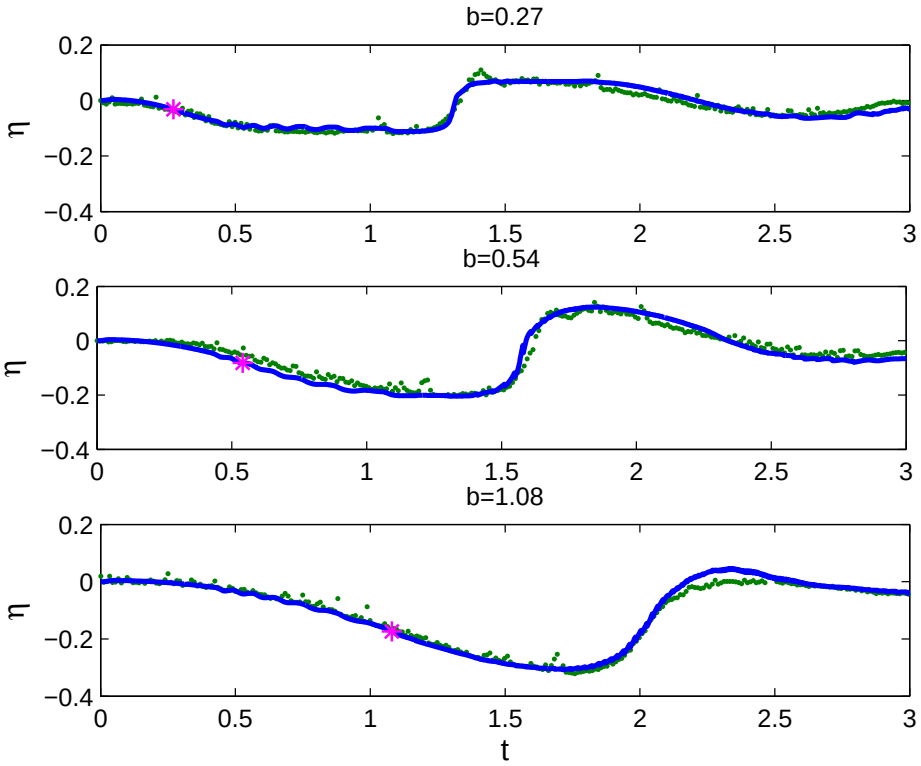

(b) down-upward motion

Figure 5.18: Comparison of the free surface elevation at the hinge with $\gamma = 1/20$, $a = 0.67$ and $\alpha = 0.03$: dot, experimental data; solid line, numerical results; asterisk, time when the bottom motion stops.

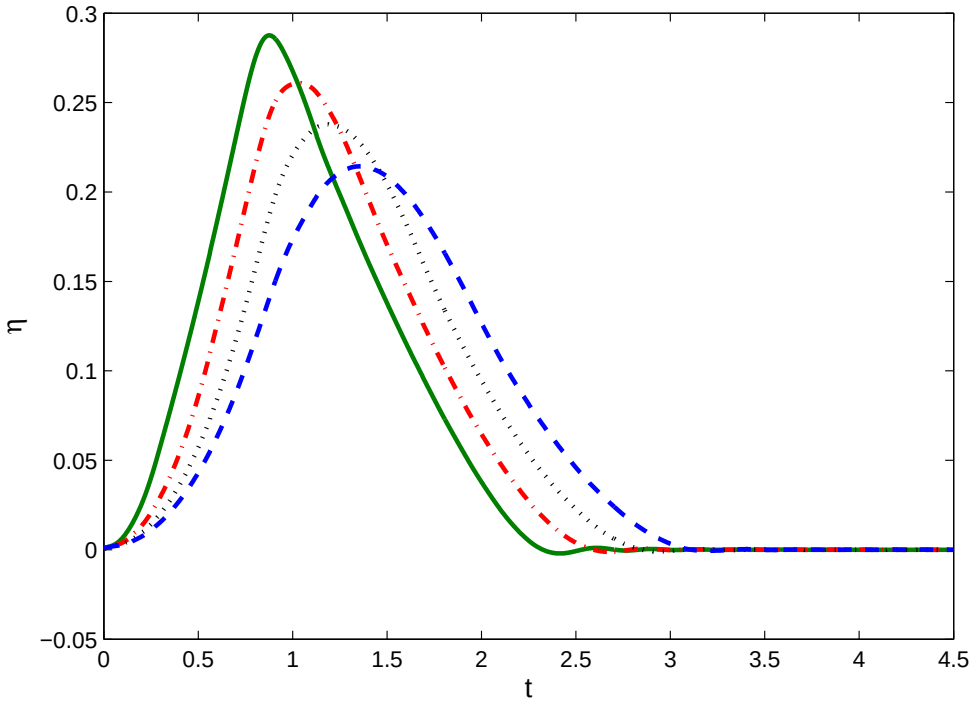

(a) upward motion

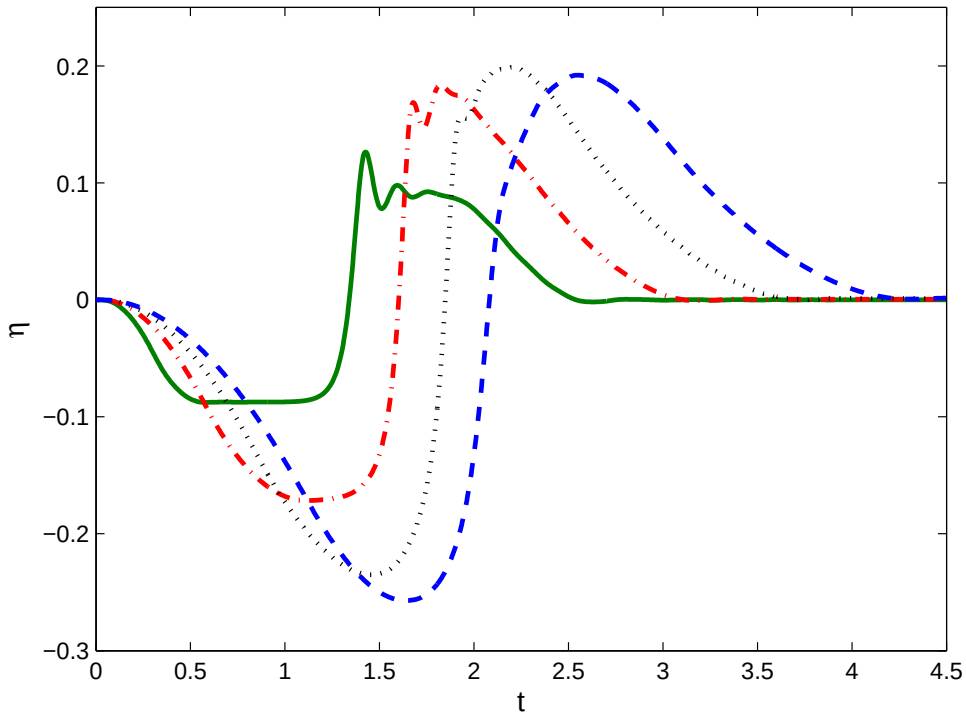

(b) down-upward motion

Figure 5.19: Comparison of the incident waves by upward or down-upward motion at the hinge with $\gamma = 1/20$, $a = 0.67$ and $\alpha = 0.03$: solid line, $b = 0.27$; dash-dotted line, $b = 0.54$; dotted line, $b = 0.81$; dashed line, $b = 1.08$.

in Fig. 5.18 can be well explained. For the leading-elevation waves, the wave front (accelerating phase) becomes steeper with smaller b. It can be caused by smaller motion duration which drives more water particles to move during a same period of time and makes the water particles easy to get squeezed at wave front (earlier peak time). Meanwhile, greater motion duration time elongates the accelerating wave profile. Then, due to the fact that the volume of displaced water is fixed by a fixed a, wave amplitude becomes smaller while wave period becomes greater with increasing b.

However, the behaviour of the waves generated by down-upward motion become more complicated. It cannot be ignored that the water in the beach area will flow to the lowered moving bottom if the downward motion is slow enough. Then, more water will be lifted up by the subsequent upward motion, which is clearly seen in Fig. 5.19 (b). Thus, the increase in the volume of the displaced water results in the growth of the wave height and the wave period. It can also induce steeper accelerating phase (nadir to peak) once the squeeze caused by the increased volume of the displaced water becomes more important than the elongation of the wave period caused by big motion duration time which increases the wave peak time T_a, e.g., the wave profile at $b = 0.54$. This issue will be further discussed later.

In conclusion, the incident waves in Fig. 5.19 verify the surface elevation time history in Fig. 5.18 and the fact that waves generated by higher-speed bottom motions have greater wave heights and steeper wave fronts when the same amount of water is displaced. On the other hand, the characteristics of the generated waves are difficult to compare monotonously when the amount of displaced water is varying.

5.2.2 Run-up process

The run-up process can be estimated by the numerical model based on the NSWE system with a tank-long domain or the analytical solution (3.71) for linear non-

breaking waves. For small amplitude waves, the analytical solutions by the linear wave theory (3.37) give a quick estimation of the incident waves. The analytical solutions can also be used to verify the numerical modelling. Fig. 5.20 presents the run-up process of small amplitude waves generated by an upward motion in (a) or a down-upward motion in (b) with $\alpha = 0.03$, $a = 0.17$ and $b = 0.54$ at a slope of $\gamma = 1/20$ compared between experimental and theoretical results.

Fig. 5.20 (i) displays the incident wave profile, where the analytical solution agrees well with the numerical result since the nonlinearity is not important here. However, it can be observed that the weak nonlinear effects still lead to a slight asymmetry in the numerical results. In (ii), the numerical results fit the experimental data better than the analytical solution, but both give reasonable prediction of the time history of the free surface elevation at the hinge. Note that the slight oscillations in the numerical results are caused by the moving domain which makes it difficult to locate the hinge exactly as the adjacent grid closest to the hinge location is used but varies. Obviously, the generated long wave is affected by the reflection at the later period of time in comparison with (i). Nevertheless, the early period of the time history shows main characteristics of the incident waves. (iii) demonstrates the comparison of the time history of the run-up height between the two theoretical methods. In order to compare with the analytical solutions, the friction term is not considered in the numerical model here. The linear solution in (i) is used as the input for the analytical solution of the run-up height (3.71). The difference between the theoretical results can be caused by the neglecting nonlinearity. The theoretical results become much greater than the measurements owing to the simplification of the theoretical methods, for example, the neglecting bottom friction, also the surface tension discussed in the section of scale effects. Note that the shoreline motion for down-upward motion cannot be tracked entirely as it gets vague in wet places. It can be seen from (iii) that the leading-elevation wave uprushes the beach directly, while the leading-depression wave first draws back then advances up the beach as observed by some field investigations.

For high-amplitude waves, the analytical solutions are unable to estimate the

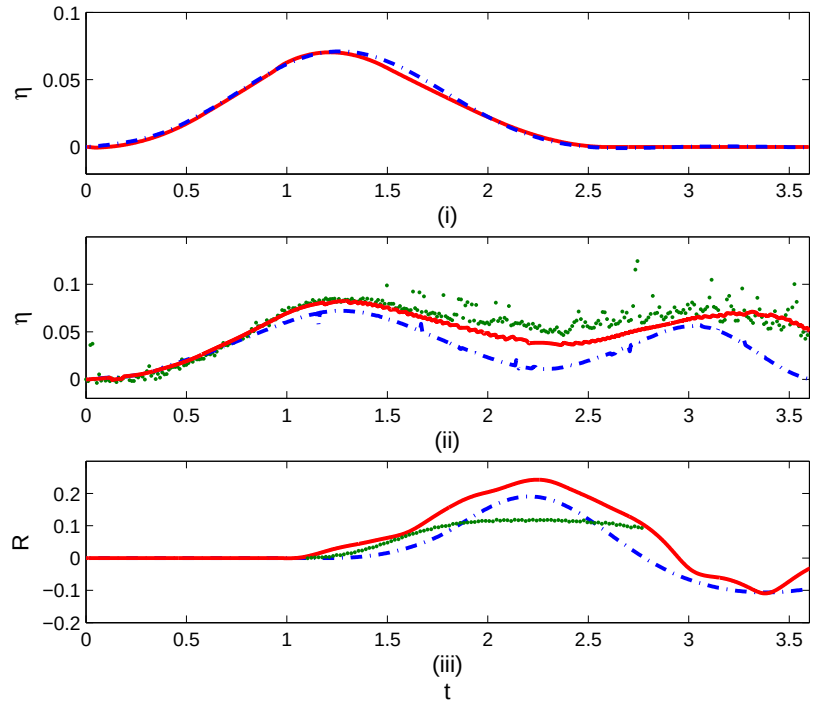

(a) upward motion

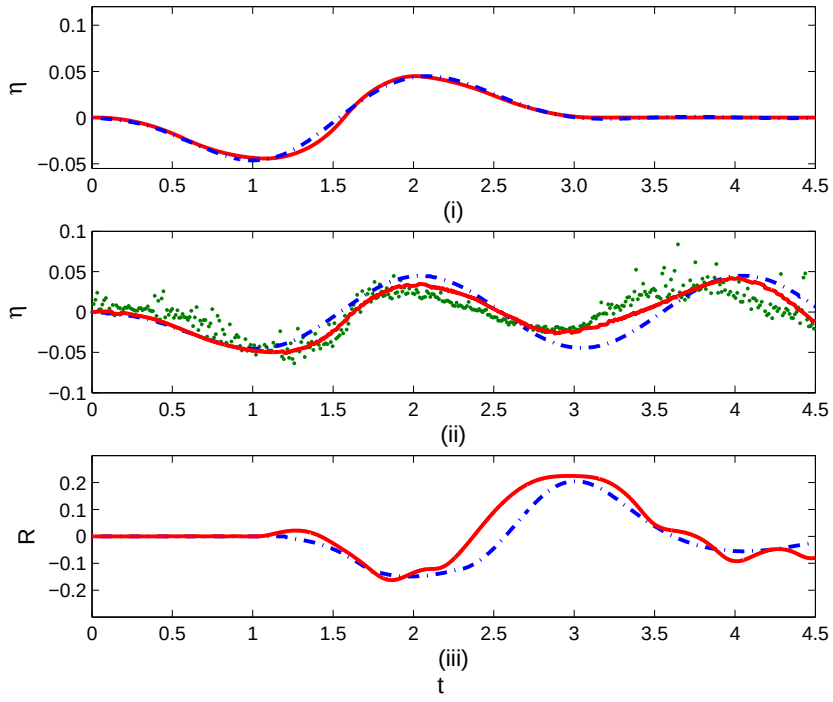

(b) down-upward motion

Figure 5.20: Run-up process between the theoretical results and the measurements with $\alpha = 0.03$, $a = 0.17$ and $b = 0.54$ at slope of 1/20: (i) Incident wave time history; (ii) Free surface elevation time history at the hinge; (iii) Run-up height time history (Solid line, dash-dot line and dot denote numerical results, analytical solutions and measurements, respectively).

run-up height time history accurately. On the other hand, the results can be clearly investigated from the numerical modelling based on the NSWE system. Fig. 5.21 and Fig. 5.22 show the numerical simulation of the run-up process of the waves shown in Fig. 5.19 with $b = 0.54$. Limited by the ability of the camera, the trajectory of the shoreline can only be recorded partly in particular at which close to the maximum run-up height location, which is indicated as asterisk in Fig. 5.21 and Fig. 5.22, respectively. The first columns of the two figures demonstrate how the waves are generated by the corresponding bottom motion. The leading elevation is created by the upward motion, while the downward component of the motion forms the leading depression. After the motion, the bottom remains parallel to the ground, which can be seen in the second columns. The shoreline is moving along with the wave run-up or run-down. The maximum run-up height is shown in the third one of the second column for the two motions. As the friction term was not considered here, the theoretical run-up height is greater than the measurements. It also verifies that water on the plane beach becomes very shallow during wave run-up. In the meanwhile, the influence of the bottom friction can be significant.

When the friction term is considered, the numerical results of the run-up height will be reduced and closer to the experimental data, as shown in Fig. 5.23 which corresponds to the cases in Fig. 5.21 and Fig. 5.22 for example. The numerical model simulates the maximum run-up height reasonably well, but the time history is retarded. The bottom friction term underestimates the acceleration of the shoreline velocity in the early period of time. In other words, the bottom friction becomes complicated and thus difficult to be described by a simple term.

Furthermore, based on the breaking criteria Eq. (3.69), the breaking conditions of the cases in Table 5.2 are investigated, even though the numerical model can deal with the breaking automatically. Thus, all the bottom motions enabling to generate non-breaking waves are denoted by dot in Fig. 5.24 while breaking waves by asterisk. It is expected that quicker bottom motion can advance the wave breaking. Moreover, waves are much easier to break on gentler beaches and greater α with the same bottom motion parameters. Additionally, the leading-

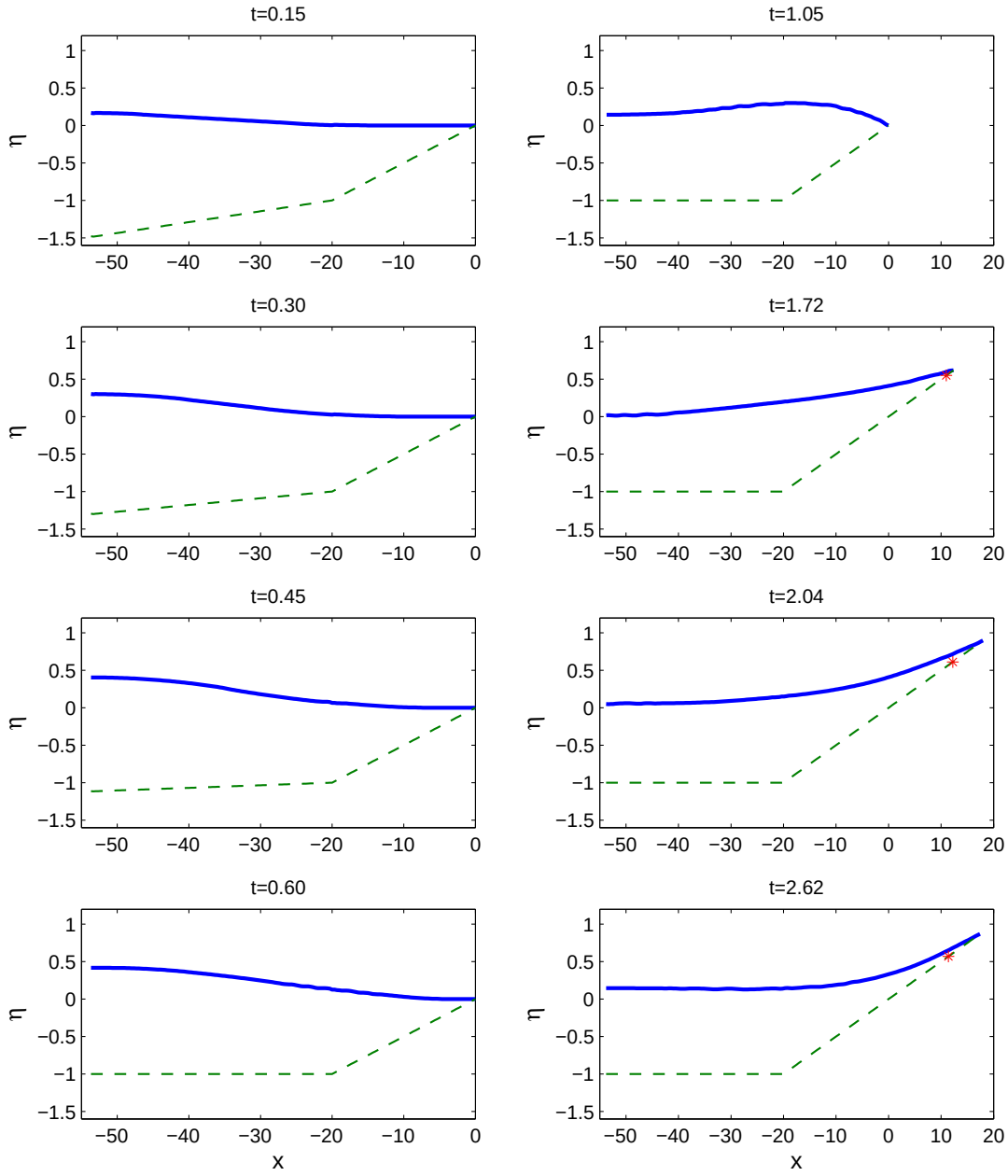

Figure 5.21: Run-up process of the waves generated by the upward bottom motion with $\alpha = 0.03$, $a = 0.67$ and $b = 0.54$ at slope of 1/20: Solid line, numerical results; dashed line, tank bottom; asterisk, experimental data.

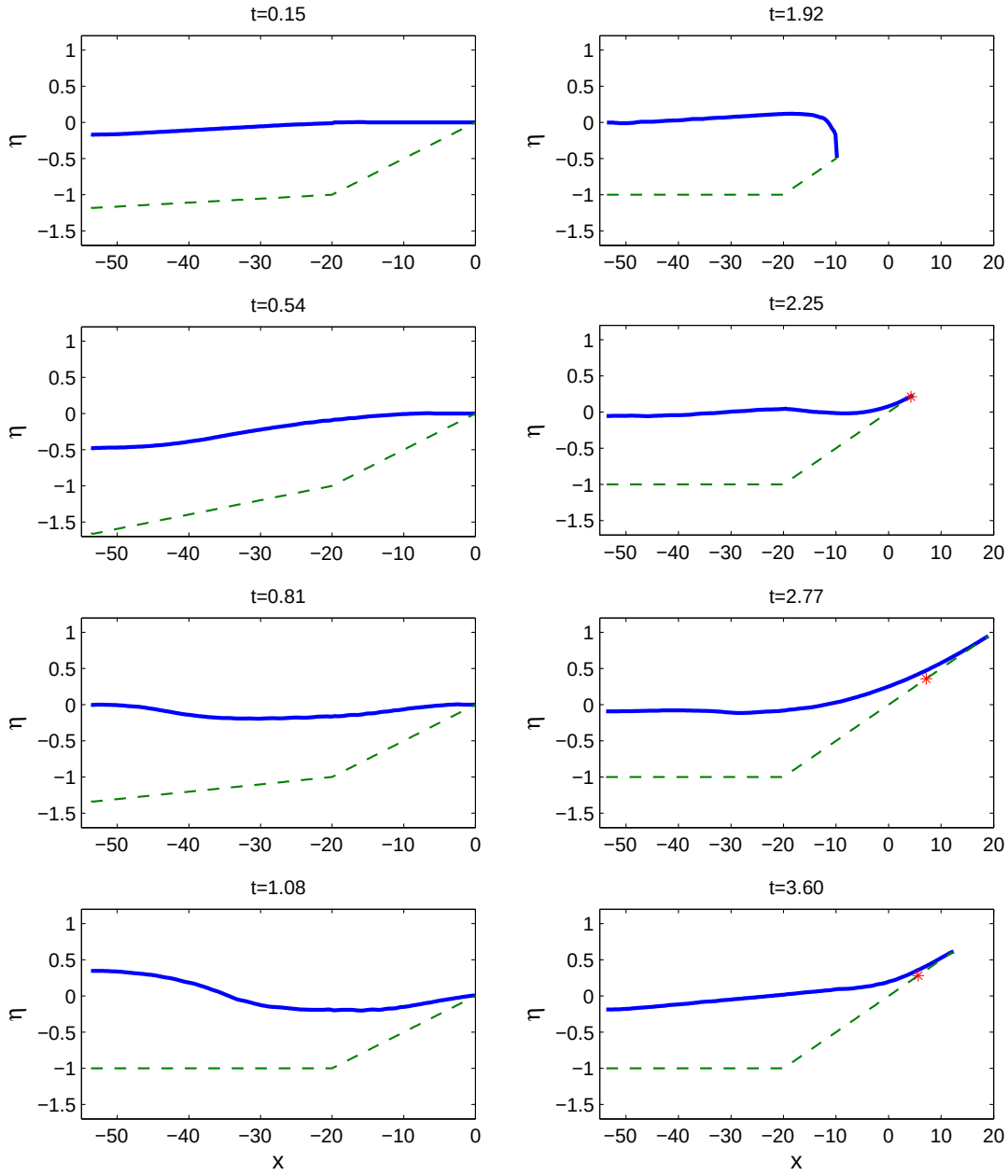

Figure 5.22: Run-up process of the waves generated by the down-upward bottom motion with $\alpha = 0.03$, $a = 0.67$ and $b = 0.54$ at slope of 1/20: Solid line, numerical results; dashed line, tank bottom; asterisk, experimental data.

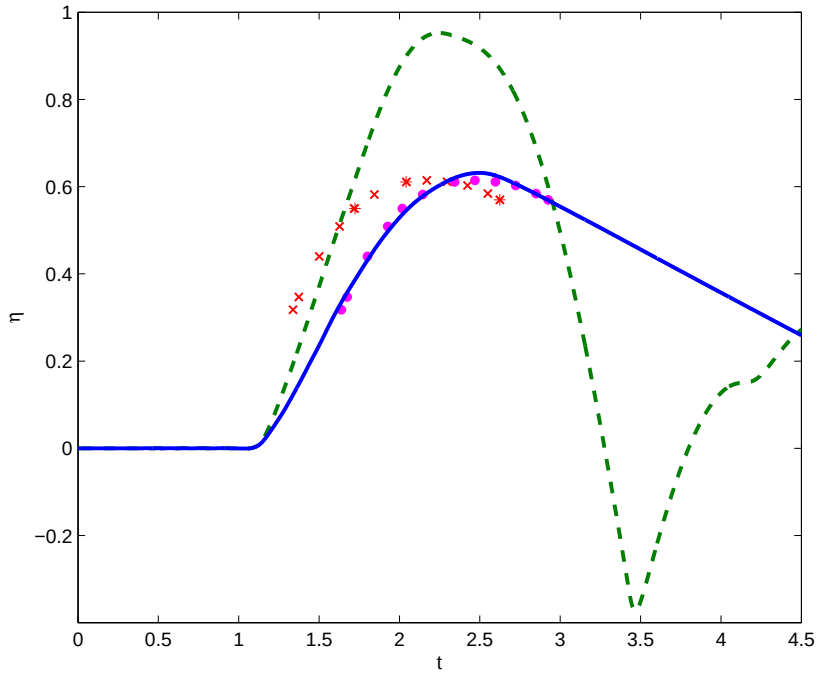

(a) upward motion

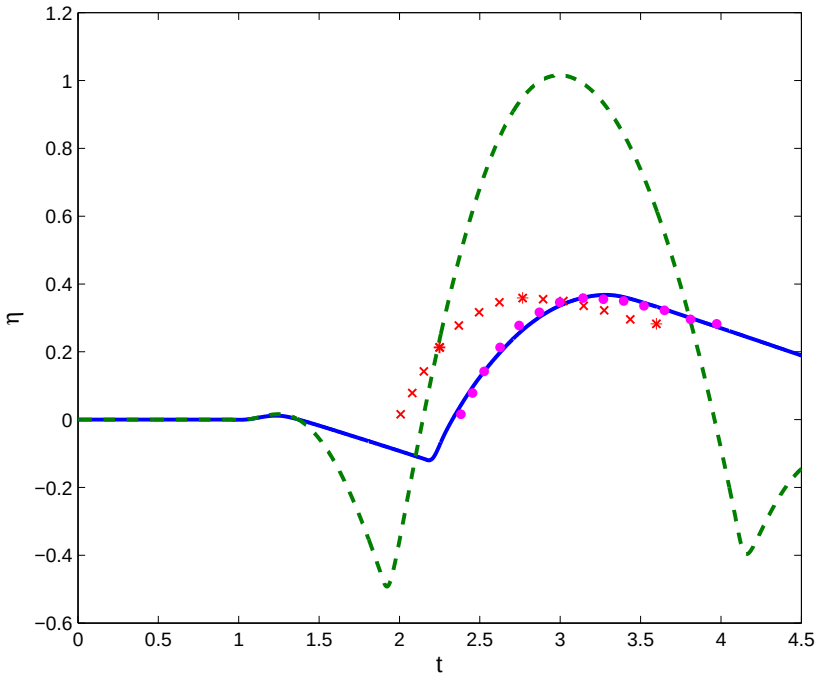

(b) down-upward motion

Figure 5.23: Comparison of the shoreline elevation time history with $\alpha = 0.03$, $a = 0.67$ and $b = 0.54$ at the slope of 1/20: Solid line, theoretical results with bottom friction considered; dashed line, theoretical results without bottom friction considered; $\times$, experimental data; $\cdot$, retarded experimental data; asterisk, experimental data in Fig. 5.21 and Fig. 5.22.

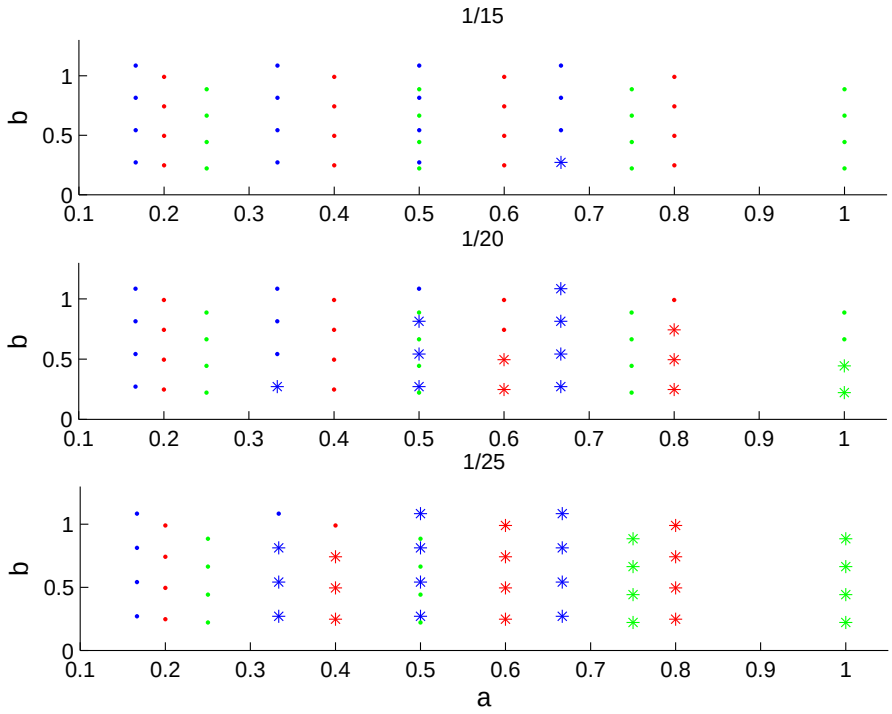

(a) upward motion

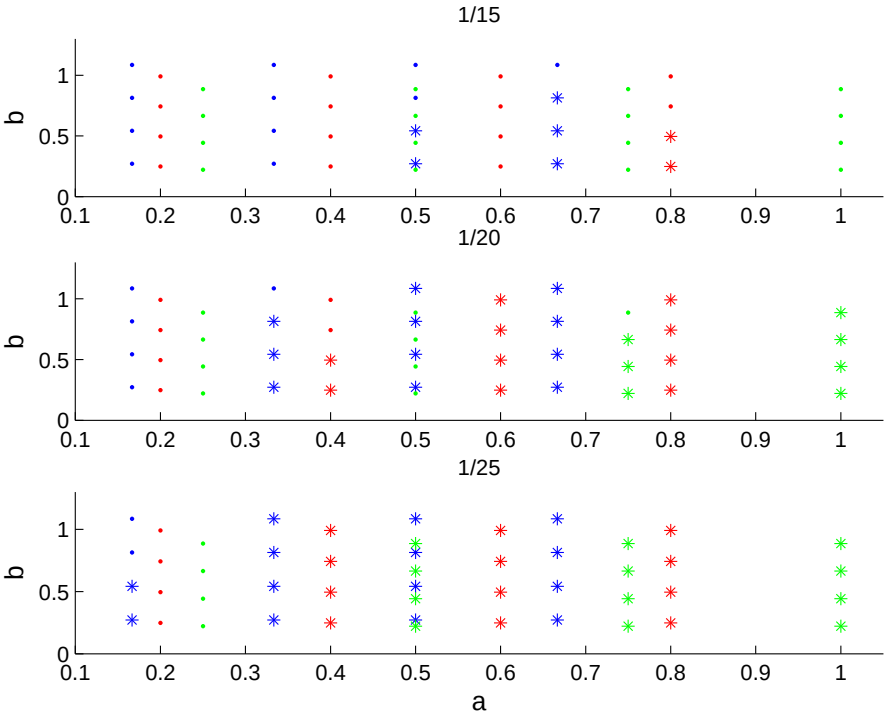

(b) down-upward motion

Figure 5.24: Breaking conditions of the waves: dot, non-breaking waves; asterisk, breaking waves; blue, $\alpha = 0.03$; red, $\alpha = 0.025$; green, $\alpha = 0.02$.

depression waves break more easily than the leading-elevation waves.

5.2.3 Effects of bottom motion on run-up

The maximum run-up height R_m can be obtained by capturing the furthest location from the time history of the shoreline. The experimental results of the maximum run-up height of the long waves on the plane beach with $\gamma = 1/20$ are plotted against the bottom motion amplitude a and the duration time b in Fig. 5.25 (upward motion) and Fig. 5.26 (down-upward motion). It has been found that waves have greater R_m on gentler beaches, but the differences are not obvious. Thus, only waves for the plane beach with the slope of $\gamma = 1/20$ are shown for example, while the others are shown in Appendix A.

Fig. 5.25 reveals the relation between the motion parameters and the maximum run-up height for upward motions. Note that these all can be found for the other two slopes. It is observed that R_m goes up with increasing motion amplitude, but opposite trends are found for the motion duration time. Obviously, greater motion displacement drives more water to uprush the beach, which results in a greater run-up height. For smaller motion duration time, greater initial velocities are given to the water which increases the energy of the waves and makes the wave run-up higher if the volume of the displaced water is fixed. Due to the characteristics of the upward motion, same volume of the water is lowered initially and then lifted at same a. Thus, the maximum run-up height decreases monotonously with b. These trends are similar to the ones between the wave profile and the bottom motions discussed in Fig. 5.18 (a) and Fig. 5.19 (a). R_m has monotonous dependence on the wave height and the wave front steepness.

Fig. 5.26 demonstrates the dependence of R_m on the down-upward bottom motions. As discussed in Fig. 5.19 (b), the wave height and the volume of the displaced water increase with b for leading-depression waves. Hence, the maximum run-up height grows with increasing b though the increase becomes slower at greater b. In addition, the increasing trend turns to a slight drop at the greatest

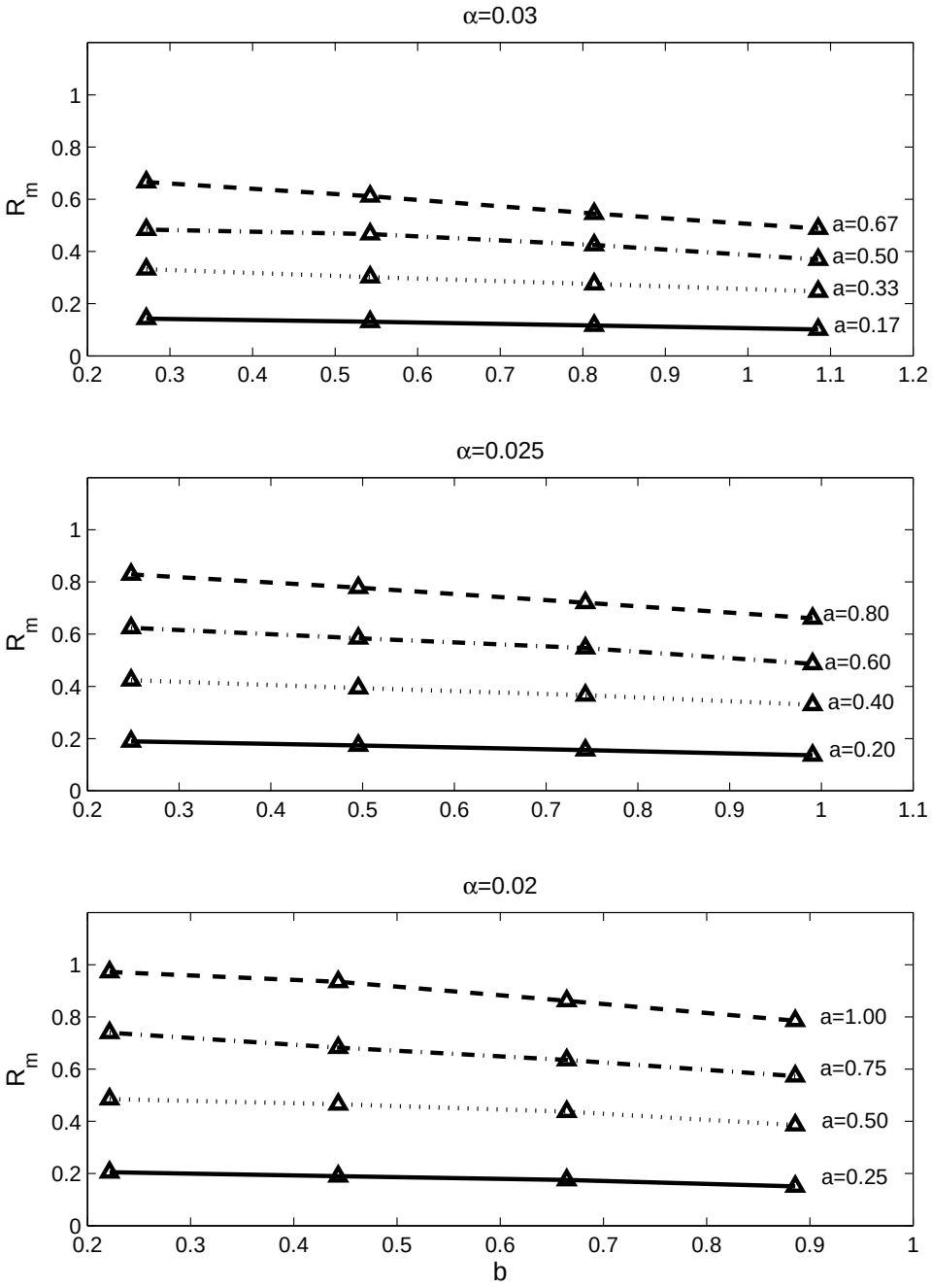

Figure 5.25: The maximum run-up height plotted against varying a and b with $\gamma = 1/20$ for upward motions.

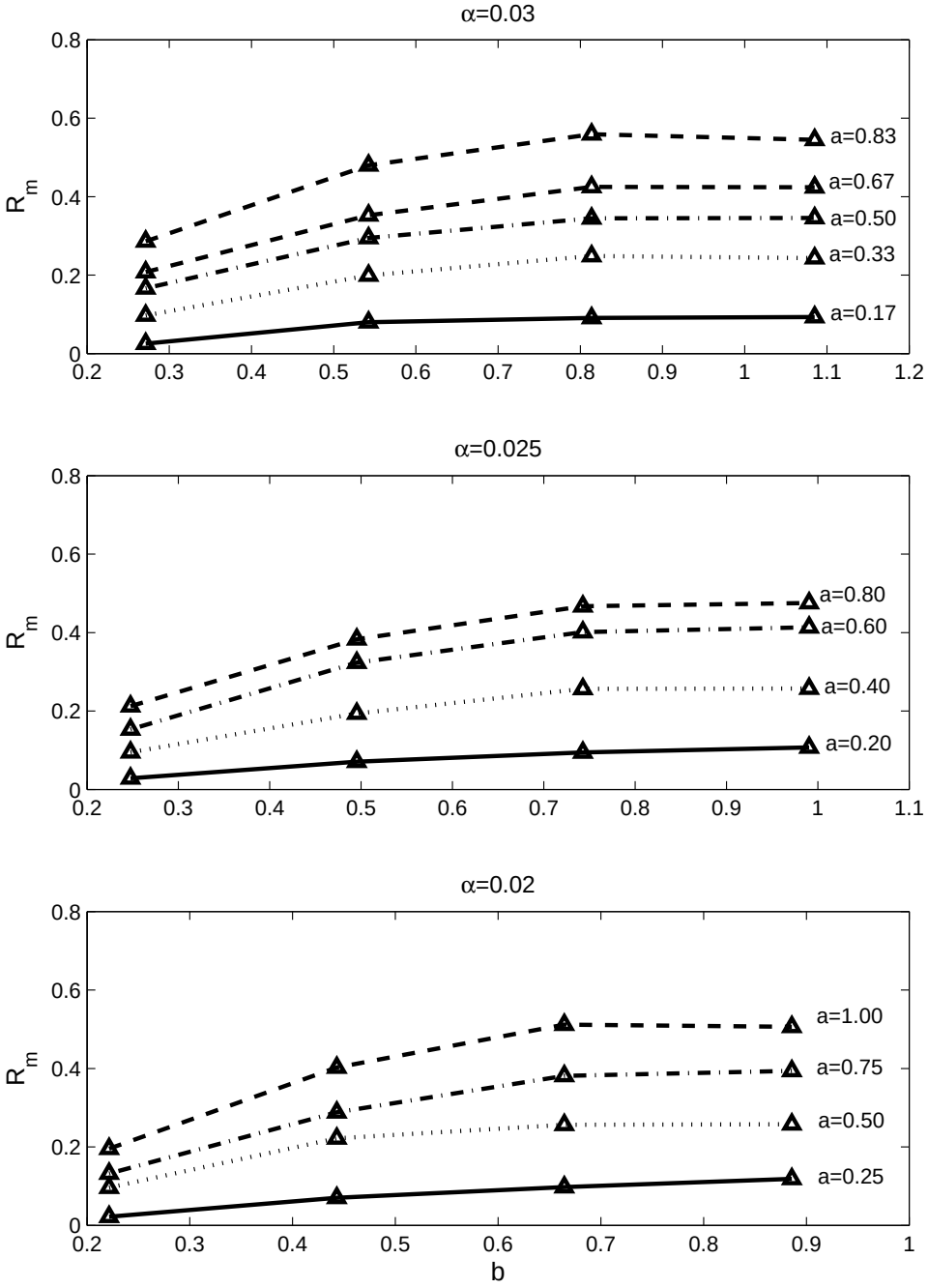

Figure 5.26: The maximum run-up height plotted against varying a and b with $\gamma = 1/20$ for down-upward motions.

b and a for all three α. The slower increasing trend could be caused by the elongation of the wave profile by slow motion which reduces the wave front steepness and the wave height. However, elongation is not the only cause since the drop of the increasing trend of R_m with b becomes obvious for bigger motion amplitude.

Focusing on the drop of the increasing trend of R_m with b, R_m of the high-amplitude waves generated by the down-upward motions with the largest a for every α is plotted against the varying b and compared between the three γ as shown in Fig. 5.27. There is a lack of information of waves by the bottom motions with $a = 0.67$ for $\alpha = 0.03$ and slope of 1/25 due to the limited length of the wave tank. After the turning point of b, it can be found that the shoreline recedes from the beach apparently before the finish of the bottom motion in Fig 5.28 for the waves shown in the last row of Fig. 5.27 with $\gamma = 1/20$. It is caused by that too slow motion and high motion displacement leave more space for the water on beach to fill, which lowers the shoreline location before the arrival of the wave and reduces the maximum run-up height. That explains that the drop is much more obvious with greater a in Fig. 5.26 and Fig. 5.27. The drop becomes more obvious for steeper slopes because there is a greater height difference of the shoreline on steeper slope when same amount of water is lowered to fill the moving area. Additionally, Fig. 5.27 also demonstrates that greater R_m is induced by gentler slope for down-upward motion.

So far, the dependence of R_m on the wave profile becomes noticeable, in particular that R_m of the incident waves in Fig. 5.20 follows how their accelerating phases vary with b. From previous studies, both Tadepalli and Synolakis (1994) and Chan and Liu (2012) have stated that the accelerating phase controls the run-up height. As a result, the effects of the bottom motion parameters a and b can be concluded into two factors: wave height and wave front steepness.

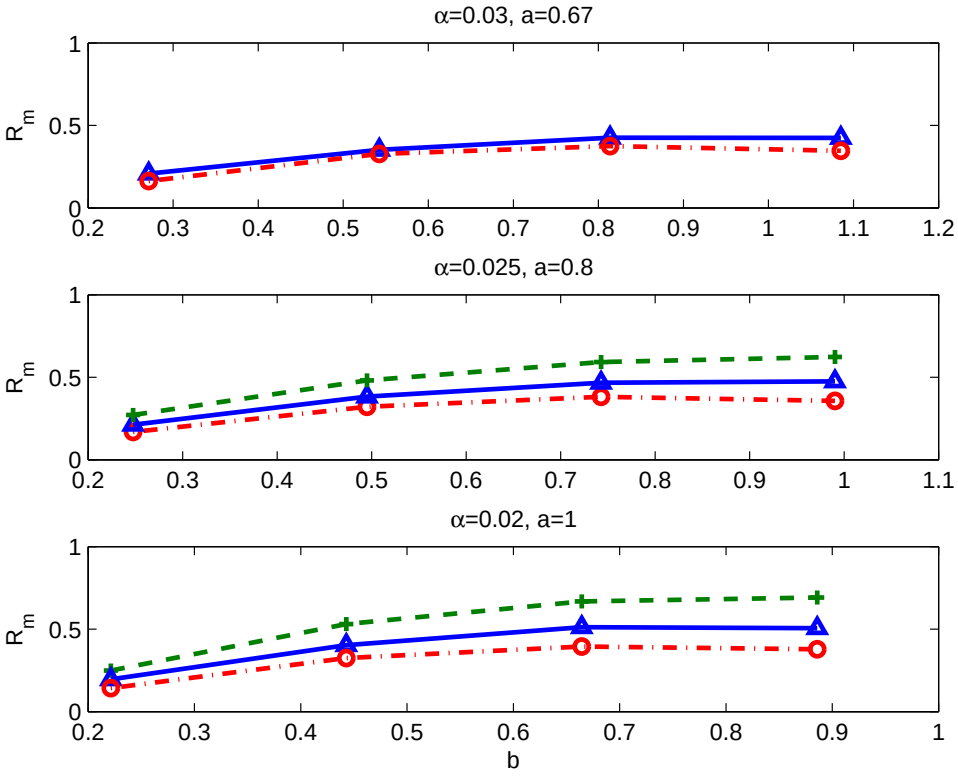

Figure 5.27: Experimental data of the maximum run-up height of the generated waves by down-upward motions plotted against b with $a = 0.67$, $a = 0.8$ and $a = 1.0$, respectively: $+$, $\gamma = 1/25$; $\triangle$, $\gamma = 1/20$; $\circ$, $\gamma = 1/15$.

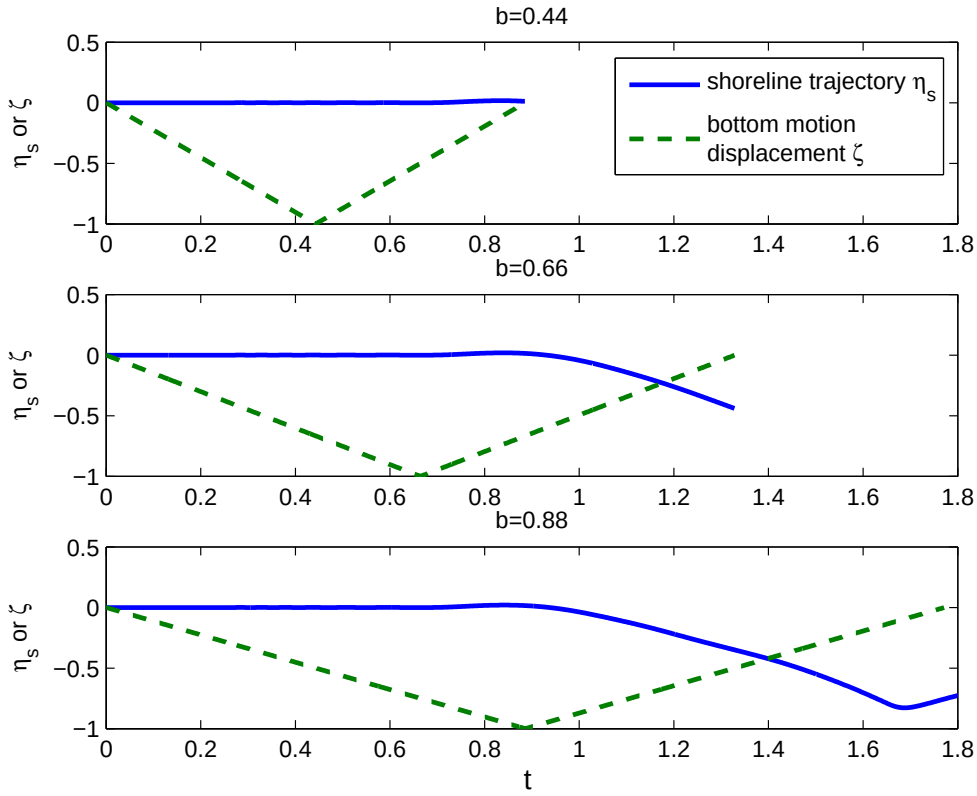

Figure 5.28: Plots of the shoreline trajectory (solid line) and the bottom motion displacement (dashed line) of the high-amplitude generated waves by down-upward motions with $\alpha = 0.02$, $a = 1.0$, $\gamma = 1/20$ and varying b.

5.2.4 Wave profile of the leading waves and the influence on wave run-up

Wave front profile (accelerating phase) is of great interest in this subsection with respect to the wave front steepness and the wave height for the generated leading-elevation or leading-depression waves. As Chan and Liu (2012) have shown in their study that the back-profiles of the elevations are not important to the run-up process and their maximum run-up heights, only the front profile is taken into consideration. Tadepalli and Synolakis (1994) also mentioned in their study that the N-waves have the same run-up height to the solitary waves with the same accelerating profile and wave height regardless of the back-profiles. Moreover, according to the analytical solution (3.71), it can be clearly found that the wave steepness (η_t) of the incident wave plays a crucial role in estimating the time histories of the run-up height.

Here, the accelerating phase is determined as the part of the profile from the beginning to the wave crest for the leading-elevation waves and from the wave trough to the crest for the leading-depression waves, respectively. Then, the steepness of the accelerating phase is given by $\kappa = (\eta_{peak} - \eta_{nadir})/(t_{peak} - t_{nadir})$ with $\eta_t > 0$, indicating that greater κ leads to a steeper wave front. Note that the starting point is regarded as the nadir for leading-elevation waves.

As the incident waves are determined as the generated long waves in a semi-infinite long wave tank with no regard to beach slope numerically, the wave front steepness κ of all the incident waves relating to different bottom motions are obtained from the BE system with a semi-infinite domain and presented in Fig. 5.29 (leading-elevation waves) and Fig. 5.30 (leading-depression waves). Interestingly, κ behaves almost the same to how R_m trends with the varying bottom motion parameters as depicted in Fig. 5.25 and Fig. 5.26. Greater motion amplitude leads to steeper wave front, for both leading-elevation and depression waves. Wave front steepness decreases with increasing motion duration time for the leading-elevation waves, but there is no monotonous dependence that relates κ and b for the leading-depression waves. Similar to the trends in Fig. 5.26, the

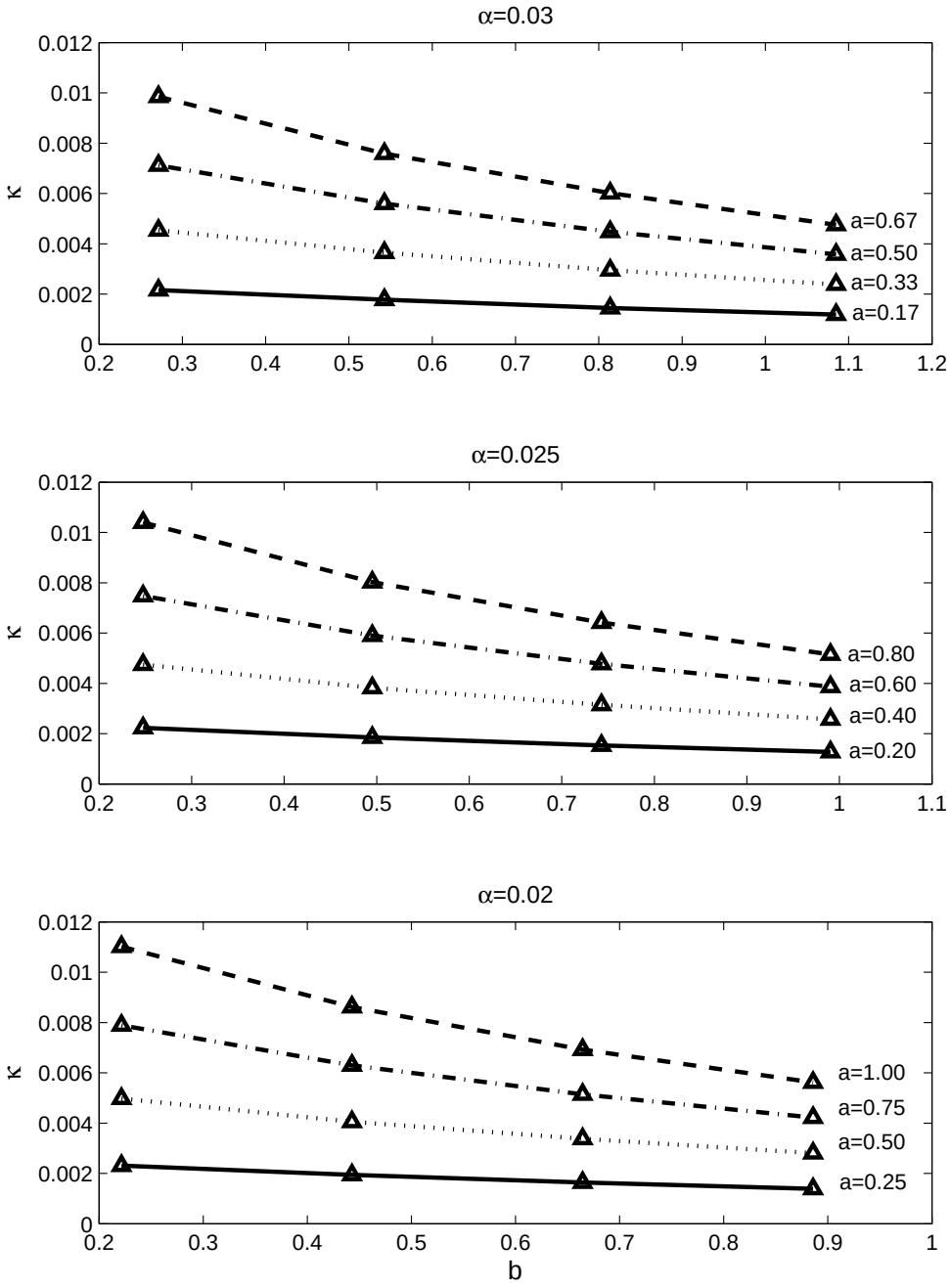

Figure 5.29: Plot of the wave front steepness against varying a and b for leading-elevation waves.

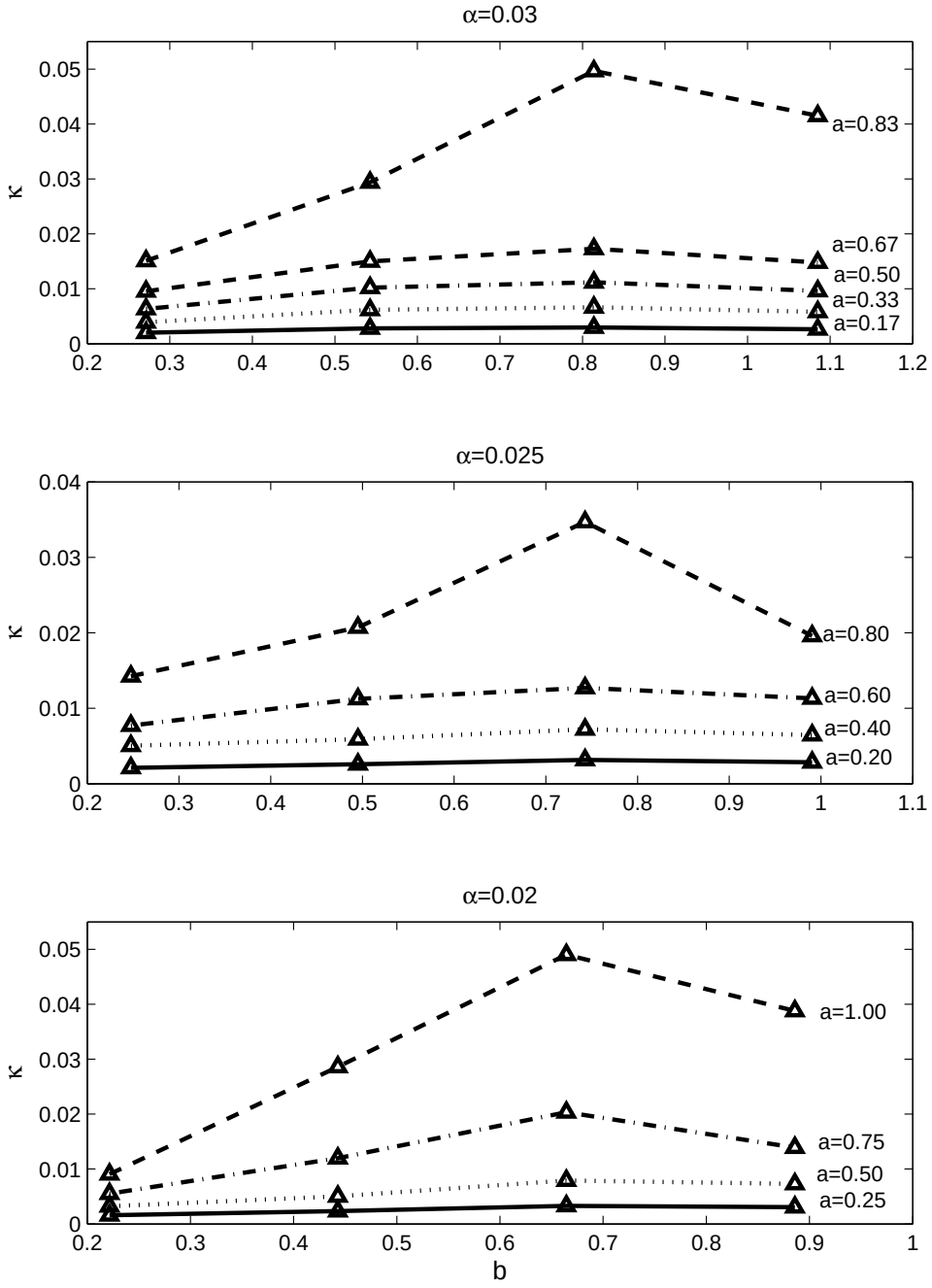

Figure 5.30: Plot of the wave front steepness against varying a and b for leading-depression waves.

increasing trend slows down and even drops at greater a and b for the leading-depression waves. Thus, it suggests that the wave front steepness is an important fact to determine the wave run-up height, which will be validated later.

To further investigate the wave profile of the leading waves, the wave front steepness (numerical results) and the wave height (experimental results) are used to relate the maximum run-up height of the generated long waves. Fig. 5.31 depicts the maximum run-up height as a function of wave front steepness. It indicates that R_m grows with the increasing κ, although the results appear scattering for both motions, in particular the leading-elevation waves. The experimental data are also compared to some realistic tsunami data (circle) from the 2011 Tohoku Earthquake Tsunami Joint Survey Group (Mori et al., 2011). The realistic tsunamis show same tendency that run-up height grows with κ, though they have greater run-up height at same κ. For leading-depression waves, the increase slows down at roughly $\kappa = 0.010$. It could be caused by that the effects of the wave breaking become more significant when waves reach a critical point, e.g., roughly $\kappa > 0.010$ here. Moreover, the waves generated by upward motion have greater R_m than the waves by down-upward motions at same κ. It is not only because of their different wave forms but also the different wave heights at the same steepness. Then, different wave heights of the waves at the same κ result in the scattering in the monotonous relation in Fig. 5.31.

In respect of the wave height, Synolakis (1987) already related the wave height to the maximum run-up height. Here, the maximum run-up height plotted as a function of the wave height is shown in Fig. 5.32 by using the experimental data, where the experimental results by Synolakis (1987) are denoted by '$\circ$'. It is noted that A is defined as the average height of the peak and the nadir for the leading-depression waves to be comparable with the leading-elevation waves.

Clearly, R_m increases almost linearly with A, in particular for the leading-elevation waves. In comparison with the dimensionless results by Synolakis (1987) with the slope of $\gamma = 1/19.85$ for solitary waves, the waves with $\gamma = 1/20$ give smaller R_m for smaller leading-elevation waves with $A < 0.15$, while greater R_m for

high-amplitude waves with $A > 0.20$. For waves with $0.15 < A < 0.20$, the results of R_m of the two wave models are approaching. It appears that high-amplitude leading-elevation waves are not significantly affected by wave breaking. Similarly, by comparing the maximum run-up height between the leading-elevation and depression waves, R_m for leading-elevation waves is greater than that for leading-depression waves at the same wave amplitude, which is opposite to field observations. The opposite tendency might be caused by the much smaller wave front steepness of the leading-depression waves. The wave height of the leading-depression waves grows with A due to more additional displaced water volume by slower motion. However, slower motion with bigger b elongates the wave front profile and decreases the front steepness.

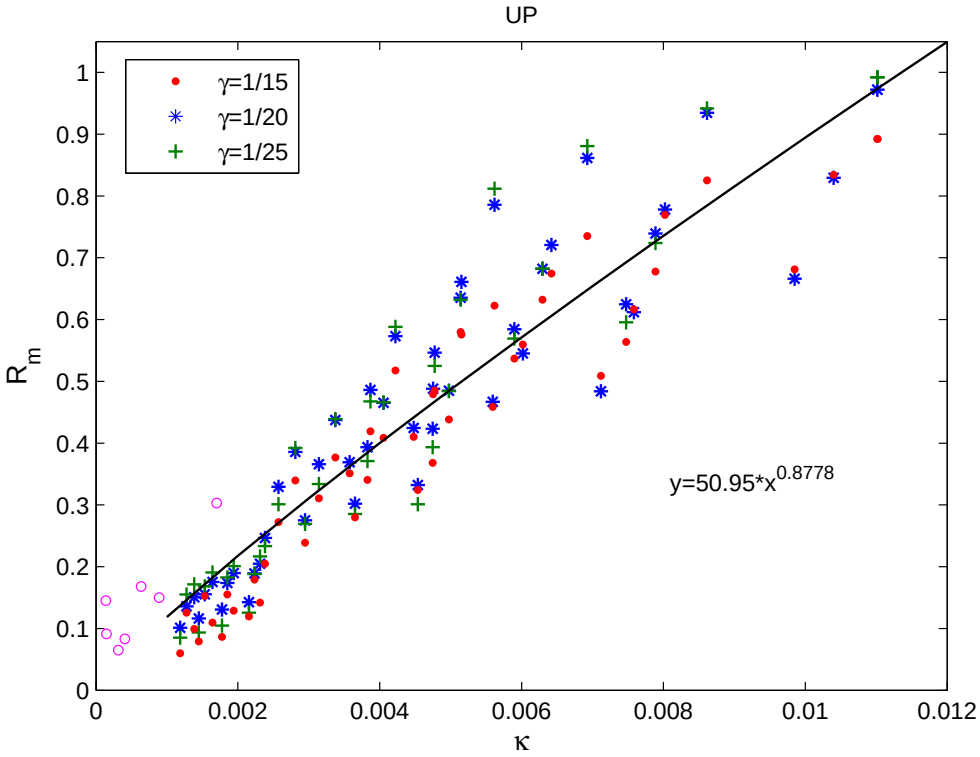

(a) upward motion

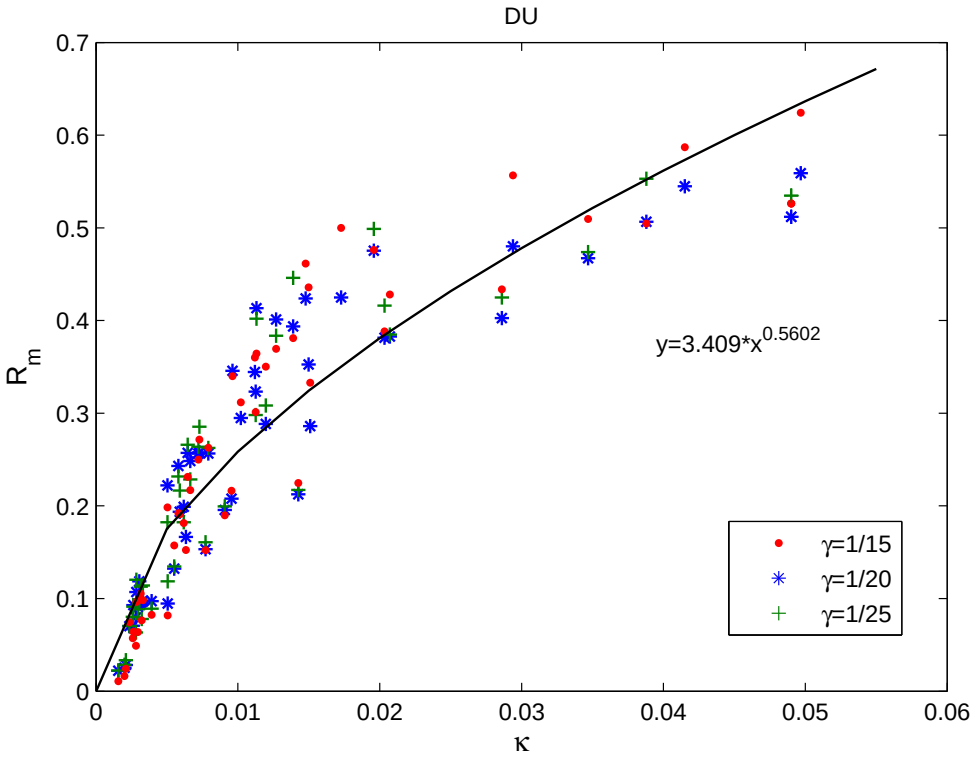

(b) down-upward motion

Figure 5.31: Maximum run-up height plotted as a function of the front steepness compared between the experimental and numerical results.

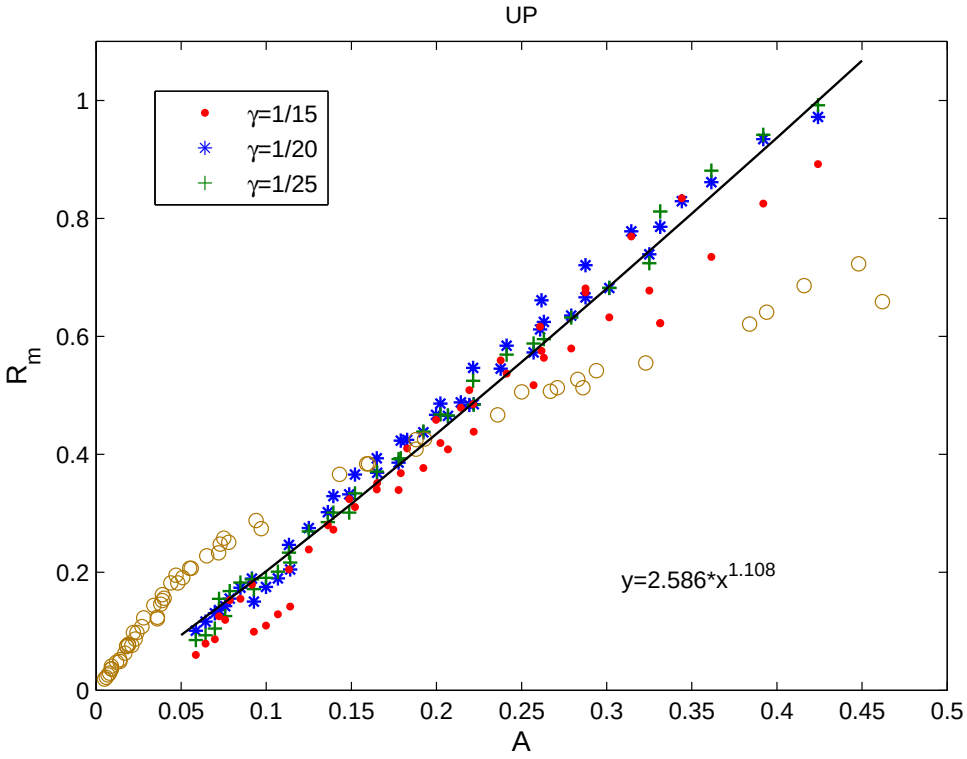

(a) upward motion

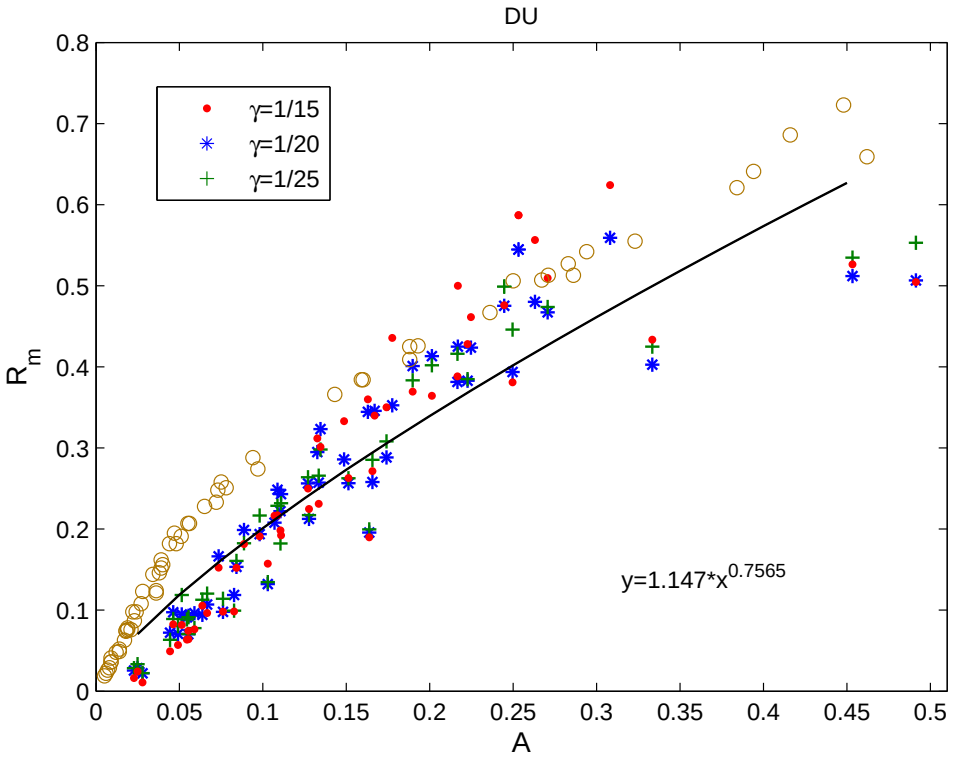

(b) down-upward motion

Figure 5.32: Maximum run-up height plotted as a function of wave height compared between the experimental results and results by Synolakis (1987) (circle).

Chapter 6

Summary and Conclusions

6.1 Summary

A number of previous studies have been reviewed about creating long waves in laboratory or developing long wave models numerically for tsunamis. However, recent research raised the question that the commonly used waves to model tsunamis are at least one order-of-magnitude shorter than the field observations. It calls for advancement of wave generating paradigm. Therefore, the present study aims to develop a new wave maker that can generate waves longer than solitary waves in terms of the effective wavelength in laboratory and re-evaluate the current understanding of tsunamis. The problem of wave run-up along a plane beach is also of interest.

The new wave generator used in this study is a bottom-tilting wave maker, which generates long waves by moving the bottom hinged at the toe of the beach with adjustable slope controlled by an electric servo motor. By changing the water depth, bottom motion displacement and speed, different waves have been created and investigated according to the ranges of parameters in Table 5.1 for wave generation investigation and in Table 5.2 for wave run-up investigation, with respect to different motion types.

Experiments were conducted to measure the wave surface elevation time histories, the shoreline moving trajectory and the maximum run-up height in the laboratory. Wave gauges were used to examine the generated long waves or the incident waves at the toe of the slope for wave run-up. A camera settled on the top of the tank has been used to observe the maximum run-up height of the varying generated long waves.

A number of numerical methods widely used in solving long waves propagating in shallow water and running up a plane slope were reviewed. Some of them pertaining to this research were further developed for modelling the wave behaviour in the new wave tank. The linear wave theory can provide the estimation of the leading order of the small-amplitude waves generated according to the two-dimensional Laplace equation along with the simplified and linearised boundary conditions. Also, the analytical solution (3.37) has been used as the incident wave for the analytical solution of the run-up time history (3.71).

Numerical schemes have been verified by good agreements between the theoretical results and the experimental measurements, both in wave generation and wave run-up. Meanwhile, the theoretical results verified the ability of the new wave maker for generate more practical long-waves. Then, parametric studies of the wave profiles as well as the maximum run-up heights of the generated long waves on a plane beach have been taken both experimentally and theoretically. In particular, the two aspects were linked to the wave characteristics, in other words, the wave characteristics can be described by bottom motion parameters.

6.2 Conclusions

The key conclusions and contributions are highlighted as follows:

- A new wave maker is developed in this study with the generation region of a moving bottom can be directly connected to a plane sloping beach. Thus, the possible deformation during wave propagation can be ignored.

The main concept has been verified that the generated waves can be as long as the wave tank when the whole bottom is moved, which is at least 2 m long for all the waves observed. The another advantage is that the beach slope is adjustable and easily manageable.

- The analytical solution (3.26) was derived by the linear wave theory. Taking into account the symmetry and simplification of the observed bottom motions, the general solution (3.26) has been specified into the analytical solution (3.37) by a superposition of the impulsive motions. Thus, given the bottom motion parameters a and b, the free surface elevation of small-amplitude waves can be predicted in an unbounded domain.

- The analytical solution (3.37) has been used to initially verify the idea of the new wave maker by introducing the ratio L_w/L_s and facilitate the design of the specific geometry of the new wave maker. The linear investigation suggested that $\alpha < 0.7$ should be satisfied for generating waves longer than the solitary waves of same wave amplitude in terms of the effective wavelength. It should be noted that the rotational effects on the vertical displacement of the bottom were ignored due to the small rotating angle.

- A numerical model based on the Boussinesq equations has been developed to simulate the evolution of the long waves in the tank without beach, while a numerical model based on the NSW equation has been built to approximate the wave behaviour in the tank with beach. A finite volume method combined with high-order reconstruction methods (UNO, WENO), has been used to numerically solve the equations, giving the benefits of conservative and shock-capturing properties.

- The three high-order reconstruction schemes (UNO2, WENO3 and WENO5) were compared to one another. UNO2 scheme is the least time-consuming and with comparable accuracy, which has been applied to solve the Boussinesq equations for wave generation only. Due to the higher order accuracy, WENO schemes have been used for the NSW equations system to simulate the more complicated wave run-up process.

- The amplitudes and periods of the generated waves were related to the parameters of the simple bottom motions. The wave amplitudes were well described in terms of the volume flux of the displaced water, and two fitting functions of the form $A = m(b/V_w)^{-n}$ have been suggested. However, the wave periods show much more complicated trends due to combined effects of nonlinearity and dispersion. It is noted that the wave period was determined by the numerical model in semi-infinite domain, while the wave peak time was used to validate the numerical model and determine the wave period of small-amplitude waves.

- The resulting wave amplitude increases with either increasing bottom motion displacement or decreasing motion duration time. The early disintegration can eliminate the effects of motion duration time on the wave amplitude for the same motion displacement, in particular for high-amplitude waves.

- Both the resulting wave period and wave peak time increase with bottom motion duration time. The wave peak time of the leading-elevation waves decreases with the motion displacement, but it is opposite for the leading-depression waves. Then, due to the nonlinear effects, the wave period is greater than the double T_a for leading-elevation waves while the leading-depression waves have the opposite trend. Therefore, growing motion displacement results in slightly greater wave period time for the leading-elevation waves. However, for waves caused by downwards motion, the wave period has no monotonous dependence on the bottom motion displacement due to the combined effects of nonlinearity and dispersion.

- In comparison of the ratio L_w/L_s from the numerical model based on the Boussinesq equations, relatively longer waves than the solitary waves with same amplitude can be generated in the wave tank, which can be at most seven times longer in terms of the effective wavelength. Slow high-amplitude bottom motions with longer moving bottom can lead to even longer waves theoretically.

- It has been found that with one moving bottom in simple monotonous mo-

tions, it is able to generate waves that are markedly similar to the field data of 2011 Japan Tohoku tsunami. Substantial improvements have been found in the long waves generated by the new wave maker over solitary waves theoretically by the numerical model based on the Boussinesq equations. It is expected that more sophisticated operation would result in even better agreement.

- The run-up process and the maximum run-up height can be estimated by the numerical modelling based on NSW equations by a high-order shock-capturing finite volume scheme developed in this study. In addition, the movement of the shoreline was approximated by the computational domain mapping technique. Moreover, the analytical solution (3.71) was used for verifying the numerical modelling and quickly evaluating for the non-breaking waves.

- It has been found that bottom friction plays an important role in dissipating the wave energy and reducing the wave run-up height, in particular in the very shallow wave front during running up. It is possible that the bottom friction term cannot be described by a simple function of water velocity. Moreover, surface tension can be another reason of smaller run-up height for small-amplitude waves in the range of capillary waves.

- Based on the analytical solution, the wave breaking has been observed for different bottom motions on different slopes. Waves are easier to break by high-speed bottom motions on gentler beach or in deeper water.

- Further exploration discovered the effects of the bottom motion on the run-up of the long waves generated in the new tank. Complicated trends found in waves generated by down-upward motions were formed in terms of the increase in displaced water volume and the elongation of the wave profile (wave period) by slow motion. It has been found that there is monotonous dependence of the maximum run-up height on the wave height (greater a or smaller b) for leading-elevation waves, which can be found in many studies on solitary waves.

- Furthermore, it has been verified that the steepness of the leading wave front controls the run-up process for a single wave. Wave height is another wave characteristic and influences the wave run-up height significantly. The maximum run-up height R_m can also be described as power functions of the wave front steepness or wave height. In general, high-amplitude wave with steeper wave front causes greater run-up height.

6.3 Future plans

It is remarked here that active absorption of the reflected waves needs to be considered for this wave maker to be more practical. This has not been discussed here as the focus is on modelling of the waves during and immediately after the generation stage. Within the linear theory, it can be shown that active absorption is possible without modification of the wave tank based on the inversion calculation of the reflected waves by the convolution theorem (3.40). This objective will be further pursued in the future work.

Additionally, a more advanced wave maker incorporating an array of multiple moving bottoms is currently under construction. This wave maker effectively changes the length of moving bottom and provides more degrees-of-freedom in operation.

Breaking of the long waves generated by the new wave maker is expected to be observed and discussed in future studies, although the analytical solutions have provided rough estimations and predictions. Visual investigation would be the main method to identify the wave breaking experimentally. The dependence of the wave breaking on the bottom motion parameters is expected to be examined and determined.

Finally, bottom friction needs to be discussed further in the future. Determining the bottom friction terms more practically will improve the accuracy of the numerical model for this new wave maker.

Appendix A

Plots of R_m

A.1 R_m plotted against varying bottom motions for $\gamma = 1/15$

A.2 R_m plotted against varying bottom motions for $\gamma = 1/25$

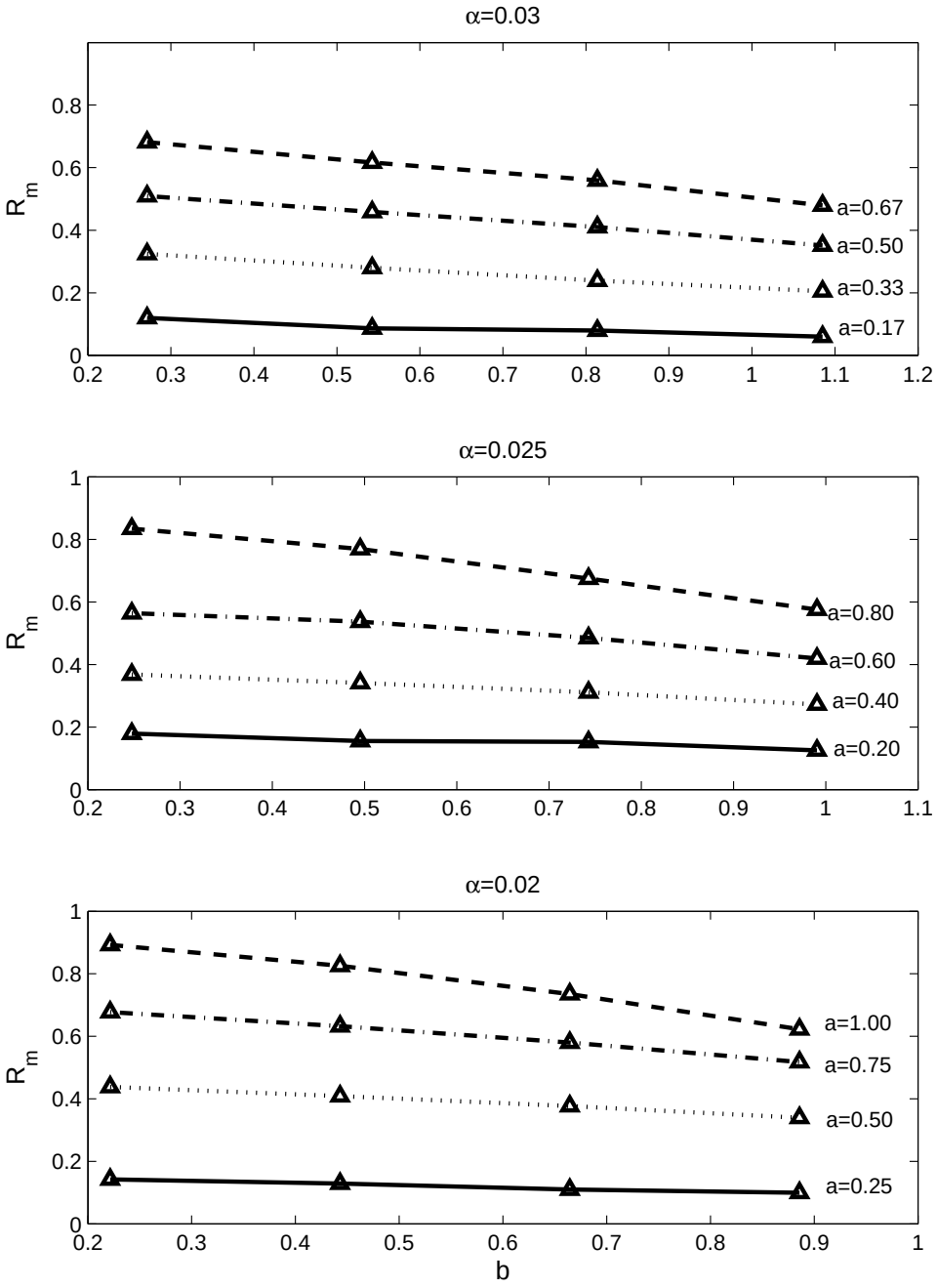

Figure A.1: The maximum run-up height plotted against varying a and b with $\gamma = 1/15$ for upward motions.

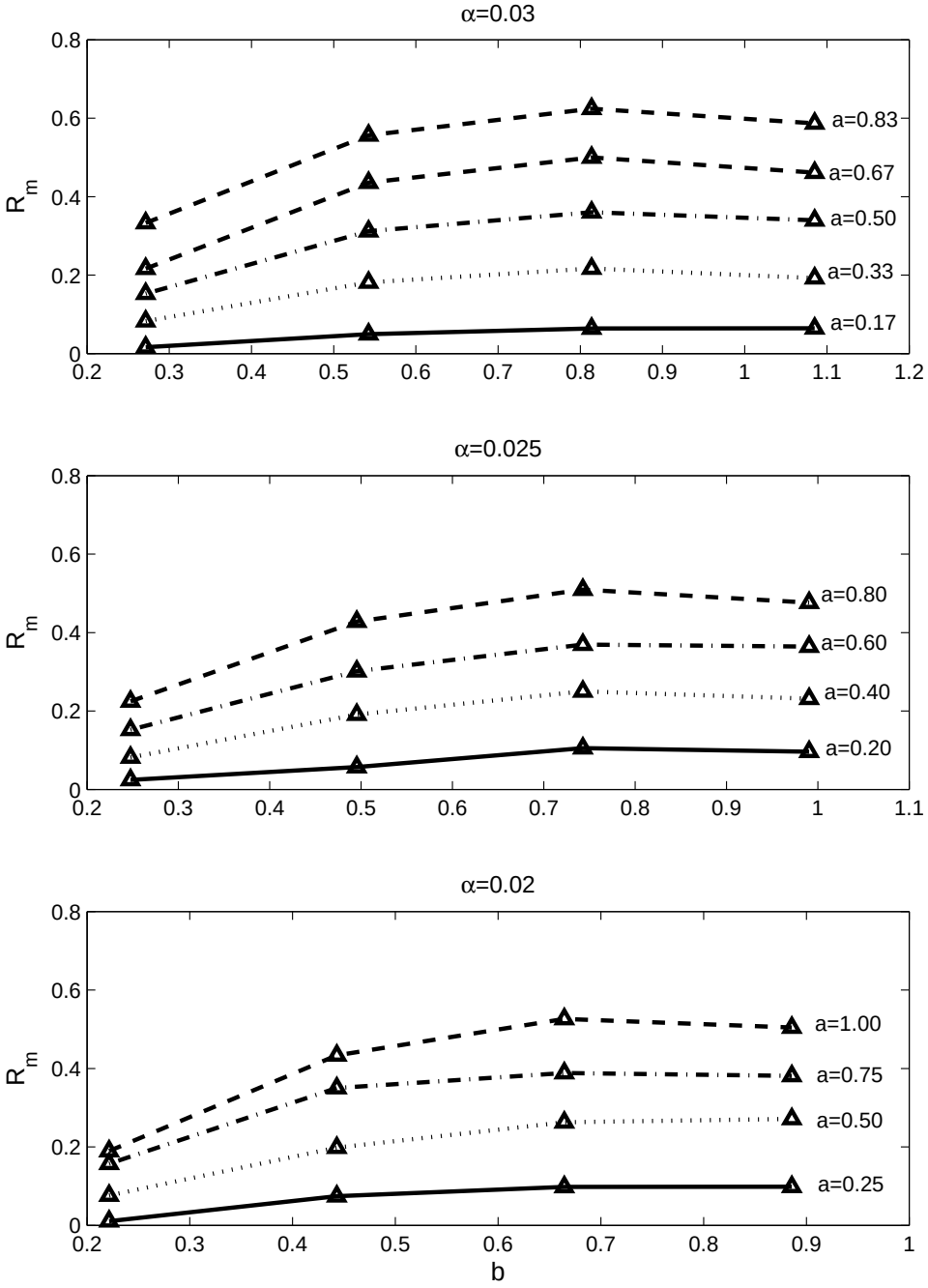

Figure A.2: The maximum run-up height plotted against varying a and b with $\gamma = 1/15$ for down-upward motions.

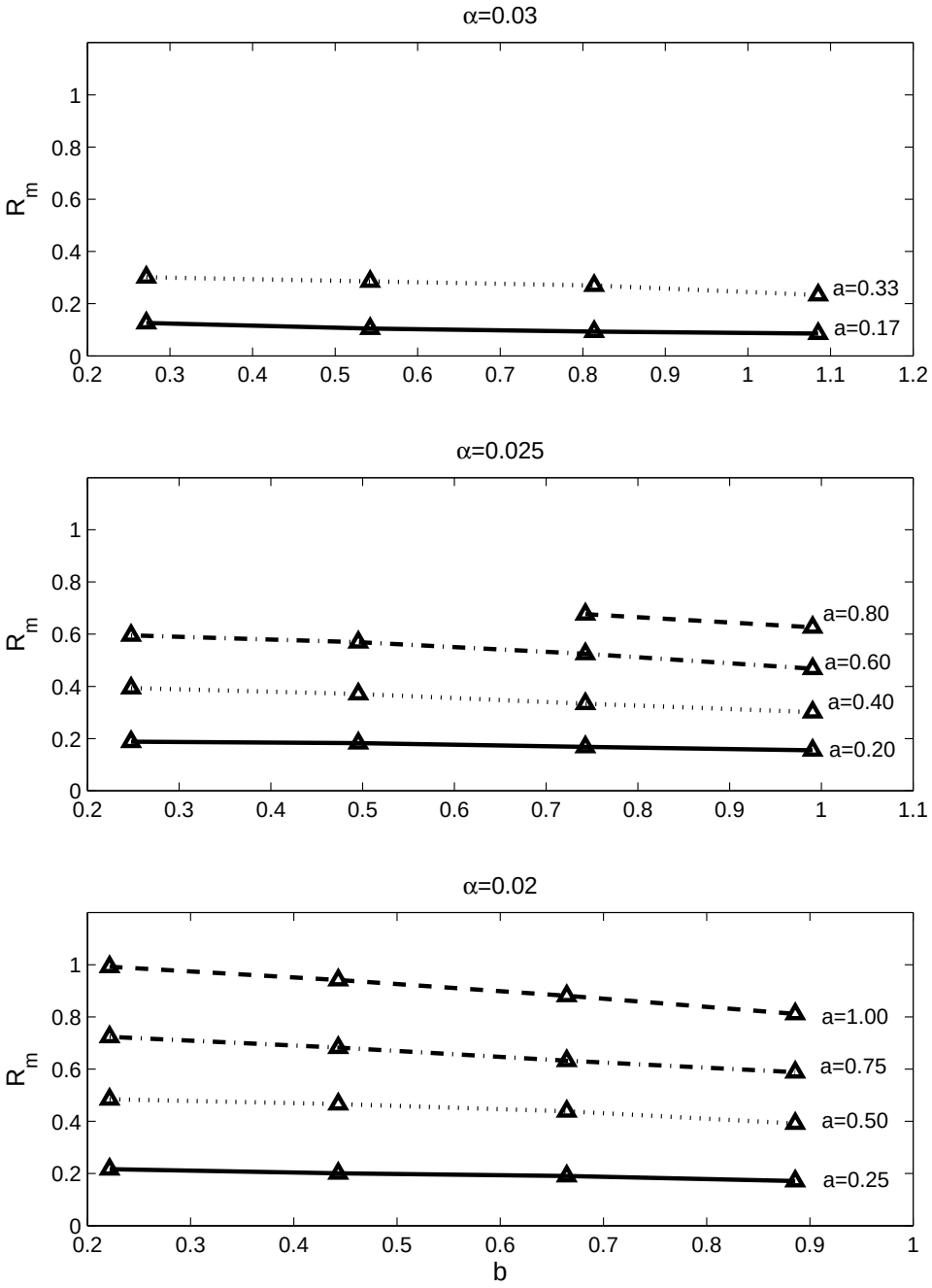

Figure A.3: The maximum run-up height plotted against varying a and b with $\gamma = 1/25$ for upward motions.

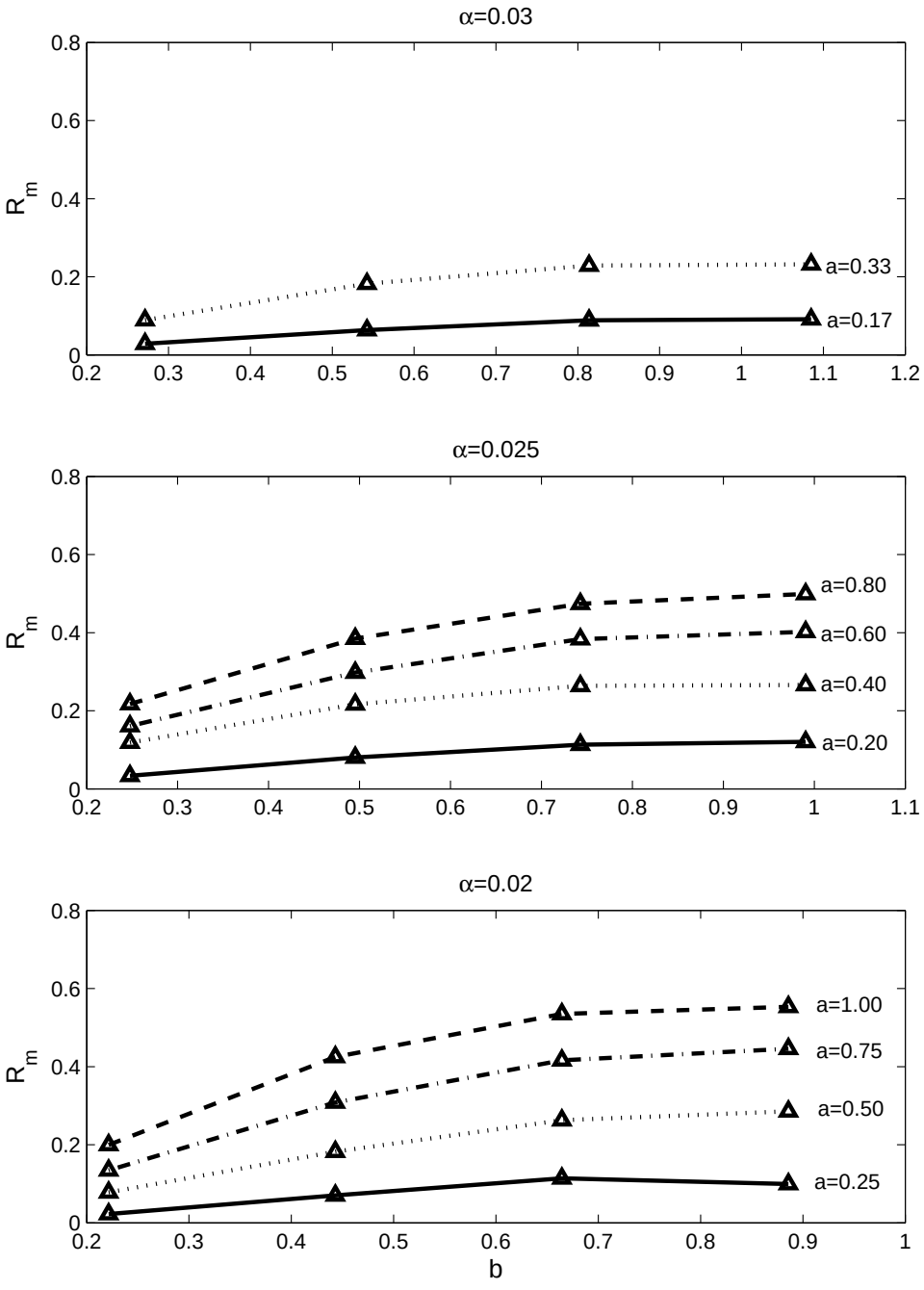

Figure A.4: The maximum run-up height plotted against varying a and b with $\gamma = 1/25$ for down-upward motions.

Bibliography

Bogacki, P. and Shampine, L. 1989. A 3(2) pair of Runge-Kutta formulas. *Appl. Math. Lett.*, 2(4):321–325.

Borthwick, A., Ford, M., Weston, B., Taylor, P., and Stansby, P. 2006. Solitary wave transformation, breaking and run-up at a beach. In *Proceedings of the Institution of Civil Engineers-Maritime Engineering*, volume 159, pages 97–105. Thomas Telford Ltd.

Boussinesq, J. 1872. Théorie des ondes et des remous qui se propagent le long d'un canal rectangulaire horizontal, en communiquant au liquide contenu dans ce canal des vitesses sensiblement pareilles de la surface au fond. *Journal de Mathématiques Pures et Appliquées*, pages 55–108.

Briggs, M. J., Synolakis, C. E., Harkins, G. S., and Green, D. R. 1995. Laboratory experiments of tsunami runup on a circular island. In *Tsunamis: 1992–1994*, pages 569–593. Springer.

Carrier, G. F. and Greenspan, H. P. 1958. Water waves of finite amplitude on a sloping beach. *J. Fluid Mech.*, 4(01):97–109.

Chan, I.-C. and Liu, P. L.-F. 2012. On the runup of long waves on a plane beach. *J. Geophys. Res.*, 117(C08006).

Chanson, H. 2005. Tidal bore processes in the baie du mont saint michel (france): field observations and discussion. In *31st IAHR Biennial Congress*, volume 2, pages 4037–4046. Korea Water Resources Association.

Craig, W. 2006. Surface water waves and tsunamis. *J. Dyn. Differ. Equ.*, 18(3):525–549.

Dodd, N. 1998. Numerical model of wave run-up, overtopping, and regeneration. *Journal of Waterway, Port, Coastal, and Ocean Engineering*, 124(2):73–81.

Dutykh, D. and Kalisch, H. 2013. Boussinesq modeling of surface waves due to underwater landslides. *Nonlinear Proc. Geoph.*, 20(3):267–285.

Dutykh, D., Katsaounis, T., and Mitsotakis, D. 2011. Finite volume schemes for dispersive wave propagation and runup. *J. Comput. Phys.*, 230(8):3035–3061.

Fujii, Y., Satake, K., Sakai, S., Shinohara, M., and Kanazawa, T. 2011. Tsunami source of the 2011 off the pacific coast of tohoku earthquake. *Earth, planets and space*, 63(7):815–820.

Goring, D. G. 1978. *Tsunamis–the propagation of long waves onto a shelf*. PhD thesis, California Institute of Technology.

Goseberg, N., Wurpts, A., and Schlurmann, T. 2013. Laboratory-scale generation of tsunami and long waves. *Coastal Engineering*, 79:57–74.

Grilli, S., Subramanya, R., Svendsen, I., and Veeramony, J. 1994. Shoaling of solitary waves on plane beaches. *Journal of Waterway, Port, Coastal, and Ocean Engineering*, 120(6):609–628.

Grilli, S., Svendsen, I., and Subramanya, R. 1997. Breaking criterion and characteristics for solitary waves on slopes. *Journal of waterway, port, coastal, and ocean engineering*, 123(3):102–112.

Hall, J. V. J. and Watts, G. M. 1953. Laboratory investigation of the vertical rise of solitary waves on impermeable slopes. Technical report, U.S. Beach Erosion Board.

Hammack, J. L. 1973. A note on tsunamis: their generation and propagation in an ocean of uniform depth. *J. Fluid Mech.*, 60(04):769–799.

Harten, A. and Osher, S. 1987. Uniformly high-order accurate nonoscillatory schemes. i. *SIAM J. Numer. Anal.*, 24(2):279–309.

Hibberd, S. and Peregrine, D. 1979. Surf and run-up on a beach: a uniform bore. *Journal of Fluid Mechanics*, 95(02):323–345.

Jensen, A., Pedersen, G. K., and Wood, D. J. 2003. An experimental study of wave run-up at a steep beach. *Journal of Fluid Mechanics*, 486(1):161–188.

Jiang, G.-S. and Shu, C.-W. 1996. Efficient implementation of weighted eno schemes. *Journal of computational physics*, 126(1):202–228.

Kajiura, K. 1963. The leading wave of a tsunami. *B. Earthq. Res. I. Tokyo*, 41:535–571.

Keller, J. B. and Keller, H. B. 1964. Water wave run-up on a beach. Technical report, U.S. Department of the Navy.

Kit, E., Shemer, L., and Miloh, T. 1987. Experimental and theoretical investigation of nonlinear sloshing waves in a rectangular channel. *Journal of Fluid Mechanics*, 181:265–291.

Li, Y. 2000. Tsunamis: Non-breaking and breaking solitary wave run-up.

Li, Y. and Raichlen, F. 2001. Solitary wave runup on plane slopes. *Journal of Waterway, Port, Coastal, and Ocean Engineering*, 127(1):33–44.

Li, Y. and Raichlen, F. 2002. Non-breaking and breaking solitary wave run-up. *J. Fluid Mech.*, 456:295–318.

Li, Y. and Raichlen, F. 2003. Energy balance model for breaking solitary wave runup. *Journal of Waterway, Port, Coastal, and Ocean Engineering*, 129(2):47–59.

Lin, P., Chang, K.-A., and Liu, P. L.-F. 1999. Runup and rundown of solitary waves on sloping beaches. *Journal of Waterway, Port, Coastal, and Ocean Engineering*, 125(5):247–255.

Liu, D. and Lin, P. 2008. A numerical study of three-dimensional liquid sloshing in tanks. *Journal of Computational Physics*, 227(8):3921–3939.

Liu, P. L.-F., Cho, Y.-S., Briggs, M. J., Kanoglu, U., and Synolakis, C. E. 1995. Runup of solitary waves on a circular island. *J. Fluid Mech.*, 302:259–285.

Liu, P. L.-F., Synolakis, C. E., and Yeh, H. H. 1991. Report on the international workshop on long-wave run-up. *Journal of Fluid Mechanics*, 229:675–688.

Liu, X.-D., Osher, S., and Chan, T. 1994. Weighted essentially non-oscillatory schemes. *J. Comput. Phys.*, 115(1):200?212.

Lo, H.-Y., Park, Y. S., and Liu, P. L.-F. 2013. On the run-up and back-wash processes of single and double solitary wavesan experimental study. *Coastal engineering*, 80:1–14.

Lu, H., Park, Y. S., and Cho, Y.-S. 2017. Modelling of long waves generated by bottom-tilting wave maker. *Coastal Engineering*, 122:1–9.

Lynett, P. J., Wu, T.-R., and Liu, P. L.-F. 2002. Modeling wave runup with depth-integrated equations. *Coastal Engineering*, 46(2):89–107.

Madsen, O. S. and Mei, C. C. 1969. The transformation of a solitary wave over an uneven bottom. *J. Fluid Mech.*, 39(04):781.

Madsen, P. A., Fuhrman, D. R., and Schäffer, H. A. 2008. On the solitary wave paradigm for tsunamis. *J. Geophys. Res.*, 113(C12012).

Madsen, P. A. and Schäffer, H. A. 2010. Analytical solutions for tsunami runup on a plane beach: single waves, N-waves and transient waves. *J. Fluid Mech.*, 645:27–57.

Mei, C. C. 1989. *The Applied Dynamics of Ocean Surface Waves*, volume 1. World scientific.

Miles, J. W. 1962. Transient gravity wave response to an oscillating pressure. *J. Fluid Mech*, 13:145–150.

Mori, N. and Takahashi, T. 2012. Nationwide post event survey and analysis of the 2011 tohoku earthquake tsunami. *Coastal Engineering Journal*, 54(01):1250001.

Mori, N., Takahashi, T., Yasuda, T., and Yanagisawa, H. 2011. Survey of 2011 tohoku earthquake tsunami inundation and run-up. *Geophysical research letters*, 38(7).

Peakall, J. and Warburton, J. 1996. Surface tension in small hydraulic river models-the significance of the weber number. *Journal of Hydrology (New Zealand)*, pages 199–212.

Pedersen, G. and Gjevik, B. 1983. Run-up of solitary waves. *Journal of fluid mechanics*, 135:283–299.

Peregrine, D. H. 1967. Long waves on a beach. *J. Fluid Mech.*, 27(04):815–827.

Puleo, J., Beach, R., Holman, R. A., and Allen, J. 2000. Swash zone sediment suspension and transport and the importance of bore-generated turbulence.

Rabinovich, A. B. and Thomson, R. E. 2007. The 26 december 2004 sumatra tsunami: analysis of tide gauge data from the world ocean part 1. indian ocean and south africa. In *Tsunami and Its Hazards in the Indian and Pacific Oceans*, pages 261–308. Springer.

Rossetto, T., Allsop, W., Charvet, I., and Robinson, D. I. 2011. Physical modelling of tsunami using a new pneumatic wave generator. *Coastal Engineering*, 58(6):517–527.

Russell, J. S. 1845. *Report on Waves: Made to the Meetings of the British Association in 1842-43*.

Schimmels, S., Sriram, V., and Didenkulova, I. 2016. Tsunami generation in a large scale experimental facility. *Coastal Engineering*, 110:32–41.

Shen, C., Qiu, J.-M., and Christlieb, A. 2011. Adaptive mesh refinement based on high order finite difference weno scheme for multi-scale simulations. *Journal of Computational Physics*, 230(10):3780–3802.

Shu, C.-W. 1998. Essentially non-oscillatory and weighted essentially non-oscillatory schemes for hyperbolic conservation laws. In Quarteroni, A., editor, *Advanced Numerical Approximation of Nonlinear Hyperbolic Equations*, volume 1697 of *Lecture Notes in Mathematics*, pages 325–432. Springer Berlin Heidelberg.

Shu, C.-W. and Osher, S. 1988. Efficient implementation of essentially non-oscillatory shock-capturing schemes. *Journal of Computational Physics*, 77(2):439–471.

Sweby, P. K. 1984. High resolution schemes using flux limiters for hyperbolic conservation laws. *SIAM J. Numer. Anal.*, 21(5):995–1011.

Synolakis, C. E. 1986. *The runup of long waves*. PhD thesis, California Institute of Technology.

Synolakis, C. E. 1987. The runup of solitary waves. *J. Fluid Mech.*, 185:523–545.

Synolakis, C. E. and Bernard, E. N. 2006. Tsunami science before and beyond boxing day 2004. *Philosophical Transactions of the Royal Society of London A: Mathematical, Physical and Engineering Sciences*, 364(1845):2231–2265.

Tadepalli, S. and Synolakis, C. E. 1994. The run-up of n-waves on sloping beaches. In *Proceedings of the Royal Society of London A: Mathematical, Physical and Engineering Sciences*, volume 445, pages 99–112. The Royal Society.

Titov, V. V. and Synolakis, C. E. 1995. Modeling of breaking and nonbreaking long-wave evolution and runup using vtcs-2. *Journal of Waterway, Port, Coastal, and Ocean Engineering*, 121(6):308–316.

Titov, V. V. and Synolakis, C. E. 1998. Numerical modeling of tidal wave runup. *Journal of Waterway, Port, Coastal, and Ocean Engineering*, 124(4):157–171.

Tonkin, S., Yeh, H., Kato, F., and Sato, S. 2003. Tsunami scour around a cylinder. *Journal of Fluid Mechanics*, 496:165–192.

Tuck, E. O. and Hwang, L.-S. 1972. Long wave generation on a sloping beach. *J. Fluid Mech.*, 51(03):449–461.

Tyvand, P. A. and Miloh, T. 2012. Incompressible impulsive sloshing. *Journal of Fluid Mechanics*, 708:279–302.

Walder, J. S., Watts, P., Sorensen, O. E., and Janssen, K. 2003. Tsunamis generated by subaerial mass flows. *Journal of Geophysical Research: Solid Earth*, 108(B5).

Wang, C., Dong, X., and Shu, C.-W. 2015. Parallel adaptive mesh refinement method based on weno finite difference scheme for the simulation of multi-dimensional detonation. *Journal of Computational Physics*, 298:161–175.

Wu, T. Y.-T. 1987. Generation of upstream advancing solitons by moving disturbances. *J. Fluid Mech.*, 184:75–99.

Xing, Y. and Shu, C.-W. 2005. High order finite difference WENO schemes with the exact conservation property for the shallow water equations. *J. Comput. Phys.*, 208(1):206–227.

Xing, Y. and Shu, C.-W. 2006. High order well-balanced finite volume weno schemes and discontinuous galerkin methods for a class of hyperbolic systems with source terms. *Journal of Computational Physics*, 214(2):567–598.

Yeh, H., Liu, P., Briggs, M., and Synolakis, C. 1994. Propagation and amplification of tsunamis at coastal boundaries. *Nature*, 372(6504):353–355.

Zelt, J. 1991. The run-up of nonbreaking and breaking solitary waves. *Coastal Eng.*, 15(3):205–246.

Zelt, J. and Raichlen, F. 1990. A lagrangian model for wave-induced harbour oscillations. *Journal of Fluid Mechanics*, 213:203–225.

Zhang, J. E. 1996. *Run-up of ocean waves on beaches*. California Institute of Technology.